POLARIMETRIC CALIBRATION OF SAR DATA USING MANMADE POINT TARGETS AND UNIFORMLY DISTRIBUTED NATURAL TARGETS

ABHISEK MAITI
March, 2019

SUPERVISORS:
Mr. Shashi Kumar
Dr. Valentyn A. Tolpekin
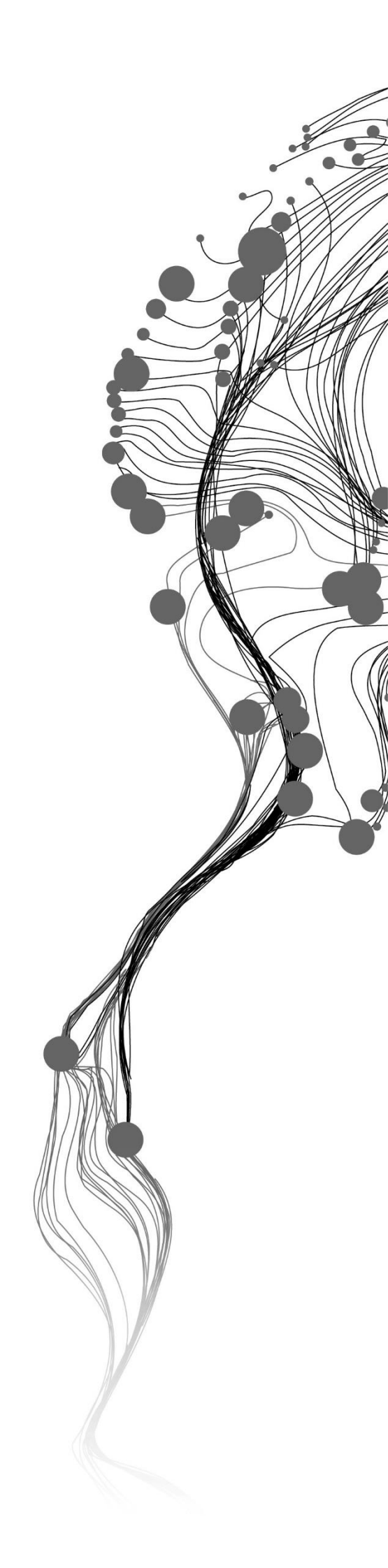
ADVISOR:
Mrs. Shefali Agarwal

POLARIMETRIC CALIBRATION OF SAR DATA USING MANMADE POINT TARGETS AND UNIFORMLY DISTRIBUTED NATURAL TARGETS

ABHISEK MAITI

Enschede, The Netherlands, March, 2019

Thesis submitted to the Faculty of Geo-Information Science and Earth Observation of the University of Twente in partial fulfilment of the requirements for the degree of Master of Science in Geo-information Science and Earth Observation.
Specialization: Geoinformatics

SUPERVISORS:
Mr. Shashi Kumar
Dr. Valentyn A. Tolpekin

ADVISOR:
Mrs. Shefali Agarwal

THESIS ASSESSMENT BOARD:
Prof. Dr. Ir. A. Stein (Chair, ITC Professor)
Dr. Anup Das (External Examiner, Space Applications Centre (SAC), Ahmedabad)

"You can know the name of a bird in all the languages of the world, but when you're finished, you'll know absolutely nothing whatever about the bird. You'll only know about humans in different places, and what they call the bird. So, let's take a look at the bird and see what it's doing — that's what counts."

- *Richard P. Feynman*

ABSTRACT

Polarimetric Synthetic Aperture Radar (PolSAR) calibration is an essential preprocessing step which must be performed to ensure that the data quality is adequate. This, in turn, helps to minimise the propagation of errors in any further data processing or information extraction. The measurements acquired by the SAR sensors are stored as digital numbers which cannot be directly related to the actual ground information. The main purpose of the radiometric correction is to represent these numbers in terms of backscatter energy. However, it cannot rectify the distortions present in the data. The crosstalk and channel imbalance are two major distortions found to be present in the uncalibrated polarimetric SAR data. The PolSAR calibration mainly aims to reduce these two distortions revealing the true scattering pattern of the targets. In this regard, Quegan's algorithm and Ainsworth algorithm are two widely used algorithms for the PolSAR calibration. However, the accuracy and efficiency of these algorithms vary. In this research, the accuracy and efficiency of these two algorithms have been thoroughly compared using suitable metrics. It has been shown that the Ainsworth algorithm performs better than the Quegan's in terms of accuracy at the cost of poor computational efficiency. Evidently, the Quegan's algorithm fails to meet the Committee on Earth Observation Satellites (CEOS) calibration requirement for the residual crosstalk for all the cases. In contrast, Ainsworth's estimates are more accurate while complying with this standard. Moreover, the data quality metrics also highlight the better calibration accuracy of the Ainsworth algorithm. The issue of higher computational complexity has been effectively addressed by coupling both of these algorithms. Evidently, the computational cost has been reduced in the case of the proposed algorithm. The polarisation orientation angle (POA) shift is another distortion caused by the topographic variations present in the target scene. Therefore, correction of POA shift has been incorporated in this research by coupling it with the PolSAR calibration. Subsequently, the improvement in the scattering has been observed. In essence, the proposed algorithm coupled with the correction of POA shift rectifies the major polarimetric distortions with adequate accuracy and computational efficiency.

Keywords: PolSAR, calibration, crosstalk, channel imbalance, POA shift

ACKNOWLEDGEMENTS

TABLE OF CONTENTS

LIST OF FIGURES

LIST OF TABLES

1. INTRODUCTION

1.1. Background

1.1.1. Synthetic Aperture Radar (SAR): A Brief Overview

Synthetic Aperture Radar (SAR) being a prominent remote sensing instrument having all-weather, day-and-night imaging capability, has gained unprecedented popularity in the recent trends of remote sensing. In addition, the polarimetric information in SAR data can be used to retrieve the geomorphological properties such as soil moisture and surface roughness (Skriver et al., 2003). SAR is an active microwave remote sensing system which transmits polarised microwave pulse and measures the power of the backscattered signal from the target in the form of complex values (Moreira et al., 2013). The radar observation of each pixel is the coherent sum of the backscatter response from all the distributed targets within the spatial extent of that pixel (Doring, Looser, Jirousek, & Schwerdt, 2011). These measurements represent the geophysical and geometric properties of the corresponding targets. Also, the radar measurement of a specific target must be consistent irrespective of the sensors, given that the influences of other factors (frequency of the radar, viewing geometry and so on) on the radar observation are compensated. In this regard, the calibration of SAR data plays a pivotal role to ensure the quality of the dataset.

1.1.2. SAR Polarimetry

There are different variations of SAR systems depending upon their implementation and use cases. SAR systems commonly make use of two linear polarisation channels namely horizontal polarisation and vertical polarisation (Cloude, 2009). Typically, a single-pol radar transmits microwave pulses with a single polarisation and receives the signal in the same polarisation as well. In the case of dual-pol radar systems, the polarisation of the transmission channel and receiving channel are different. The quad-pol or full polarimetric radar transmits in both the polarimetric channels alternatingly but receives signal in both the channels simultaneously. Thus, a full-pol system is capable of acquiring data in all possible combinations of transmitting and receiving polarisation channels. In hybrid-pol radar, the circularly polarised signal is transmitted, and the backscattering response is received in both the standard polarisation channels. The transmission signal of hybrid-pol radar is either left circular or right circular. A hybrid-pol radar capable of transmitting both left circular and right circular signal is known as compact-pol radar system (Jet Propulsion Laboratory NASA, 2016). Among all these variations of SAR, the full-polarimetric mode is widely popular, and the term 'PolSAR' commonly refers to the quad-pol SAR unless specified otherwise. The critical advantage of the PolSAR is that observations from multiple polarisation channels can be used to retrieve additional information about the target (Cloude, 2009).

1.1.3. Calibration

The term 'calibration' is defined as, "Operation that, under specified conditions, in a first step, establishes a relation between the quantity values with measurement uncertainties provided by measurement standards and corresponding indications with associated measurement uncertainties and, in a second step, uses this information to establish a relation for obtaining a measurement result from an indication" (Clifford, 1985). Essentially, the calibration process ensures that all the measurements by the respective instrument are quantifiable and reproducible under the same conditions with acceptable accuracy and precision. Thus, every scientific device needs to be appropriately calibrated before being used for reliable measurements.

1.1.4. Need for SAR Calibration

The measurements from the different polarisation channels, however, require to be quantitively comparable to take advantage of the added benefits from the PolSAR data (Freeman, 1989). The anomaly which hinders this comparability of measurements from different polarisation channels is known as channel imbalance (van Zyl & Kim, 2011b). The radar observations contain amplitude as well as phase information (Cloude, 2009). Therefore distortion may occur in the phase of the radar measurement along with its amplitude.

Consequently, channel imbalance represents both amplitude imbalance and phase imbalance (van Zyl & Kim, 2011b). Additionally, the polarisation channels need to be completely isolated to reduce the undesirable attenuation by one polarisation channel on the measurements of the other polarisation channels (Al-kahachi, 2014). Distortions in PolSAR data due to improper channel isolation are commonly known as crosstalk (Baffelli, Frey, Werner, & Hajnsek, 2018). The working principle of SAR dictates that the pixel spacing in the SAR image is smaller compared to the spatial resolution. Due to this reason, a typical point target occupies more than one pixel. This, in turn, leads to the error in the estimation of Radar Cross Section (RCS) (van Zyl & Kim, 2011b). At the time of SAR data acquisition, it is challenging to avoid all these issues entirely (Freeman, 1992). For this reason, SAR data require additional correction and pre-processing.

Proper calibration of PolSAR data is a reasonably complex process which is mostly based on the statistical comparison of the data with the ideal theoretical models assuming the backscattering symmetry (Al-kahachi, 2014). This typically involves three crucial steps. The antenna gain of the SAR sensor is appropriately estimated, and the corresponding dataset is corrected through the absolute calibration of the polarimetric dataset. This, in turn, minimises the errors in the estimation of RCS. Rectification of channel imbalance ensures the cross-pol reciprocity and the crosstalk minimisation reduces the error in the data due to imperfect isolation of the polarisation channels. There are well established theoretical models for radiometric correction (Doring et al., 2011; El-Darymli, McGuire, Gill, Power, & Moloney, 2014; Gray, Vachon, Livingstone, & Lukowski, 1990; van Zyl & Kim, 2011a). However, calibration techniques for crosstalk and channel imbalance minimisation are still under active research.

1.1.5.   Recent Advancements in PolSAR Calibration

Currently, there are two widely popular methods for crosstalk calibration (Fore et al., 2015). The approach of Quegan, (1994) is based upon the assumption of reciprocity of the cross polarised channels. Additionally, it also assumes azimuth symmetry, which means that the co-pol and cross-pol channels are truly uncorrelated in any scene dominated by distributed targets (Quegan, 1994). Kimura, Mizuno, Papathanassiou, & Hajnsek, (2004) further improved the Quegan's algorithm by incorporating the cross-channel noise imbalance; this algorithm is popularly known as the improved Quegan's algorithm. However, the Quegan's assumptions do not always hold in the raw SAR dataset. Later on, Ainsworth, Ferro-Famil, & Jong-Sen, (2006) proposed a posteriori model to estimate the crosstalk which is only based upon the weak constraint of scattering reciprocity (Ainsworth, Ferro-Famil, & Lee, 2006).

A comparative analysis of the uncalibrated and the calibrated SAR data shows the significance of the Polarimetric SAR calibration. The Maximum Normalised Error (MNE) and the decomposition error are the two widely accepted metrics to assess the SAR data quality (Wang, Ainsworth, & Lee, 2011). A study by Wang, Ainsworth, & Lee (2011) shows that both crosstalk and channel imbalance increase the MNE and decomposition error.

1.2.   Motivation and Problem Statement

The PolSAR calibration as a whole is not streamlined (Freeman, 1989). In this research, the focus is on estimation and minimisation of crosstalk and channel imbalance of NASA Uninhabited Aerial Vehicle Synthetic Aperture Radar (UAVSAR) L-Band dataset. For this purpose, both Quegan's and Ainsworth algorithm has been adopted, and their accuracies are thoroughly compared by observing the change in the polarimetric signature and the accuracy of the polarimetric decompositions. Besides, the shift in Polarisation Orientation Angle (POA) due topography of the surface has been considered and appropriately corrected.

1.3.   Research Identification

The overall focus of this research is the minimisation of estimation and minimisation of crosstalk, channel imbalance and POA shift present in the uncalibrated PolSAR data and analytically evaluate the effect of calibration. Furthermore, this study aims to evaluate different PolSAR calibration algorithms and observe the effect of POA shift correction on the scattering pattern.

1.3.1. Research Objectives

The prime objective of this research is to study the effectiveness of the Polarimetric SAR calibration algorithms for estimation and minimisation of crosstalk, channel imbalance. Additionally, it aims to investigate the effect of the POA shift correction. In this regard, suitable natural or manmade targets and the targets depicting surface scattering will be used in order to derive the calibration parameters. Furthermore, this study focuses on analysing the effect of the calibration on the overall data quality.

1.3.1.1. Specific Objectives

The specific objectives of this research are:
  I. To estimate and minimise the channel imbalance and crosstalk for the calibration of the scattering matrix.
 II. To estimate and compensate the shift in the polarisation orientation angle of the polarisation ellipse.
III. To study and analyse the effect of calibration on the PolSAR data quality

1.3.2. Research Questions

This research intends to answer the following research questions:
  I. How Quegan's algorithm and Ainsworth algorithm compare in terms of accuracy?
 II. How improved Quegan's algorithm leads to a better estimation of crosstalk?
III. What is the effect of the shift in Polarisation Orientation Angle (POA) on PolSAR data?
 IV. How to improve the computational efficiency of the calibration algorithm?

1.4. Innovation

This study aims to optimise the Ainsworth algorithm for PolSAR calibration concerning the computational complexity without compromising with its accuracy. In order to achieve the same, a hybrid approach has been adopted using both the Ainsworth's and Quegan's algorithm. Moreover, the recommendation of Ainsworth & Lee, (2001) regarding the data quality has been incorporated into the algorithm. Additionally, the process of POA shift compensation has been incorporated as a part of PolSAR calibration to further improve the data quality.

1.5. Thesis Outline

The thesis has been adequately organised to coherently guide the reader throughout the research. Chapter 2 provides the necessary background of this research in detail. Then chapter 3 describes the methodology adopted for this research. After that, chapter 4 shows the chosen study area following by chapter 5 showing the relevant results. Next, chapter 6 describes the implications of these results to the readers and answers the research questions. Finally, the thesis concludes with chapter 7 providing a summary of the key findings and remarks for the potential future works.

2. LITERATURE REVIEW ON POLSAR CALIBRATION

This chapter summarises the scientific and theoretical background of the polarimetric SAR calibration. It begins with an overview of the PolSAR calibration, following which different calibration methods are discussed. Finally, it concludes with a discussion on the existing algorithms for PolSAR calibration.

2.1. PolSAR Calibration

Calibration of PolSAR is essential to establish the relationships between the radar backscatter and the geophysical properties of the scene. In addition to this, it improves overall data quality. PolSAR calibration is a fairly complex process which is mostly based on the statistical comparison of the data with the ideal theoretical models assuming the backscattering symmetry (Al-kahachi, 2014). However, the calibration approach varies depending upon the sensor, band, data acquisition platform and use case. However, the SAR platform is the most prominent factor which governs the overall calibration process. These are described in the following subsections.

2.1.1. Spaceborne SAR

SAR exploits the motion of the platform. Evidently, the relative angle of each point along the track with respect to the direction of the velocity of the radar is different. As a result, the Doppler frequency of the response received from each of the points along the flight line will be unique. Therefore, each point lying in the azimuth direction can be uniquely identified using the Doppler frequency analysis or doppler beam sharpening. SAR extensively use this technique to enhance the azimuth resolution without the requirement of a larger physical antenna. The azimuth resolution of SAR can be derived as shown in equation (1) (van Zyl & Kim, 2011b).

$$x_g = \frac{L}{2} \tag{1}$$

Where,

x_g : Azimuth resolution the SAR sensor

L : Effective antenna length in the zimuth direction

It is evident from equation (1) that, unlike real aperture radar, azimuth resolution of SAR is not directly affected by the effective range of the scene or the flying height (van Zyl & Kim, 2011b). On the contrary, the range resolution of SAR is inherently independent of the flying height. These two facts are the main reason behind the feasibility of the spaceborne SAR systems.
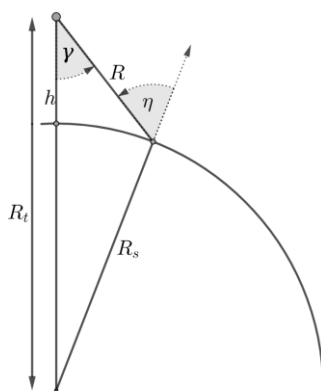
Figure 1: Look angle and incidence angle in case of very high flying-height (h), i.e., in the case of spaceborne sensor the effect of the Earth's curvature has significant influence over look angle and incidence angle.

There are additional issues associated with spaceborne SAR regarding the calibration. The radar look angle is one of the critical factors governing the antenna radiation pattern at a particular target point. In the case of the spaceborne SAR, the target scene cannot be assumed flat because of the high flying-height and the large ground footprint of the radar pulse. Therefore, earth's curvature has to be considered for accurately determining the antenna gain which is essential for the proper calibration of the SAR data (van Zyl & Kim, 2011b). As shown in Figure 1, the radar look angle (γ) and the incidence angle (η) at a point is not the same when the earth's curvature is considered. In this case, the look angle can be indirectly derived using equation (2).

$$\gamma = \cos^{-1}\left(\frac{R^2 + R_s^2 - R_t^2}{2RR_s}\right) \tag{2}$$

Where,
R : Effective slant range of the point
R_s : Distance of the SAR platform from the centre of the Earth
R_t : Distance of the target point from the centre of the Earth

Additionally, the transmitted pulse and the return signal of the spaceborne SAR pass through the ionised plasma of the ionosphere (Thompson, Moran, & Swenson Jr., 2017). According to the Faraday effect, the induced magnetic field of the ionosphere rotates the polarisation plane of the radar signal (Campbell & Ostro, 2014). Bickel & Bates (1965) experimentally showed that the effect of Faraday rotation on the scattering matrix due to the attenuation by ionosphere is non-reciprocal. The relation between the true scattering matrix ([S]) and the distorted scattering matrix ([S']) is subject to Faraday rotation (Freeman, 2004). This relation is shown in equation (3).

$$\underbrace{\begin{pmatrix} S'_{hh} & S'_{vh} \\ S'_{hv} & S'_{vv} \end{pmatrix}}_{[S']} = \underbrace{\begin{pmatrix} \cos\Omega & \sin\Omega \\ -\sin\Omega & \cos\Omega \end{pmatrix}}_{[R_F]} \underbrace{\begin{pmatrix} S_{hh} & S_{vh} \\ S_{hv} & S_{vv} \end{pmatrix}}_{[S]} \underbrace{\begin{pmatrix} \cos\Omega & \sin\Omega \\ -\sin\Omega & \cos\Omega \end{pmatrix}}_{[R_F]} \tag{3}$$

In equation (3), [R_F] is the oneway Faraday rotation matrix, Ω is the Faraday Rotation Angle (FRA). The generic term S_{tr} represents the backscattering measurement where t is the polarisation of the transmission pulse and r is the polarisation of the received signal. However, the effect of Faraday's rotation on signals from higher frequency bands like X-band and C-band is negligible (Shimada, 2011).

2.1.2.   Airborne SAR

SAR data acquisitions are also possible using an airborne platform. Although airborne SAR system has many operational disadvantages, it has fewer issues regarding the calibration of the data. The typical flying height of airborne radar is decidedly less compared to the spaceborne radar. In this case, the effect of earth curvature on the antenna pattern would be negligible.

Therefore, it is safe to assume flat earth throughout a scene of an airborne radar image. From Figure 2, it is evident that the look angle of the airborne radar is the same as the incidence angle of the target. A typical aircraft cannot fly over the ionosphere due to the engineering limitations. Consequently, the airborne SAR systems are entirely unexposed to the Faraday effect as their signals never pass through a dense electromagnetic field like the ionosphere (Hoekman & Quiriones, 2000).
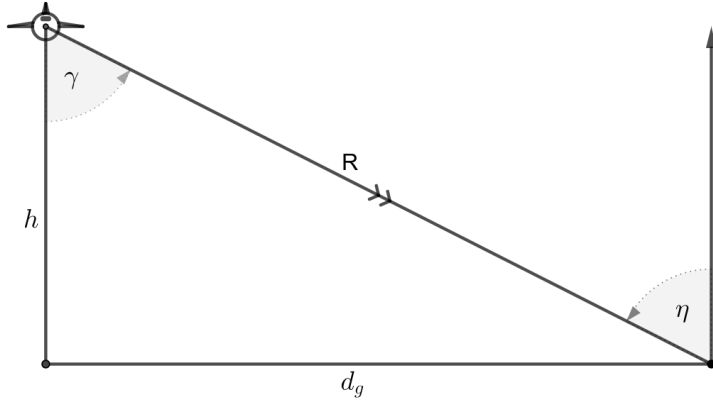
Figure 2: Local incidence angle and look angle of airborne SAR assuming flat earth

2.2.   Methods of PolSAR Calibration

Proper calibration of PolSAR involves three important steps, namely absolute radiometric calibration, rectification of crosstalk and minimisation of channel imbalance. There are well established theoretical models for radiometric correction (Doring et al., 2011; El-Darymli et al., 2014; Gray et al., 1990; van Zyl & Kim, 2011a). In order to understand the overall calibration process in a better way, first, the polarisation leakage of one polarisation channel into another polarisation channel in the transmitted pulse has to be appropriately modelled. The distortion model of the electric field at the time of transmission is shown in equation (4) (van Zyl & Kim, 2011b).

$$\mathrm{E}^t_{actual} = K_t(\gamma) \begin{pmatrix} f_t(\gamma) & \delta^t_1(\gamma) \\ \delta^t_2(\gamma) & 1 \end{pmatrix} \mathrm{E}^t_{ideal} \tag{4}$$

Where,
E^t_{ideal} : Transmitted electric field in the ideal condition
E^t_{actual} : Observed electric field
f_t : Coefficient representing the differences in the antenna pattern
δ_1, δ_2 : Coefficients representing the crosstalk
K_t : Absolute calibration parameter

Following equation (4), the observed scattering matrix ($\mathrm{S}_{observed}$) can be modelled in terms of true scattering matrix (S_{ideal}) as shown in equation (5) (van Zyl & Kim, 2011a).

$$\mathrm{S}_{observed} = K(\gamma)[\mathrm{R}][\mathrm{S}_{ideal}][\mathrm{T}] + [\mathrm{N}] \tag{5}$$

Where,

$$[\mathrm{R}] = \begin{pmatrix} f_r(\gamma) & \delta^r_1(\gamma) \\ \delta^r_2(\gamma) & 1 \end{pmatrix}$$

$$[\mathrm{T}] = \begin{pmatrix} f_t(\gamma) & \delta^t_1(\gamma) \\ \delta^t_2(\gamma) & 1 \end{pmatrix}$$

The terms $[\mathrm{T}]$ and $[\mathrm{R}]$ in equation (5) represents the distortion of the signal at the time of transmission and at the time of reception respectively and $[\mathrm{N}]$ represents the random system noise. It is worth mentioning that, the effect of Faraday rotation and random noise has not been considered in this model.

2.3. Radiometric and Polarimetric Phase Calibration

The rigorous experimentations show that the external calibrators are the more suitable for estimation of absolute radiometric parameters and phase imbalance terms compared to the theoretical estimation from the precisely known system parameters and antenna pattern (Fore et al., 2015). External radar calibrators can be broadly categorised into two types based upon their operational principle.

2.3.1. Active Calibrator

Active radar calibrator is special kind of transponder which receives the radar pulse from the actual radar sensor, measures its intensity, and in return, it sends an echo of adequately amplified intensity towards the radar (Lenz, Schuler, Younis, & Wiesbeck, 2005). Moreover, it is precisely synchronised with the overflight radar sensor and tracks it during the calibration (Tang & Xu, 2015). Active transponders as external calibrators have several advantages. The RCS of the active transponder is adjustable making it more versatile (Hounam & Wagel, 2001). Also, the response of the transponder is easily identifiable in the image as the synthesised echo is amplified and precisely directed towards the radar by tracking the radar sensor. In addition, there are advanced modulation techniques in order to differentiate the active transponder response from passive echo from the nearby region of the calibrator (Brunfeldt & Ulaby, 1984). However, being an active device, it requires power and sophisticated electronics in order to operate, and it needs frequent maintenance (Kemp & Martin, 1990). There many well-known spaceborne SAR systems (Sentinel-1, TerraSAR-X, RADARSAT-2) which have been calibrated using the active transponders (Lenz et al., 2005; Luscombe, Chotoo, & Huxtable, 2000; Snoeij et al., 2010).

2.3.2. Passive Calibrator

Passive radar calibrators generally refer to the targets with either well-known uniform backscattering properties or theoretically predictable RCS (Sarabandi, 1993). Unlike active calibrators, passive calibrators do not require external power to operate. Passive calibrators can be categorised into two major types, namely natural targets and manmade targets.

2.3.2.1. Natural Targets for Calibration

The naturally occurring targets can be suitable passive calibrator if their scattering properties are very well-known and consistent. van Zyl (1993) explored the suitability of different natural targets as consistent scatterers using the NASA Airborne SAR (AIRSAR) and concluded that a forest crown could be approximated as a collection of narrow cylinders which are randomly oriented. Therefore, the rainforests over flat terrains can be safely assumed as uniformly distributed Lambertian targets (Shimada, 2011). Evidently, the Committee of Earth Observation Satellites (CEOS) has adopted rainforest on flat terrain as a standard for radar calibration (Desnos et al., 1999; Shimada & Freeman, 1995). There are different approaches of calibration using the distributed natural targets (Sarabandi, 1993; Shimada & Freeman, 1995) Several studies have been able to successfully retrieve the antenna pattern of different spaceborne SAR systems using the Amazon rainforest (Cote, Srivastava, Dantec, & Hawkins, 2005; Shimada, 2011).

2.3.2.2. Manmade Targets for Calibration

In contrast with the natural targets, manmade targets generally exhibit more predictable and consistent scattering pattern as shown by Kimura (2009), where a method has been presented to derive the system distortions using polarisation orientation in the built-up areas. However, manmade point targets designed explicitly for radar calibration are widely popular as their RCS can be accurately predetermined. These carefully designed passive targets are commonly known as corner reflectors. A corner reflector is typically made of lightweight conductive, and highly reflective metallic plates fixated to form a particular geometric shape improving its directional reflectivity (Bonkowski, Lubitz, & Schensted, 1953). There are different types of corner reflectors depending upon their design, some of which are discussed in section 2.4.

2.4. Corner Reflectors

A corner reflector is a scientifically engineered passive manmade point target which reflects the incoming signal in the precisely opposite direction, ideally without any scattering. Therefore, the basic principle of a corner reflector is similar to that of a retroreflector (Skolnik, 1990). The corner reflectors can be of different types depending upon their shape and the reflection properties. Some of the popular corner reflectors are discussed in the following subsections.

2.4.1. Flat Plate

A flat conductive plate can work as a very basic corner reflector. The RCS of the corner reflector can be derived using different approaches. Andrade, Nohara, Peixoto, Rezende, & Martin (2003) used physical optics method to theoretically derive the RCS of a flat plate corner reflector as shown in equation (6). Figure 3 depicts the working of the flat plate corner reflector.

$$\sigma_0 = 4\pi \left(\frac{ab}{\lambda}\right)^2 \cos^2(\theta_i) \left[\frac{\sin(\beta b \sin(\theta_i))}{\beta b \sin(\theta_i)}\right]^2 \tag{6}$$

Where,

a : Length of the plate

b : Breadth of the plate

θ_i : Incidence angle satisfying $-\frac{\pi}{2} \leq \theta_i \leq +\frac{\pi}{2}$

λ : Wavelength of the radar signal

β : Phase constant
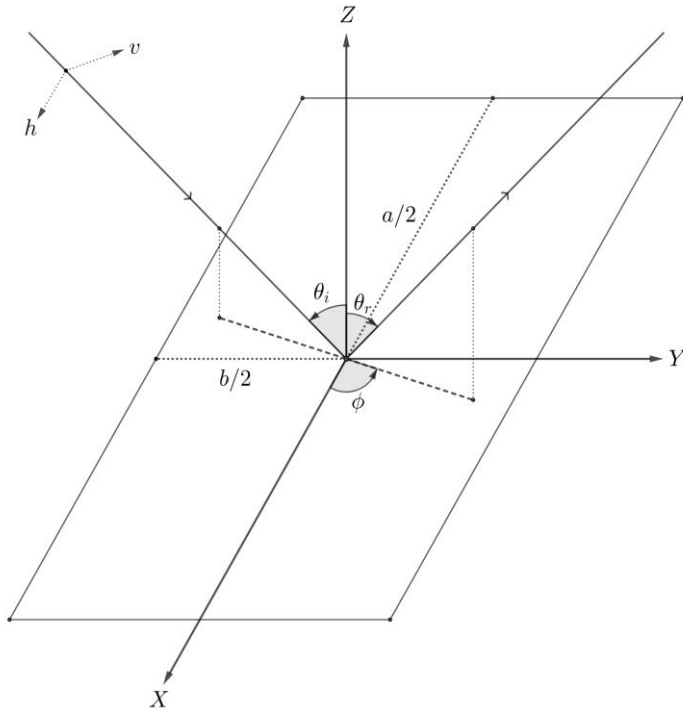
Figure 3: Reflection of radar signal by conductive flat plate

2.4.2. Dihedral Corner Reflector

A dihedral corner reflector consists of two flat conductive placed in a particular angle and having a common edge as shown in Figure 4.
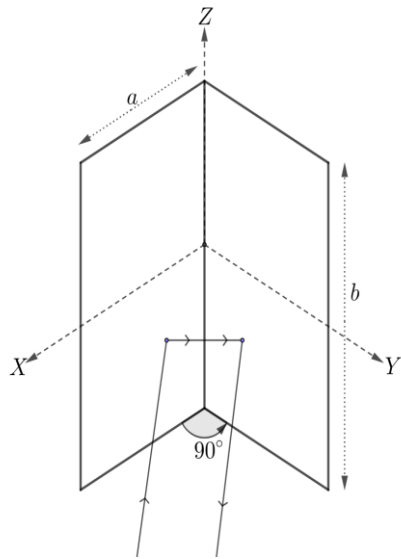
Figure 4: Schematic diagram of a dihedral Corner Reflector

The effective RCS of the dihedral corner reflector depends upon the angle between the plates, and the RCS is maximum when the plates are at right angle to each other (Knott, 1977). Griesser & Balanis (1987) extensively modelled the theoretical RCS of the dihedral corner reflector using different approaches. However, according to Sorensen, (2013), assuming the plates are at a right angle with respect to each other and the rectangular plates are having the same dimensions, the maximum RCS (σ_{max}) of a dihedral corner reflector can be expressed in equation (7).

$$\sigma_{max} = 8\pi \left(\frac{ab}{\lambda}\right)^2 \tag{7}$$

Where,

a : Width of the each of the flat plate
b : Height of the each of the flat plate
λ : Wavelength of the EM wave

2.4.3. Triangular Trihedral Corner Reflector

A triangular trihedral corner reflector generally consists of three flat triangular plates at a right angle to each other meeting at a common apex point and sharing an edge with the immediate neighbours. Doerry & Brock (2009) theoretically derived the RCS (σ_{tri}) of the triangular trihedral corner reflector presented in equation (8), assuming the inner leg length of each flat plate is equal and, each of them are at a right angle with respect to its neighbouring plate as shown in Figure 5.

$$\sigma_{tri} = \frac{4\pi}{\lambda^2}(2A_{tri})^2 a^4$$

$$A_{tri} = \begin{cases} \sin\theta\cos\psi & if \ \cos\theta - \sin\theta \geq \tan\psi \\ \dfrac{2\sin\theta\cos\theta\cos\psi}{\sin\theta \ + \ \cos\theta \ + \ \tan\psi} & else \end{cases} \tag{8}$$

Where,

λ : Wavelength of the EM wave
a : Inner leg length of the triangular trihedral corner reflector
θ : Angle between the X axis and the projection of viewing perspective in the XY plane
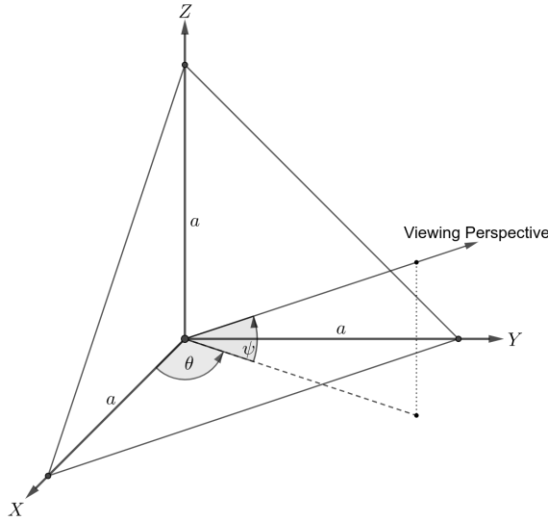
Figure 5: Schematic diagram of a triangular trihedral corner reflector showing viewing geometry

ψ : Angle of viewing perspective with respect to the XY plane

Analytically comparing equations (6), (7) and (8), it can be concluded that the RCS of the triangular trihedral corner reflector largest among the three given that other constraint such as the size of the corner reflector, viewing geometry and the wavelength remains same or equivalent. The study by Qin, Perissin & Lei (2013) supports this conclusion.

2.5.   Algorithms for Crosstalk Calibration

It has been shown by van Zyl (1990) that distributed natural targets are sufficient in order to estimate the crosstalk provided some assumptions are satisfied. However, manmade point targets such as corner reflectors coupled with the distributed natural targets can significantly improve the calibration accuracy (van Zyl, 1990). Whitt, Ulaby, Polatin & Liepa (1991) presented an eigenvalue and eigenvector based approximate PolSAR calibration model with reasonable accuracy. However, the problem of the non-invertible matrix is not addressed by this method. Quegan (1994) proposed a non-iterative generalised algorithm for crosstalk calibration based on the findings of van Zyl (1990). Later on, Kimura, Mizuno, Papathanassiou, & Hajnsek (2004) improved the algorithm proposed by Quegan (1994) considering the asymmetric cross-polarisation channel noises. Ainsworth et al. (2006) proposed a new iterative posterior approach for crosstalk and channel imbalance correction imposing lesser constraints than the previous algorithms. In the following subsections, Quegan's algorithm and the Ainsworth algorithm are discussed briefly followed by a brief discussion on recent advancements in this field.

2.5.1.   Quegan's Algorithm

The preconditions of the Quegan's algorithm are:
1.   The acquired dataset is fully polarimetric and available in the form of the scattering matrix.
2.   The observed scattering matrix can be modelled as a linear system, similar to equation (5).
3.   Scattering reciprocity is satisfied unless the target is physically altered, i.e., $S_{ij} = S_{ji}$.
4.   In the case of distributed targets, cross-polarised channels are not correlated, i.e., $\langle S_{ii}S_{ij}^* \rangle = 0$.
5.   The off-diagonal terms of the matrices [R] and [T] from equation (5) are small compared to the diagonal terms.

Here, S_{ij} represents the backscattering response at polarisation channel i when the stimulating polarisation channel is j. Due to condition (3) and condition (4), the ensembled covariance matrix ($\langle C_s \rangle$) gets reduced as shown in equation (9).

$$\langle C_S \rangle = \begin{bmatrix} \sigma_{HH} & 0 & \rho \\ 0 & \sigma_{VH} & 0 \\ \rho^* & 0 & \sigma_{VV} \end{bmatrix} \tag{9}$$

Where,

$\sigma_{ij} = \langle S_{ij} S_{ij}^* \rangle$

$\rho = \langle S_{HH} S_{VV}^* \rangle = \langle S_{VV} S_{HH}^* \rangle^*$

On the contrary, equation (5) can be rewritten as equation (10).

$$[S'] = [M][S] + [N] \tag{10}$$

Where,

$[S']$: Observed scattering matrix in the form $(S'_{HH}, \ S'_{HV}, \ S'_{VH}, \ S'_{VV})^T$

$[S]$: True scattering matrix in the form $(S_{HH}, \ S_{VH}, \ S_{VV})^T$

$[M]$: Distortion matrix of dimension (4×3)

$[N]$: System noise matrix in the form $(N_{HH}, \ N_{HV}, \ N_{VH}, \ N_{VV})^T$

Now, the observed covariance matrix (C) can be derived using equation (11) ignoring the noise $[N]$.

$$C = MC_S M^\dagger \tag{11}$$

On the other hand, the distortion matrix can be expressed as shown in equation (12).

$$M = Y \begin{pmatrix} \alpha & v + \alpha w & vw \\ au & \alpha & v \\ \alpha z & 1 & w \\ \alpha uz & u + \alpha z & 1 \end{pmatrix} \begin{pmatrix} k^2 & 0 & 0 \\ 0 & k & 0 \\ 0 & 0 & 1 \end{pmatrix} \tag{12}$$

Here, u, v, w, z are the complex crosstalk parameters and α, k are the complex channel imbalance parameters. By considering the azimuthal symmetry and the condition (4), the solution for the terms u, v, w, z can be obtained as shown in equations (13).

$$u = (C_{44} C_{21} - C_{41} C_{24})/\Delta \qquad \text{... a}$$
$$v = (C_{11} C_{24} - C_{21} C_{14})/\Delta \qquad \text{... b}$$
$$z = (C_{44} C_{31} - C_{41} C_{34})/\Delta \qquad \text{... c} \quad (13)$$
$$w = (C_{11} C_{34} - C_{31} C_{14})/\Delta \qquad \text{... d}$$
$$\Delta = C_{11} C_{44} - |C_{14}|^2 \qquad \text{... e}$$

Similarly, the term α can be derived as shown in equations (14), assuming the random noises in cross-polarised channels are equal, i.e. $N_{VH} = N_{HV}$.

$$\alpha = \frac{|\alpha_1 \alpha_2| - 1 + \sqrt{(|\alpha_1 \alpha_2| - 1)^2 + 4|\alpha_2|^2}}{2|\alpha_2|} \frac{\alpha_1}{|\alpha_1|} \qquad \text{... a}$$
$$\alpha_1 = \frac{C_{22} - u C_{12} - v C_{42}}{X} \qquad \text{... b} \quad (14)$$
$$\alpha_2 = \frac{X^*}{C_{33} - z^* C_{31} - w^* C_{34}} \qquad \text{... c}$$
$$X = C_{32} - z C_{12} - w C_{42} \qquad \text{... d}$$

2.5.2.   Improved Quegan's Algorithm

Kimura et al. (2004) showed that the assumption of $N_{VH} = N_{HV}$ cannot be satisfied for some sensors such as the ALOS/PALSAR. Therefore, considering the imbalanced cross-pol noise, Kimura et al. (2004) modified equation (14a) into equation (15).

$$\alpha = \frac{|\alpha_1\alpha_2| - m + \sqrt{(|\alpha_1\alpha_2| - m)^2 + 4m|\alpha_2|^2}}{2|\alpha_2|} \frac{\alpha_1}{|\alpha_1|} \qquad \dots a$$

$$m = \frac{N_{VH}}{N_{HV}} \approx \frac{\langle S'_{VH}S'^*_{VH} \rangle}{\langle S_{HV}S^*_{HV} \rangle} \qquad \dots b$$

(15)

However, the assumptions of the Quegan's algorithm implies that the algorithm is only applicable when there is no polarisation orientation angle, and the helicity is effectively zero (Ainsworth & Lee, 2001). These stringent requirements may not always be satisfied; thus, there is a need for an improved algorithm.

2.5.3.   Ainsworth's Algorithm

Ainsworth et al. (2006) proposed a new algorithm for PolSAR calibration addressing the drawbacks of the Quegan's algorithm. This algorithm uses a posteriori approach which does not require the prior relationship between [R] and [T] in equation (5). Moreover, it imposes only one weak constraint which is scattering reciprocity (Ainsworth et al., 2006). Fore et al., (2015) showed that, according to Ainsworth's model, the true covariance matrix could be expressed as shown in equation (16).

$$\langle C_s \rangle = \begin{bmatrix} \sigma_{hhhh} & A^* & A^* & \sigma_{hhvv} \\ A & \beta & \beta' & B \\ A & \beta' & \beta & B \\ \sigma^*_{hhvv} & B^* & B^* & \sigma_{vvvv} \end{bmatrix}$$

(16)

Here equation (10) can be rewritten as equation (17).

$$\underbrace{\begin{bmatrix} S'_{HH} \\ S'_{VH} \\ S'_{HV} \\ S'_{VV} \end{bmatrix}}_{[\mathbf{S'}]} = [M] \underbrace{\begin{bmatrix} S_{HH} \\ S_{VH} \\ S_{HV} \\ S_{VV} \end{bmatrix}}_{[\mathbf{S}]} + \underbrace{\begin{bmatrix} N_{HH} \\ N_{VH} \\ N_{HV} \\ N_{VV} \end{bmatrix}}_{[\mathbf{N}]}$$

(17)

Here, [M] can be expressed as shown in equation (18) assuming dataset is radiometrically and phase calibrated.

$$[M] = \begin{bmatrix} 1 & u\sqrt{\alpha} & v/\sqrt{\alpha} & vw \\ u & \sqrt{\alpha} & uv/\sqrt{\alpha} & v \\ z & wz\sqrt{\alpha} & 1/\sqrt{\alpha} & w \\ uz & z\sqrt{\alpha} & u/\sqrt{\alpha} & 1 \end{bmatrix}$$

(18)

Now, the crosstalk parameters can be obtained by solving the system of equations (19a) which is obtained by considering the linear terms from the expansion of equation (5).

$$\begin{bmatrix} \Re(\zeta + \tau) & -\Im(\zeta - \tau) \\ \Im(\zeta + \tau) & \Re(\zeta - \tau) \end{bmatrix} \begin{bmatrix} \Re(\delta) \\ \Im(\delta) \end{bmatrix} = \begin{bmatrix} \Re(\chi) \\ \Im(\chi) \end{bmatrix} \qquad \dots a \quad (19)$$

$$\zeta = \begin{bmatrix} 0 & 0 & C_{41} & C_{11} \\ C_{11} & C_{41} & 0 & 0 \\ 0 & 0 & C_{44} & C_{14} \\ C_{14} & C_{44} & 0 & 0 \end{bmatrix} \qquad \dots b$$

$$\tau = \begin{bmatrix} 0 & C_{33} & C_{32} & 0 \\ 0 & C_{23} & C_{22} & 0 \\ C_{33} & 0 & 0 & C_{32} \\ C_{23} & 0 & 0 & C_{22} \end{bmatrix} \qquad \dots c$$

$$\chi = \begin{bmatrix} C_{31} - A \\ C_{21} - A \\ C_{34} - B \\ C_{24} - B \end{bmatrix} \qquad \dots d$$

$$A = \frac{1}{2}(C_{31} + C_{21}) \qquad \dots e$$

$$B = \frac{1}{2}(C_{34} + C_{24}) \qquad \dots f$$

Therefore, the calibrated covariance matrix can be obtained as shown in equation (20), ignoring $[N]$.

$$C_c = \Sigma C_s \Sigma^\dagger \qquad \dots a$$
$$\Sigma = [M]^{-1} \qquad \dots b \qquad (20)$$

Theoretically, there should not be any change if the calibration algorithm reapplied on the dataset any number of time (Ainsworth et al., 2006). Ainsworth algorithm ensure this by iteratively adjusting the calibrated covariance matrix (C_c) using equation (20), until the convergence is reached. In each iteration, the crosstalk and channel imbalance parameters are modified as shown in the equation.

$$u = u + u_i/\sqrt{\alpha} \qquad \dots a$$
$$v = v + v_i/\sqrt{\alpha} \qquad \dots b$$
$$w = w + w_i\sqrt{\alpha} \qquad \dots c \qquad (21)$$
$$z = z + z_i\sqrt{\alpha} \qquad \dots d$$
$$\alpha = \alpha\alpha_i \qquad \dots e$$

Here, subscript indicates the value of the respective parameter in the current (i^{th}) iteration. It is worth noting that, this algorithm ignores the nonlinear terms from the expansion of equation (5) in order to model the crosstalk parameters. Therefore, the solution of equation (19a) might not be the exact solution.

2.5.4. Recent Advancements

Although Quegan's and Ainsworth's PolSAR calibration algorithms are well established, Hu, Qiu, Hu & Ding (2015) presented a new approach of PolSAR calibration considering the effect of POA shift. Fore et al., (2015) performed an extensive study on PolSAR calibration using both Quegan's and Ainsworth's algorithm and concluded that the Ainsworth's algorithm provides a more stable estimation of crosstalk parameters compared to the results of Quegan's algorithm.

2.6. Estimation and Correction of POA Shift

Polarisation orientation angle is the angle between the major axis of the polarisation ellipse and the horizontal direction of the polarisation plane. A schematic representation of the orientation angle (ψ) along with the ellipticity angle (χ) are shown in Figure 6.
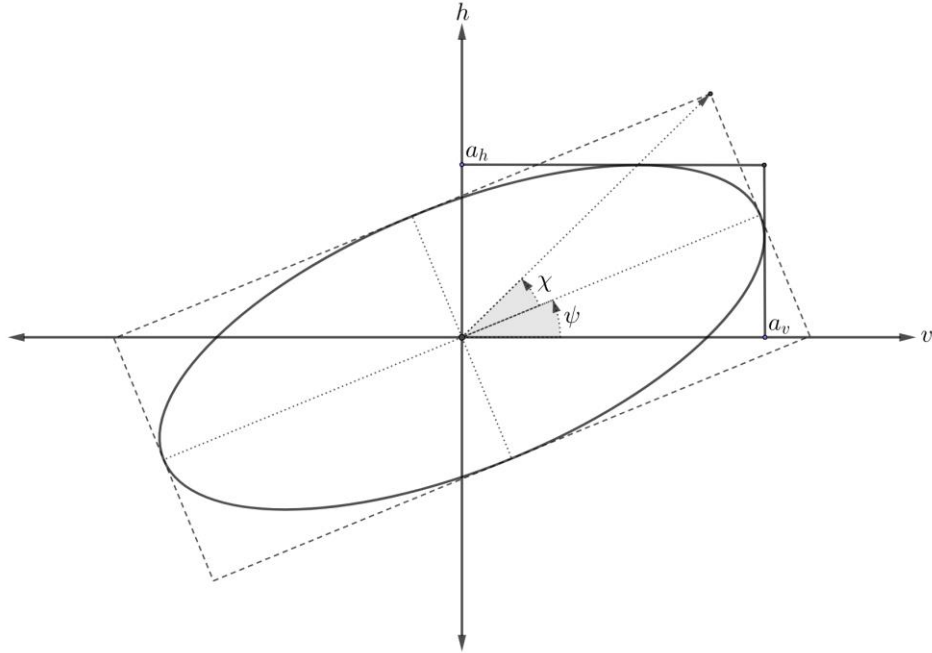
Figure 6: Polarisation ellipse where ψ denotes the orientation of the major axis with respect to the vertical direction and χ denotes the ellipticity angle.

The shift in the polarisation orientation angle occurs due to the rotation of polarisation with respect to the line of sight of the wave, caused by the azimuthal slope (Pottier, Schuler, Lee, & Ainsworth, 1999). Lee, Schuler, and Ainsworth, (2000) presented three important approaches for estimation of POA shift, the first approach is to derive the orientation angle from the Digital Elevation Model (DEM) (Lee et al., 1998), the second method makes use of Cloude's target decomposition (Cloude & Pottier, 1996) or Huynen decomposition (Huynen, 1970) to estimate the POA shift and the last approach is circular polarisation based (Pottier et al., 1999). However, circular polarisation based estimation of POA shift yields the most reliable results (Lee et al., 2000). According to Lee, Schuler, Ainsworth, and Boerner, (2003) the orientation angle (ψ) can be estimated from observed scattering matrix ([S]), using equation (22).

$$\psi = \begin{cases} \eta & \text{If } \eta \leq \frac{\pi}{4} \\ \eta - \frac{\pi}{2} & \text{If } \eta > \frac{\pi}{4} \end{cases} \tag{22}$$

Where,

$$\eta = \frac{1}{4}\left[\tan^{-1}\left(\frac{-4\Re(\langle(S_{HH} - S_{VV})S_{HV}\rangle)}{-\langle|S_{HH} - S_{VV}|^2\rangle + 4\langle|S_{HV}|^2\rangle}\right) + \pi\right]$$

$$\tan^{-1} : \mathbb{R} \rightarrow [-\pi, \pi]$$

The compensated scattering matrix ($[\tilde{S}]$) can be obtained using equation (23).

$$\begin{bmatrix} \tilde{S}_{HH} & \tilde{S}_{HV} \\ \tilde{S}_{VH} & \tilde{S}_{VV} \end{bmatrix} = \begin{bmatrix} \cos\psi & \sin\psi \\ -\sin\psi & \cos\psi \end{bmatrix} \begin{bmatrix} S_{HH} & S_{HV} \\ S_{VH} & S_{VV} \end{bmatrix} \begin{bmatrix} \cos\psi & -\sin\psi \\ \sin\psi & \cos\psi \end{bmatrix} \tag{23}$$

2.7. Metrics of Data Quality

Maximum Normalised Error (MNE)

The maximum normalised error (MNE) proposed by Wang et al., (2011) is an adequate metric to evaluate the polarimetric distortions present in the PolSAR data. The error ($[E]$) in the polarimetric measurement can be derived using as the equation (24). Here, ($[S]$) is the scattering matrix, ($[M]$) is the distortion matrix derived from the equation (10) and $[I]$ is the identity matrix.

$$[E] = ([M] - [I])[S] \tag{24}$$

Therefore, the MNE can be estimated as presented in equation (25), which can be further represented as shown in equation (25).

$$\omega_{MNE} = \max_{S}(|E|/|S|) \qquad \dots \text{(a)}$$

$$\omega_{MNE} = \sqrt{\lambda_{max}\left[A_n^{\dagger}([M] - [I])^{\dagger}([M] - [I])A_n\right]} \qquad \dots \text{(b)} \tag{25}$$

Where,

λ_{max} : Largest eigen value of the enclosed matrix

A_n: Matrix compensating for the dimensionality mismatch due to reciprocity of cross-pol channels

Signal to Noise Ratio (SNR) of Cross-pol Channels

SNR is a direct measure of data quality depicting the ratio of information content concerning the noise present in the dataset. In the case of Bragg surface, ideally, the two cross-pol channels should be equal, provided, there are no distortions in the data (Villano & Papathanassiou, 2013). Consequently, the variance of the distortions can be roughly estimated from the cross-pol backscattering of a known Bragg surface. Furthermore, the cross-pol backscattering from Bragg surface is low, i.e. mean of the cross-pol backscattering is zero and variance equal to its RCS (Villano & Papathanassiou, 2013). The cross-pol SNR (SNR_X) can be derived from these two assumptions by calculating the ratio of the variance of the RCS (A_0^2) and the variance of the distortion (σ_N^2) as shown in the equation (26) (Villano & Papathanassiou, 2013).

$$SNR_X = \frac{A_0^2}{\sigma_N^2} \tag{26}$$

In this regard, the SNR of cross-pol channels is especially important as it not only represents the data quality but also takes into account the distortions present in the data (Villano & Papathanassiou, 2013). The maximum likelihood of the cross-pol SNR can be estimated as shown in equation (27) (Villano & Papathanassiou, 2013).

$$\hat{S}_{ML} = \frac{2\sum_{i=0}^{N-1}\Re(s_{hv}^*(i)s_{vh}(i))}{\sum_{i=0}^{N-1}|s_{hv}(i) - s_{vh}(i)|^2} \tag{27}$$

Villano & Papathanassiou, (2013) presented a statistically unbiased method to measure the SNR of cross-pol channels in the PolSAR data as presented in equation (28).

$$\hat{S}_{unbiased} = \left(\frac{N-1}{N}\right)\hat{S}_{ML} + \left(\frac{1}{2N}\right) \tag{28}$$

Polarimetric Signature

Polarimetric signatures provide information regarding the scattering pattern of the target (van Zyl, Zebker, & Elachi, 1987). The polarimetric signature can be generated using electromagnetic wave synthesis. The synthesised scattering matrix ($[S_{syn}]$) can be generated from the actual scattering matrix ($[S]$) with respect to varying ellipticity angle (χ) and orientation angle (ψ) as shown in equation (29) (ESA & European Space Agency, 2017).

$$[S_{syn}] = [R_\psi][S][R_\chi] \tag{29}$$

Where,

$$[R_\psi] = \begin{bmatrix} \cos\psi & -\sin\psi \\ \sin\psi & \cos\psi \end{bmatrix}, \; [R_\chi] = \begin{bmatrix} \cos\chi & -j\sin\chi \\ -j\sin\chi & \cos\chi \end{bmatrix}$$

Accordingly, the voltage (V_{oc}) of the backscatter can be obtained from the synthesised scattering matrix ($[S]$) and the complex effective length vector of the antenna ($\underline{h}$) using equation (30) (Cloude, 2009). The comparison of observed and theoretical polarimetric signature of known targets can provide hints regarding the quality of the radiometric and phase calibration (Fore, Chapman, Hensley, Michel, & Muellerschoen, 2009).

$$V_{oc} = \underline{h}^T[S_{syn}]\underline{h} \tag{30}$$

Roll Invariant Parameters and Polarimetric Decomposition

The Cloude & Pottier, (1996, 1997) decomposition theorem states that the entropy (H), anisotropy (A) and scattering angle (α) are roll invariant parameters, i.e. these parameters are invariant irrespective of the variation of polarisation basis (Touzi, 2007), therefore they are suitable indicator of scattering characteristics of the target. The entropy indicates the randomness in the scattering pattern and the scattering angle denotes the scattering type. Cloude & Pottier, (1997) devised an unsupervised classification algorithm based on the scattering property of the target evaluated from the two dimensional H-α plane. Nine separate zones have been identified in the H-α plane, each corresponding to a unique class as shown in Figure 7. Additionally, the model based polarimetric decomposition methods are also useful for characterising the scattering patterns (Cloude, 2009). A comparative study by Sato, Watanabe, Yamada, & Yamaguchi, (2013) shows that the Yamaguchi four component decomposition (Y4R) is highly robust and provides reliable scattering patterns irrespective of the targets present in the scene.
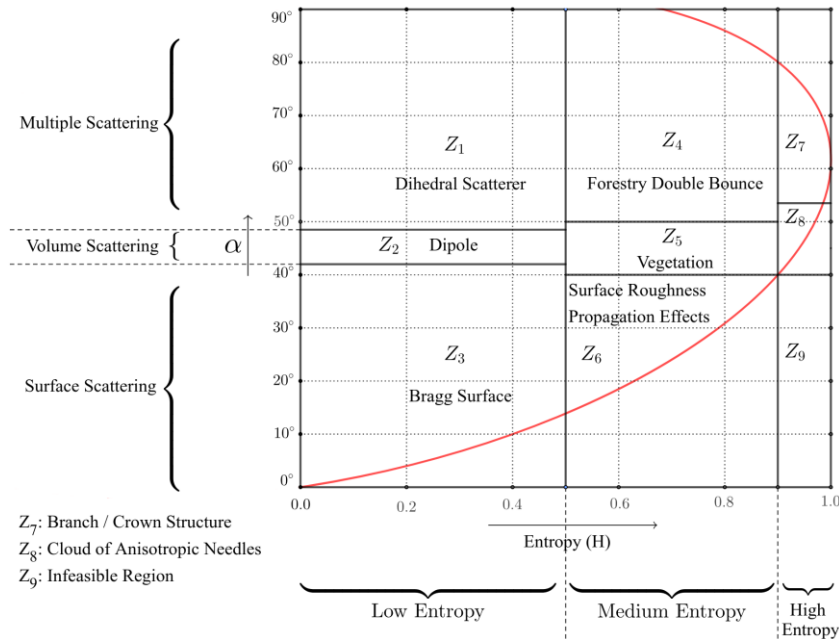
Figure 7: H-α plane showing different zones and their class labels. The curve in red denotes the overall boundary of the feasible regions

2.8.   Chapter Summary

In this chapter, the technical aspects of the different PolSAR calibration algorithms along with their necessary assumptions have been discussed. Moreover, the impact of design and choice of external calibrators on the radiometric and channel imbalance calibration have been briefly described. Additionally, the basic principles of SAR systems and the working of its spaceborne and airborne variants have been summarised. In the subsequent chapters, specific discussion regarding this thesis is provided.

3.   METHODOLOGY

This chapter describes the adopted methodology adopted for this study in detail. The overview of the adopted methodology has been shown in Figure 8. The workflow involves one data preprocessing step and three significant processing steps. Additionally, one analysis step has been incorporated into the methodology in order to estimate the effect of calibration on the dataset.
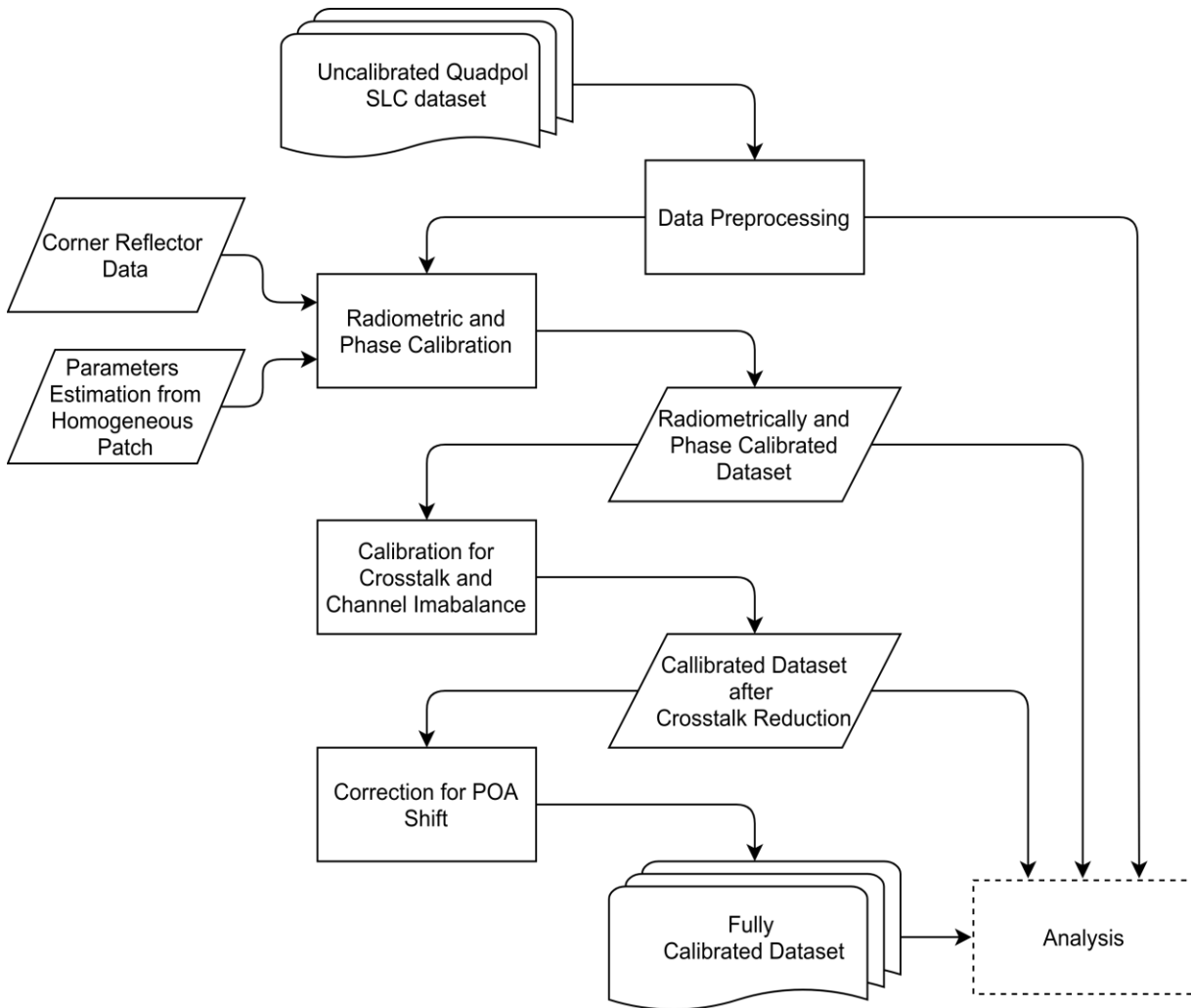
Figure 8: Overview of the Adopted Methodology

3.1.   Data Preprocessing

Each polarisation channel of the original dataset consists of 61349 rows and 9874 columns; however, a subset of 1914 rows and 2745 columns containing all the visible corner reflectors has been considered for this study. An overview of the effective study area is presented in Figure 10. Furthermore, in order to maintain compatibility with other software, the original dataset has been converted into ENVI file format with the precision of 64-bit complex number from the original binary image format having the same precision. Since the precision of the dataset is the same before and after the conversion, this file format conversion is lossless.

3.2. Radiometric and Phase Calibration

Radiometric and phase calibrations are the crucial preceding steps of any polarimetric calibration (Fore et al., 2015). The phase calibration helps in minimising the phase bias present in both co-pol channels and cross-pol channels whereas, the purpose of the radiometric correction is to correctly convert pixel values to corresponding normalised RCS (Freeman, 1992). Assuming that the correction for antenna pattern has already been applied and neglecting the crosstalk, the radiometric and phase calibration can be modelled as given in equation (31) (Fore, Chapman, Hensley, Michel, & Muellerschoen, 2009).

$$S' = A \begin{bmatrix} s_{vv}f^2 e^{i(\phi_{t,v}+\phi_{t,r})} & s_{vh}(f/g)e^{i(\phi_{t,h}+\phi_{r,v})} \\ s_{hv}fg e^{i(\phi_{t,v}+\phi_{r,h})} & s_{hh}e^{i(\phi_{t,h}+\phi_{r,h})} \end{bmatrix} \tag{31}$$

Where,

$S' = \begin{bmatrix} s'_{vv} & s'_{vh} \\ s'_{hv} & s'_{hh} \end{bmatrix}$:   Radiometric and phase calibrated scattering matrix, where s_{tr} is the back scattering from transmitted polarisation t and received polarisation r.

$S = \begin{bmatrix} s_{vv} & s_{vh} \\ s_{hv} & s_{hh} \end{bmatrix}$:   Observed scattering matrix, where s_{tr} is the back scattering from transmitted polarisation t and received polarisation r.

A: Absolute calibration parameter.

f: Co-pol channel imbalance parameter.

g: Cross-pol channel imbalance parameter.

$\phi_{x,y}$:   Phase error in polarisation channel y where x signifies whether it corresponds to transmission (t) or reception (r).

After the removal of the arbitrary phase, equation (31) reduces into equation (32) (Fore et al., 2009).

$$S' = A \begin{bmatrix} s_{vv}f^2 e^{i(\phi_t+\phi_r)} & s_{vh}(f/g)e^{i\phi_r} \\ s_{hv}fg e^{i\phi_t} & s_{hh} \end{bmatrix} \tag{32}$$

Where,

$\phi_t \equiv \phi_{t,v} - \phi_{t,h}$

$\phi_r \equiv \phi_{r,v} - \phi_{r,h}$

3.2.1. Estimation of Radiometric Calibration Parameters

The absolute calibration parameter (A) is obtained from the ratio of theoretically predicted RCS and the measured RCS of HH polarisation channel at the peak of the oversampled corner reflectors by solving equation (33) (Fore et al., 2009).

$$10\log_{10}\left[\frac{\sigma_{cr}}{(s_{hh}s_{hh}^*)}\right] = -10\log_{10}(A^2) \tag{33}$$

In this regard, the theoretical RCS of a triangular trihedral corner reflector (σ_{cr}) can be estimated as shown in equation (34) (Fore et al., 2009).

$$\sigma_{cr} = \frac{4\pi l^4}{\lambda^2}\left[\Omega(\theta_{cr},\phi_{cr}) - \frac{2}{\Omega(\theta_{cr},\phi_{cr})}\right] \tag{34}$$

Where,

$\Omega(\theta_{cr},\phi_{cr}) = \cos\theta_{cr} + (\sin\phi_{cr} + \cos\phi_{cr})\sin\theta_{cr}$

θ_{cr}: Incidence angle relative to the triangular trihedral corner reflector.
ϕ_{cr}: Azimuth angle.
l: Length of the inner side of the triangular trihedral corner reflector.
λ: Wavelength of the radar signal.

All the absolute calibration parameters obtained from each of the corner reflectors distributed over the scene are regressed with respect to the corresponding incidence angles as shown in equation (35) (Fore et al., 2009).

$$A(\theta') = \sum_{i=0}^{n} A_i(\theta')^i \tag{35}$$

Where,
A_i: Coefficients of the fitted polynomial
$\theta': \theta - \theta_m$
θ: Incidence Angle
θ_m: Mounting angle of the radar antenna
n: Degree of polynomial

Accordingly, the co-pol channel imbalance parameter (f_i) has been estimated using equation (36) on each of the corner reflectors and the mean value of them has been considered as the effective value of f as shown in equation (36).

$$f_i = \left[\frac{(s_{vv}s_{vv}^*)}{(s_{hh}s_{hh}^*)} \right]^{\frac{1}{4}} \qquad \dots a \tag{36}$$
$$f = \bar{f_i} \qquad \dots b$$

Where,
f_i: Co-pol channel imbalance parameter
f_i: Estimation of parameter f at i[th] corner reflector

Finally, the cross-pol channel imbalance parameter (g) has been derived from a sufficiently large homogeneous featureless patch of the scene according to equation (37).

$$g = \left[\frac{\langle s_{hv}s_{hv}^* \rangle}{\langle s_{vh}s_{vh}^* \rangle} \right]^{\frac{1}{4}} \tag{37}$$

3.2.2. Estimation of Phase Calibration Parameters

The term $\phi_t + \phi_r$ is estimated as the phase anomaly between the HH and VV channels at each of the corner reflector points as shown in equation (38) (Fore et al., 2009). These values are regressed against corresponding incidence angles forming a polynomial in the form of equation (39), where the degree of the polynomial (n) chosen optimally.

$$\phi_s = \arg(s_{vv}s_{hh}^*) \tag{38}$$

Where,
$\phi_s = \phi_t + \phi_r$

$$\phi_s(\theta') = \sum_{i=0}^{n} c_i(\theta')^i \tag{39}$$

Where,

$\theta': \theta - \theta_m$

θ: Incidence Angle

θ_m: Mounting angle of the radar antenna

c_i: i^{th} coefficient of the polynomial

n: Degree of the polynomial

Similarly, the term $\phi_t - \phi_r$ can be estimated from the average phase bias between the cross-polarisation channels, from a large homogeneous patch, as given in equation (40).

$$\phi_d = \arg(\langle s_{hv}s_{vh}^* \rangle) \tag{40}$$

Where,

$\phi_d = \phi_t - \phi_r$

Now, ϕ_t and ϕ_r can be simply solved from the estimated values of ϕ_s and ϕ_d as shown in equations (41) and (41).

$$\phi_t = \frac{\phi_s + \phi_d}{2} \qquad \ldots a$$
$$\phi_r = \frac{\phi_s - \phi_d}{2} \qquad \ldots b \tag{41}$$

3.2.3. Summary

The overview of the radiometric calibration is shown in Figure 9. First, the parameters f, g and ϕ_d are estimated from equations (36), (37) and (40) respectively as these terms do not vary with respect to incidence angle and therefore, are constants.
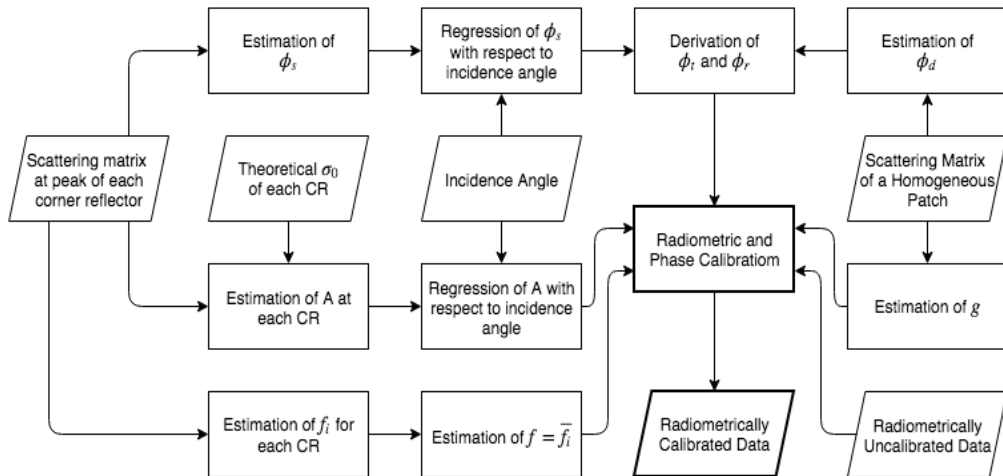

Figure 9: Workflow for the radiometric and phase calibration

In addition to this, parameters $A(\theta')$ and $\phi_s(\theta')$ are estimated for each pixel using equations (35) and equation (39), given the incidence angle (θ) of a pixel and the antenna mounting angle of the radar (θ_m).

After that, ϕ_t and ϕ_r are derived from $\phi_s(\theta')$ and ϕ_d according to equation (41). Finally, radiometric and phase calibration has been applied according to equation (31).

3.3. Calibration for Crosstalk and Channel Imbalance

The radiometric and phase calibrated SAR data are partially calibrated as the channel imbalance is not entirely minimised and crosstalk is still present in the dataset. Typically, the crosstalk parameters are estimated from the covariance matrix; therefore the specifics of covariance matrix generation are essential for the correct estimation of crosstalk and channel imbalance parameters. Furthermore, there are different existing algorithms for the estimation of the crosstalk parameters as described in section 2.5. In this regard, the choice of the algorithm also affects the accuracy of the overall PolSAR calibration. The details of these procedures are discussed in the subsequent subsections.

3.3.1. Covariance Matrix Generation

The polarimetric covariance matrix ($[C_4]$) is computed from the vector form of the scattering matrix of fully polarimetric SAR data using equation (42) and it has the form shown in equation (43) (Fore et al., 2015).

$$[C_4] = \langle [S][S]^\dagger \rangle \tag{42}$$

Where,
$$[S] = [s_{hh} \quad s_{vh} \quad s_{hv} \quad s_{vv}]^T$$

$$[C_4] = \begin{bmatrix} \langle s_{hh}s_{hh}^* \rangle & \langle s_{hh}s_{vh}^* \rangle & \langle s_{hh}s_{hv}^* \rangle & \langle s_{hh}s_{vv}^* \rangle \\ \langle s_{vh}s_{hh}^* \rangle & \langle s_{vh}s_{vh}^* \rangle & \langle s_{vh}s_{hv}^* \rangle & \langle s_{vh}s_{vv}^* \rangle \\ \langle s_{hv}s_{hh}^* \rangle & \langle s_{hv}s_{vh}^* \rangle & \langle s_{hv}s_{hv}^* \rangle & \langle s_{hv}s_{vv}^* \rangle \\ \langle s_{vv}s_{hh}^* \rangle & \langle s_{vv}s_{vh}^* \rangle & \langle s_{vv}s_{hv}^* \rangle & \langle s_{vv}s_{vv}^* \rangle \end{bmatrix} \tag{43}$$

Here, $\langle \cdot \rangle$ signifies the ensemble average operation. In this regard, the choice of kernel size in covariance matrix computation is crucial as it can affect the estimation of crosstalk parameters. Ideally, the kernel size should not be too large as the covariance may deviate from expected value due to the high variation in sizeable spatial extent, on the other hand, it should not be too small as the correct estimation of covariance requires an adequate number of samples (pixels) to be present in the kernel.

3.3.2. Estimation of Channel Imbalance

Appropriate radiometric and phase calibration partially rectifies the channel imbalance present in the data. Thus, after radiometric and phase calibration the channel imbalance parameters k, α satisfies the condition in equation (44).

$$k = \frac{1}{\sqrt{\alpha}} \tag{44}$$

The term α is later estimated at the time of crosstalk estimation. The estimation of α varies depending upon the crosstalk model. In the case of Quegan's algorithm, α is estimated according to equations shown in (14) given in the section 2.5.1. Similarly, in the improved Quegan's crosstalk model, α is estimated using equations in (15), provided in the section 2.5.2. Since Ainsworth algorithm follows an iterative approach the value of α is also adjusted iteratively. However, in this case, the initial value of α is directly determined from the covariance matrix (C_4), according to equation (45) (Fore et al., 2015).

$$\alpha = \frac{C_{23}}{|C_{23}|} \sqrt{\left|\frac{C_{22}}{C_{33}}\right|} \tag{45}$$

3.3.3. Estimation of Crosstalk Parameters

In this study, three well-established algorithms, namely Quegan's algorithm, improved Quegan's algorithm and Ainsworth algorithm have been applied to estimate the crosstalk parameters. These algorithms are discussed in section 2.5. Furthermore, a modified Ainsworth algorithm has been proposed to improve the computational efficiency. It is worth mentioning that the crosstalk parameters vary with respect to the range; therefore the pixels having the same range should correspond to a single set of crosstalk parameters. Due to this reason, a set of crosstalk parameters comprising the mean of each crosstalk parameter estimated from pixels having the same range is considered to be the estimation of the crosstalk for that range.

Crosstalk Estimation using Quegan's Algorithm

The Quegan's crosstalk model has been described in section 2.5.1. The estimation of crosstalk using Quegan's algorithm is straight forward. First, the term Δ is calculated from the covariance matrix using equation (13). Then the crosstalk parameters u, v, w, z are estimated using equations (13), (13), (13) and (13) respectively.

The correlations between the co-pol and cross-pol channels are defined as shown in equation (46).

$$r_1(s_{hh}, s_{vh}^*) = \frac{\langle s_{hh}s_{vh}^* \rangle}{\sqrt{\langle |s_{hh}|^2 \rangle \langle |s_{vh}|^2 \rangle}} \qquad \dots a$$
$$r_2(s_{vv}, s_{hv}^*) = \frac{\langle s_{vv}s_{hv}^* \rangle}{\sqrt{\langle |s_{vv}|^2 \rangle \langle |s_{hv}|^2 \rangle}} \qquad \dots b \tag{46}$$

It is worth mentioning that, the Quegan's crosstalk model assumes that the co-pol cross-pol channels are entirely uncorrelated. However, in practice, the correlations between co-pol and cross-pol channels cannot be absolute zero. Therefore, the crosstalk parameters should only be estimated from the pixels where the correlations between co-pol and cross-pol channels are very low. Consequently, a sufficiently small threshold value for these correlations has been chosen so that the pixels having the cross-pol correlation less than this threshold is considered to have effectively uncorrelated co-pol and cross-pol channels. It implies that the crosstalk parameters will only be estimated from the pixels where the cross-pol correlation is below the predetermined threshold.

Improved Quegan's Algorithm

According to the discussion in section 2.5.2, if imbalanced cross-pol noise is present in the dataset, the estimation of channel imbalance provided by Quegan, (1994) will largely deviate from the actual value. Therefore, imbalanced cross-pol noise should be compensated as shown in equations in (15). However, the estimations of the crosstalk parameters, in this case, are identical to that of the Quegan's algorithm, and the same correlation-based approach is followed as discussed in the Crosstalk Estimation using Quegan's Algorithm.

Crosstalk Estimation using Ainsworth Algorithm

The Ainsworth algorithm adopts an iterative approach for the estimation of the crosstalk parameters. The crosstalk model by Ainsworth et al., (2006) has been described in section 2.5.3. Here, the algorithm code for crosstalk parameters estimation is as follows (Fore et al., 2015):

Ainsworth Algorithm

Input covariance matrix $[C_0]$
Input maximum iteration count i_{max}
Input precision threshold ε
Initialize crosstalk parameters $u = v = w = z = 0$
Compute channel imbalance parameter α using equation (45)
Set iteration count $i = 0$
do
        Increment iteration count $i = i + 1$
        Compute C_i using equations (20) and (18)
        Estimate $[\delta]$ from $[C_i]$ by solving equations in (19)
        Update u, v, w, z and α with values in δ using equations in (21)
        Set $\gamma = \max([\delta_{abs}]) : \forall\, x \in [\delta] \Rightarrow |x| \in [\delta_{abs}]$
while $\gamma > \varepsilon$ and $i < i_{max}$

The algorithm starts with a crude estimation of channel imbalance while assuming crosstalk is not present in the data. Then the calibration is iteratively applied on the covariance matrix, and residual crosstalk is observed. In each iteration, the crosstalk parameters are updated by scaling the respective residuals of crosstalk by channel imbalance, and the channel imbalance is updated by the residual channel imbalance. The iteration stops when the absolute value of all the crosstalk residuals are below the predetermined threshold. For this reason, the threshold value has been chosen as per the requirement of the precision in the estimation. Furthermore, the purpose of providing the maximum iteration count is to avoid indefinite execution of the iterations in case the crosstalk parameters do not converge as per expectation. Therefore, the maximum number of iterations is chosen heuristically.

Proposed Algorithm

The Ainsworth algorithm adopted by Fore et al., (2015) does not take into account the system noise. According to Ainsworth et al., (2006) the term η as given in equation (47a) represents the system noise and the term q in equation (47b) depicts the data quality .

$$
\begin{aligned}
\eta &= \beta - \beta' && \dots \text{a} \\
q &= \frac{\eta}{\beta} && \dots \text{b}
\end{aligned}
\qquad (47)
$$

Where,
β and β' refer to the respective terms in the covariance matrix according to Ainsworth's crosstalk model presented in equation (16).

When, $q > 1$, the covariance matrix is not positive definite. This implies that, either the data contains less polarimetric information compared to the noise present in it or the Ainsworth's crosstalk model does not apply in this case. Consequently, the estimation of crosstalk parameters from these covariance matrices reduces the overall accuracy of the crosstalk estimation as the crosstalk parameters are averaged from the pixels having constant range. The proposed method incorporates this measure by ignoring the pixels where $q > 1$. In contrast, the Ainsworth algorithm is iterative in nature and its computational complexity is higher than the Quegan's algorithm. Although the estimations of crosstalk parameters using Quegan's algorithm are no better than the Ainsworth algorithm, in some cases the Quegan's crosstalk estimations are very close to the result of the Ainsworth's algorithm. Therefore, in those cases, Ainsworth's iterative computations can be avoided by increasing the computational efficiency and saving execution time.

Furthermore, the crosstalk parameters may not converge to the expected precision within the maximum allowed iterations, i.e. $\gamma \leq \varepsilon$ may not be satisfied when $i = i_{max}$ has been reached. There is a possibility that the value of γ the Quegan's algorithm can better than the γ value from Ainsworth algorithm when $i = i_{max}$ i.e. equation (48) holds true.

$$\gamma_A > \gamma_Q \tag{48}$$

Where,

γ_Q : γ of the crosstalk parameters derived by Quegan's algorithm

γ_A : γ of the crosstalk parameters derived by Ainsworth algorithm when $i = i_{max}$

Therefore, in these cases, the Quengan's estimations are better than that of Ainsworth algorithm. The proposed algorithm takes this into account and accepts Quegan's solution, in case the condition in (48) is satisfied. Thus, the proposed algorithm is as follows:

Proposed Algorithm

Input covariance matrix $[C_0]$
Input maximum iteration count i_{max}
Input precision threshold ε
Estimate q using equation (47
If $q < 1$

    Estimate u_q, v_q, w_q, z_q and α_q using Quegan's algorithm in equations (13) and (14)
    Compute C_q using equations (20) and (18)
    Estimate $[\delta_q]$ from $[C_q]$ by solving equations in (19)
    Set $\gamma_Q = \max\left([\delta_{abs_q}]\right) : \forall x \in [\delta] \Rightarrow |x| \in [\delta_{abs_q}]$
    If $\gamma_Q < \varepsilon$
        Accept Quegan's solution: $u = u_q, v = v_q, w = w_q, z = z_q, \alpha = \alpha_q$
    Else
        Initialize $u_a = v_a = w_a = z_a = 0$
        Compute channel imbalance parameter α_a using equation (45)
        Set iteration count $i = 0$
        do
            Increment iteration count $i = i + 1$
            Compute C_i using equations (20) and (18)
            Estimate $[\delta]$ from $[C_i]$ by solving equations in (19)
            Update u_a, v_a, w_a, z_a and α_a with values in δ using equations in (21)
            Set $\gamma = \max([\delta_{abs}]) : \forall x \in [\delta] \Rightarrow |x| \in [\delta_{abs}]$
        while $\gamma > \varepsilon$ and $i < i_{max}$
        If $i = i_{max}$
            $\gamma_A = \gamma$
            If $\gamma_A > \gamma_Q$
                Accept Quegan's solution: $u = u_q, v = v_q, w = w_q, z = z_q, \alpha = \alpha_q$
            Else
                Accept Ainsworth's solution: $u = u_a, v = v_a, w = w_a, z = z_a, \alpha = \alpha_a$
Else
    Ignore crosstalk estimation: $u = \text{NaN}, v = \text{NaN}, w = \text{NaN}, z = \text{NaN}, \alpha = \text{NaN}$

3.3.4. Correction of Crosstalk

After the estimation of crosstalk, the calibration can be performed according to a generic crosstalk model is shown in equation (17). Since the random system noise ($[N]$) is assumed to be zero, the actual scattering matrix ($[S]$) can be derived from the observed scattering matrix ($[S']$) using equation (49).

$$[S] = [M]^{-1}[S']$$
(49)

Where,

$[M]$: As defined in equation (18)

Although $[M]^{-1}$ can be computed numerically; the analytical solution of matrix inversion is advantageous considering the computational cost. Therefore, $[M]^{-1}$ can be calculated as shown in equation (50). It is worth mentioning that, the same approach can be applied for the estimation of Σ in equation (20).

$$[M]^{-1} = \frac{1}{(uw-1)(vz-1)}\begin{bmatrix} 1 & -w & -v & vw \\ -u/\sqrt{\alpha} & 1/\sqrt{\alpha} & uv/\sqrt{\alpha} & -v/\sqrt{\alpha} \\ -z\sqrt{\alpha} & wz\sqrt{\alpha} & \sqrt{\alpha} & -w\sqrt{\alpha} \\ uz & -z & -u & 1 \end{bmatrix}$$
(50)

Where,

u, v, w, z : Estimated crosstalk parameters
α : Estimated channel imbalance parameter

3.3.5. Estimation and Correction of POA Shift

As discussed in section 2.6, the variations in topography cause the shift in polarisation orientation angle, and this shift can be estimated with the help of equation (22), and its effect can be corrected using equation (23). However, POA shift should be estimated and corrected after the radiometric and crosstalk calibration has been performed so that the deviation from the accurate estimation of POA shift can be avoided due the presence of anomalies in the uncalibrated dataset.

3.4. Metrics of Data Quality and Validation

According to Wang et al., (2011) the MNE is an important metric to check the polarisation distortion in PolSAR data. SNR is another generalised metric to evaluate the amount of useful information present in the data with respect to the noise. Villano & Papathanassiou, (2013) suggested that the SNR of cross-pol channels of SAR data is crucial since the powers of the backscattered signal are comparatively very low with respect to backscatter powers of the co-pol channels. Therefore, MNE and cross-pol SNR have been chosen as the data quality metrics for this study. Along with this, the polarimetric signature has been used in order to validate the scattering behaviour of the known targets.

Additionally, the scattering pattern of the scene has been studied through the $H\text{-}\alpha$ plane. As discussed in section the topographic variation causes POA shift and as a result generally volume scattering is over estimated and even bounce scattering is under estimated. Therefore, if the POA shift is present in the dataset, the subsequent changes should necessarily be reflected in the scattering patterns depicted by decomposition modelling. According to the study by Sato et al., (2013) the Y4R decomposition is highly reliable for estimating the true scattering pattern. Therefore, Y4R decomposition has been selected for observing the changes in the scattering pattern due to POA shift correction.

4.   STUDY AREA AND DATASET

This chapter briefly describes the study area and the dataset used in this research. Furthermore, it introduces the software and tools required for this study.

4.1.   Study Area

Rosamond dry lake is situated between Antelope Valley and the Mojave Desert in the southern part of California, United States of America. It is a naturally formed dry lake bed with a large flat surface of nearly 35 km² (Meyer & Bowers, 2012). The area is characterized by a hard surface having less than 40 cm of variation in curvature over a distance of 9 km and with least amount of vegetation, thus making it suitable for a calibration validation (cal-val) site. For these unique characteristics, this site is being used as a permanent cal-val site by NASA (Muellerschoen & Muellerschoen Ronald, 2018). At the southern part of the lake, an array of 38 triangular trihedral corner reflectors of different sizes has been deployed for the calibration of SAR instruments (Muellerschoen & Muellerschoen Ronald, 2018). These reflectors are routinely maintained and. The size of the different corner reflectors with respective count is presented in Table 1. A large dry flat area with the presence of the corner reflectors array of different sizes makes this area suitable for this study. Furthermore, it is relatively easy to access the dataset of different levels because of the open data policy of NASA (NASA, 2015).

Table 1: Size and Count of Corner Reflectors in Rosamond Corner Reflector Array

The side length of triangular trihedral corner reflector (m)	Total count
4.8	5
2.4	23
0.7	10

4.2.   Dataset

This study requires uncalibrated data; therefore the UAVSAR (Rosen et al., 2006) L band uncalibrated dataset has been used. The details of the dataset are provided in Table 2. Since the dataset is not calibrated for crosstalk and POA shift, it is suitable for crosstalk calibration and POA shift correction. This particular dataset pre-processed up to level 1.1, and it has a 1.8 m slant range resolution and 0.8 m azimuth resolution.

Table 2: Details of the dataset

Attribute	Value
Date and Time of Acquisition	September 20, 2016, 22:31:22 UTC
Site	Rosamond, California, USA
Acquisition Mode	Quad Pol
Flight Line	35012
Track ID	35
Average Altitude	1.25 km
Look Direction	Left
Radiometric Calibration Applied	Yes
Frequency Band	L (1.2575 GHz)

The intensity image of HH channel is depicted in Figure 10, with the visible corner reflectors marked in circles. The bright portion near the top is a slightly rough surface with mild vegetation and marks the boundary of the dry lake. Rest of the area is nearly featureless. The area near the top right appears comparatively dark indicating smooth surface and presence of soil moisture as the Piute ponds are located in the close neighbourhood.
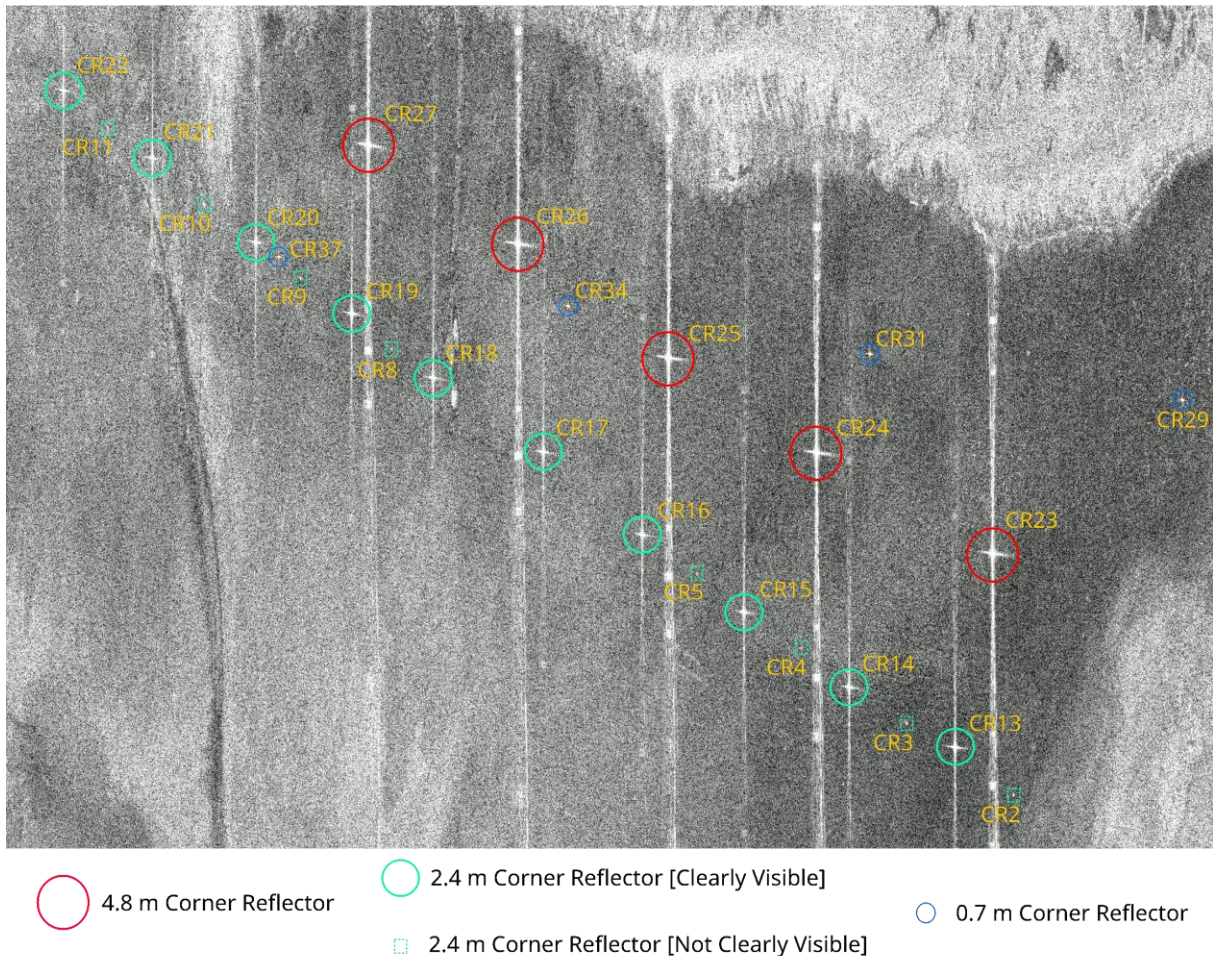

Figure 10: Visible corner reflectors in the HH intensity image acquired on September 20, 2016

There are ten 2.4 m corner reflectors, and all five 4.8 m corner reflectors are visible in the scene. Additionally, four 0.7 m corner reflectors are also visible but those are not useful in this study as the wavelength of the SAR sensor is 0.24 m. Some corner reflectors are not prominently visible as their viewing vector were away from the sensor at the time of acquisition.

4.3.   Softwares

This study has been carried out using the following software.
- Python 3 (Python Core Team, 2018) and required modules for processing
- ENVI 5.3 for visualisation of the dataset
- PolSARpro v5.1.3 for assessment

4.4.   Chapter Summary

In this chapter, a general overview of the study area and dataset has been provided. Additionally, the requirements of different software and tools along with their specific purpose has been specified.

5.   RESULT AND ANALYSIS

This chapter presents the results of this study and summarises the analysis of these results. Section 5.1 ensures that the dataset is radiometrically calibrated. Section 5.2 and 5.3 provides the results and the analysis of the Quegan's algorithm and the improved Quegan's algorithm while section 5.4 concerned with the results and the analysis of the Ainsworth algorithm. Section 5.5 describes the results and analysis of the proposed algorithm. Section 5.6 compares the algorithms in terms of scattering angle and entropy. Section 5.7 shows the effect of POA shift correction. Finally, the chapter ends with a summary in section 5.8.

The estimated covariance matrix depends upon the choice kernel size, which in turn affects the estimation of crosstalk parameters. Henceforth, all the covariance matrices have been computed using the 7×7 kernel. Furthermore, in each case, the cross-pol SNR has been estimated from a featureless area of 286×263 pixels with a 7×7 window. For the iterative crosstalk estimation algorithms, the maximum allowed iterations are set to be 16. Similar to the computation of the covariance matrix, the 7×7 window has been used for the estimation of POA shift.

5.1.   Verification of Radiometric Calibration

The radiometric and phase calibration has already been applied in the dataset. Therefore, the shapes of the polarimetric signatures at the corner reflector pixels should closely resemble the ideal shapes. The polarimetric signature of a 4.8 m triangular trihedral corner reflector is shown in Figure 11.
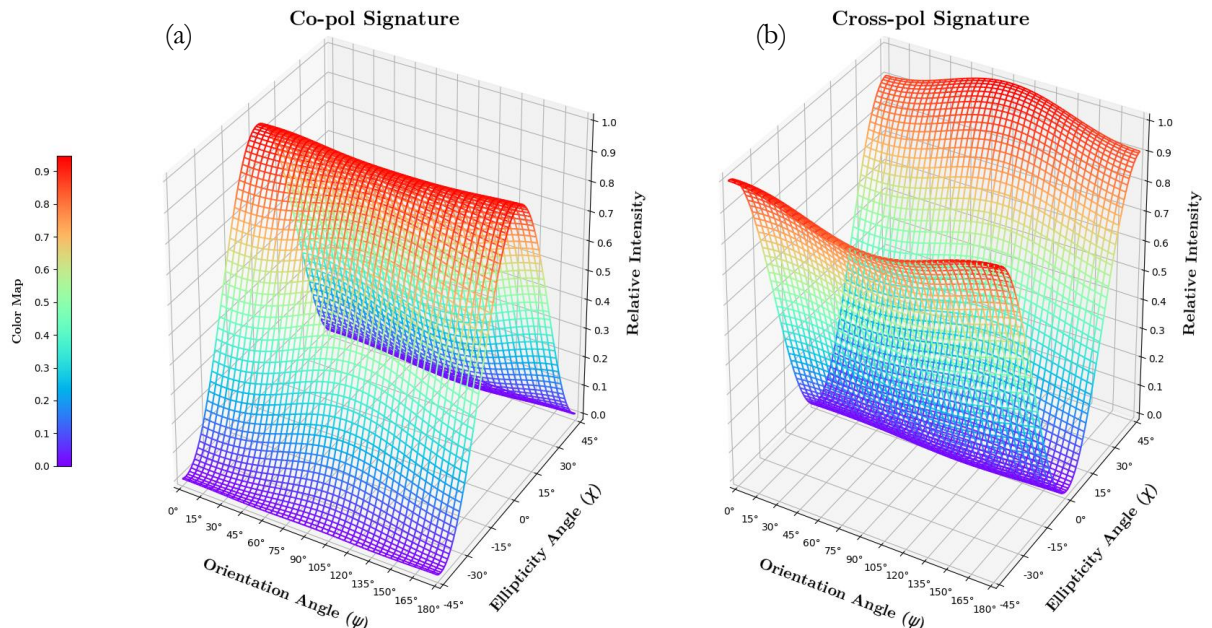

Figure 11: Polarimetric signatures of corner reflector 24. It is a triangular trihedral corner reflector with 4.8 m side length, (a) co-pol signature, (b) cross-pol signature
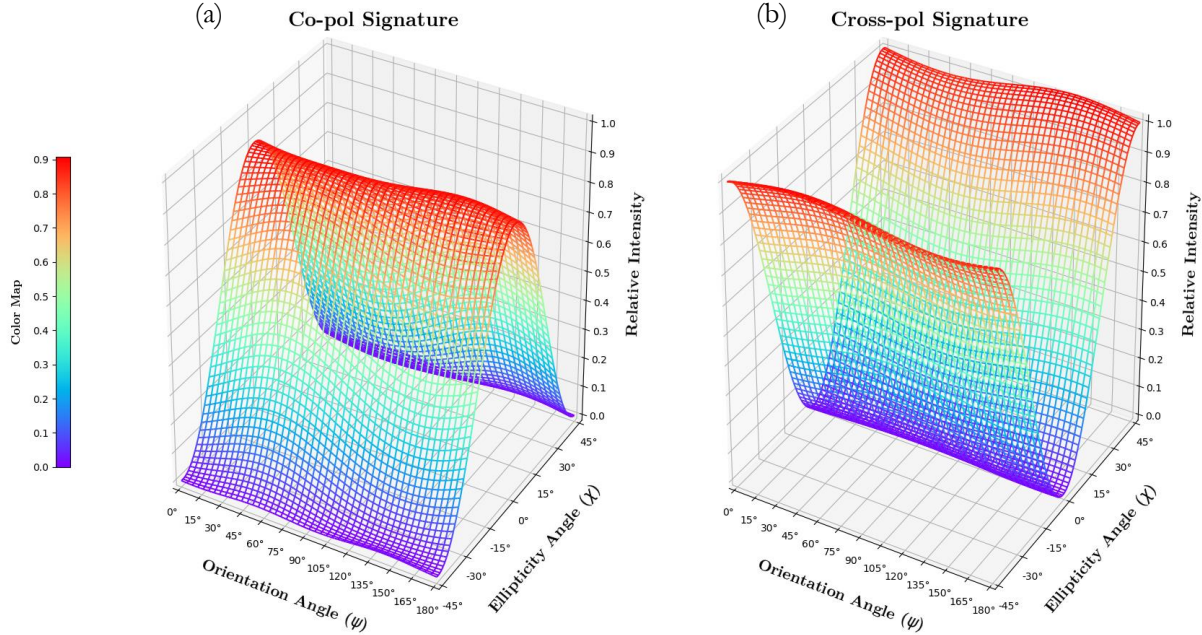
Figure 12: Polarimetric signatures of corner reflector 21. It is a triangular trihedral corner reflector with 2.4 m side length, (a) co-pol signature, (b) cross-pol signature

The polarimetric signatures of the 2.4 m corner reflector in Figure 12 and polarimetric signatures of 4.8 m corner reflector in Figure 11 closely depict the ideal shape of the triangular trihedral corner reflector. Although there are some visible distortions in the cross-pol signatures of both the corner reflectors, the distortions are not high, i.e. phase offset is reasonable. Therefore, the dataset is radiometrically calibrated and the presence of phase imbalance is negligible.

5.2.   Estimations using Quegan's Algorithm

Estimates of Crosstalk Parameters

The variations of crosstalk parameters estimated using Quegan's algorithm have been observed before and after the crosstalk calibration. In Figure 13, crosstalk parameters are plotted for the range direction over 2750 range pixels. It can be observed that the parameter u varies roughly between -28 dB to -34 dB before the calibration and it varies roughly between -34 dB to -38 dB after the calibration. There are no anomalies in the estimation of u as the residual of u is less than the estimated u before the calibration in all the cases. The parameter v is estimated to be nearly -20 dB and it does not show much variations with respect to the range direction before the calibration. However, residual of v varies between -35 dB and -43 dB and exhibits a similar pattern to that of residual u. The parameter w mostly varies around -35 dB before the calibration and it is estimated to be roughly between -35 dB -42 dB after the calibration. The parameter z is estimated to be in the range of -34 dB to -36 dB before calibration and in the range of -35 dB to -39 dB after the calibration.
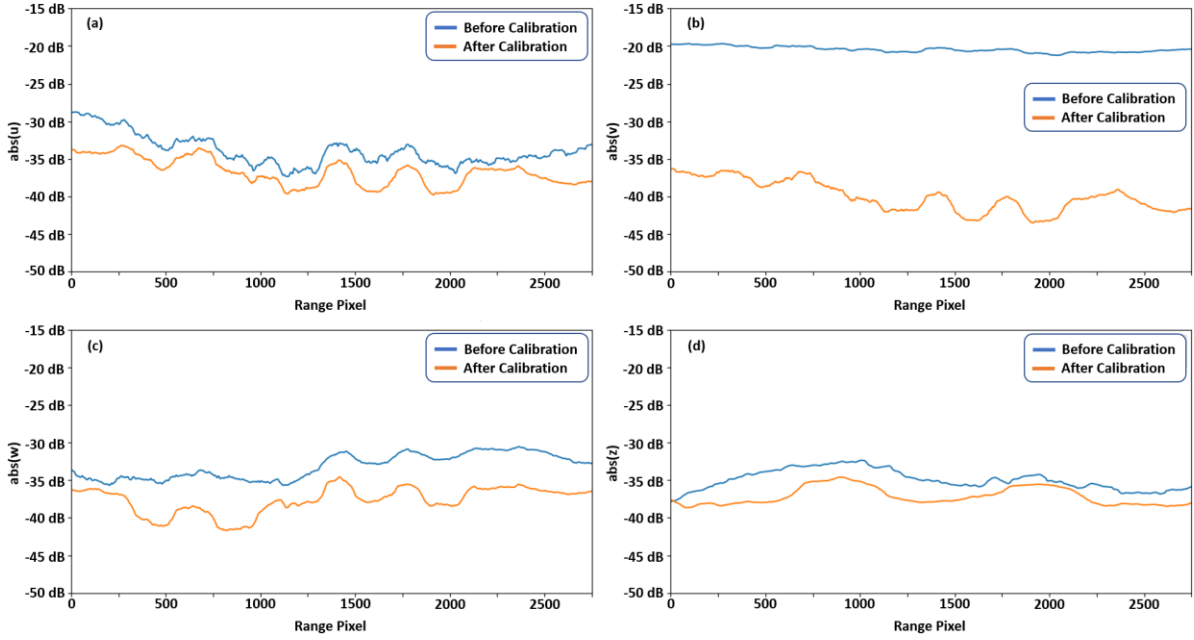
Figure 13: Variation of Quegan's crosstalk parameters with respect to range. All the crosstalk parameters have reduced after performing calibration.

Estimate of Channel Imbalance

Similar to the crosstalk parameters, the estimated channel imbalance parameter α is plotted against the range direction in Figure 14, both before and after the calibration. The amplitude of α varied between 0.25 dB to 0.35 dB before the calibration which reduced to below 0.07 dB after the calibration. On the other hand, the phase of α varied close to 27° before the calibration and it reduced to nearly 0° after performing the calibration. The residual amplitude and phase of α indicate that the channel imbalance has been substantially reduced.
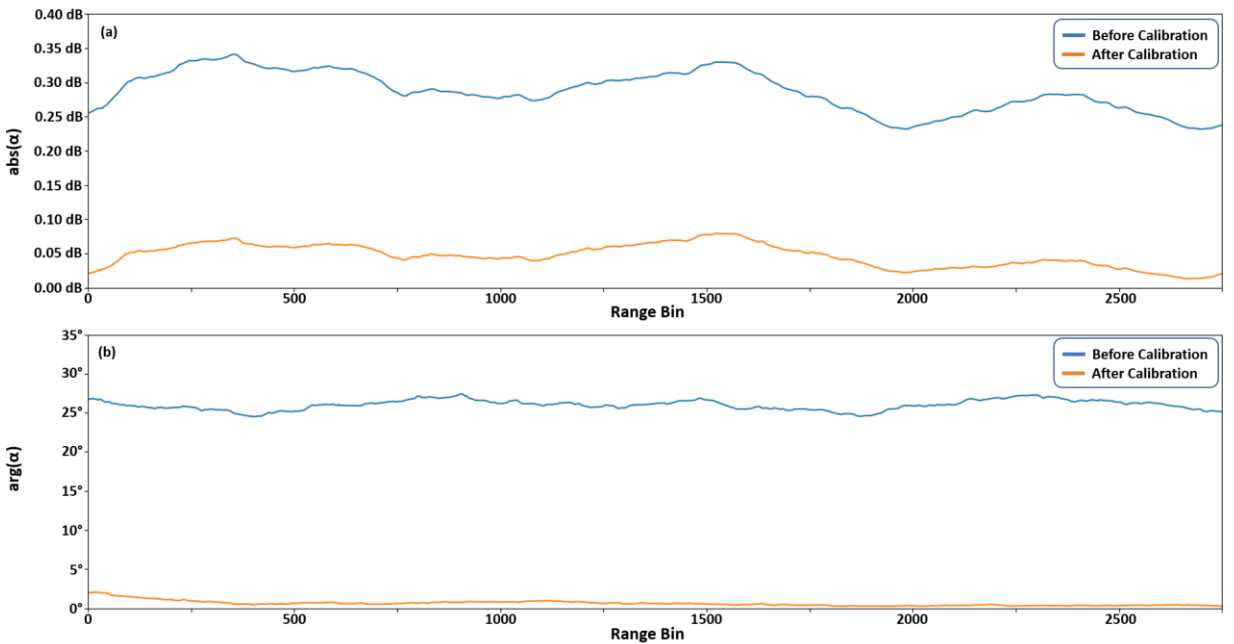

Figure 14: Variation of estimated using Quegan's algorithm, (a) shows the variation of amplitude of α with respect to the range direction, (b) shows the variation of phase of α with respect to the range direction

Polarimetric Signatures

The polarimetric signature of the corner reflector 24 after performing the crosstalk and channel imbalance calibration is shown in Figure 15.
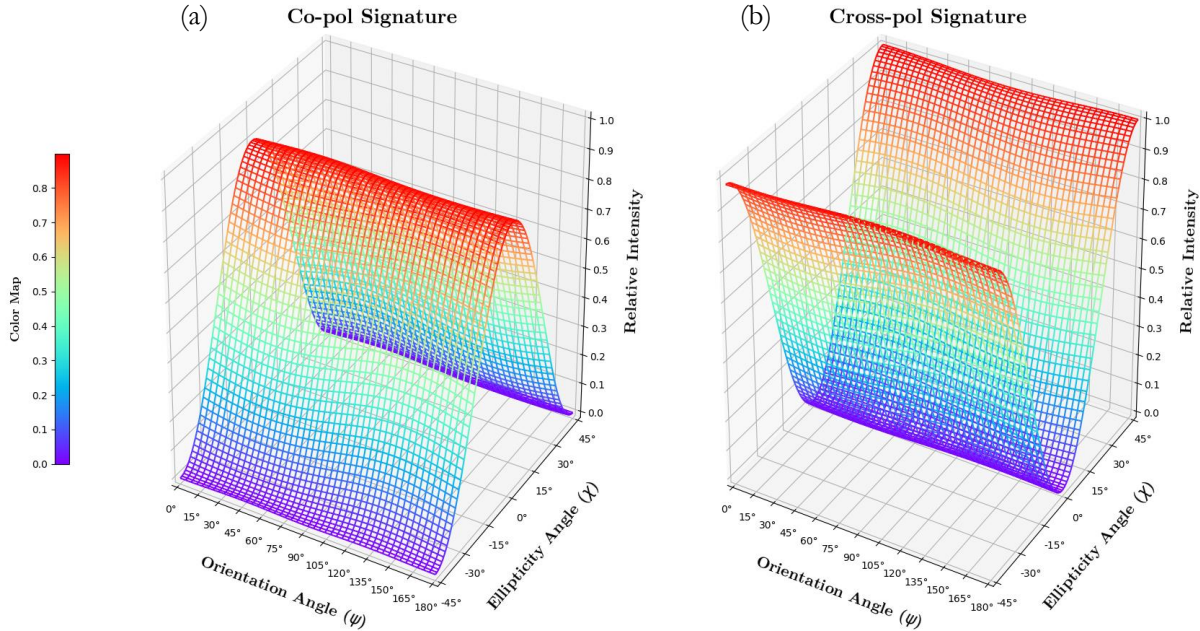

Figure 15: Polarimetric signatures of corner reflector 24 after crosstalk and channel imbalance calibration using Quegan's algorithm. (a) co-pol signature, (b) cross-pol signature

The distortions present in Figure 11 have been reduced significantly. Similarly, the signature of all the corner reflectors with distortions before the crosstalk and channel imbalance calibration have been improved after performing the calibration.

Estimates of Data Quality

MNE Estimate

Wang et al., (2011) recommended that the MNE is a suitable metric to evaluate the polarimetric distortions. Figure 16 shows the variation of MNE before performing the crosstalk calibration. The MNE before performing the crosstalk varied between -18.41 dB and -21.63 dB. However, MNE has been reduced to the range of -26.69 dB to -33.81 dB after crosstalk calibration using Quegan's algorithm as shown in Figure 17. It is observed from Figure 17 that a large number of range pixels do not satisfy the threshold of -30 dB.
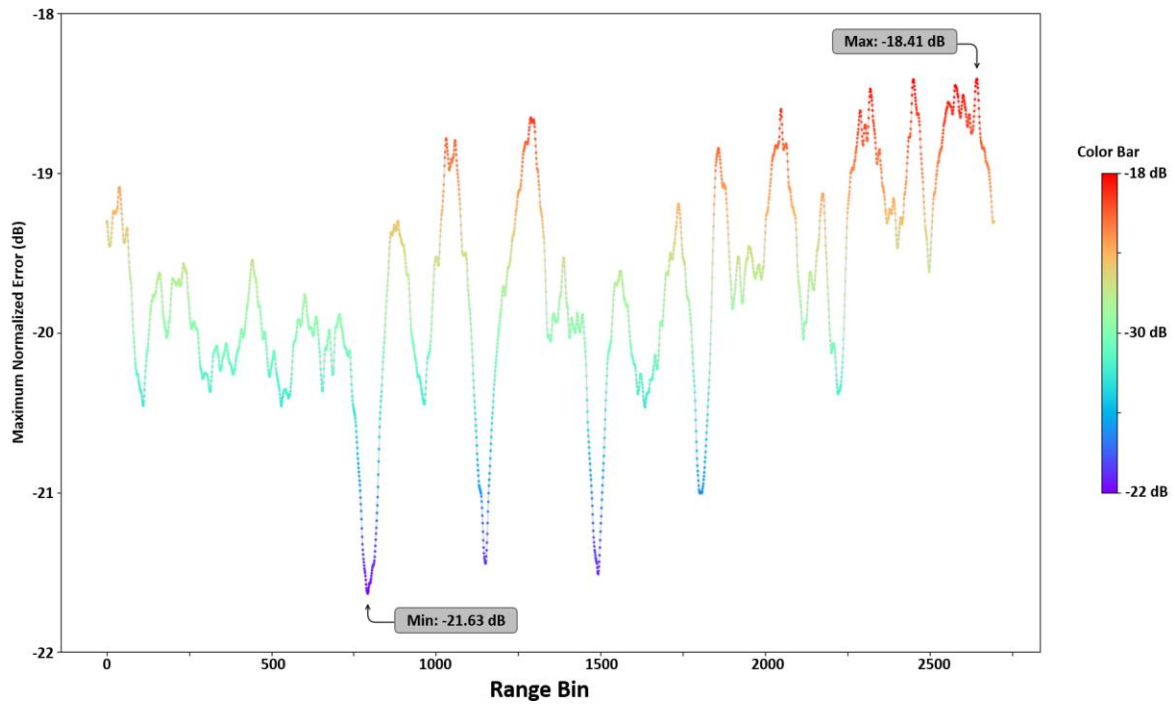
Figure 16: Variation of MNE with respect to the range direction before calibration
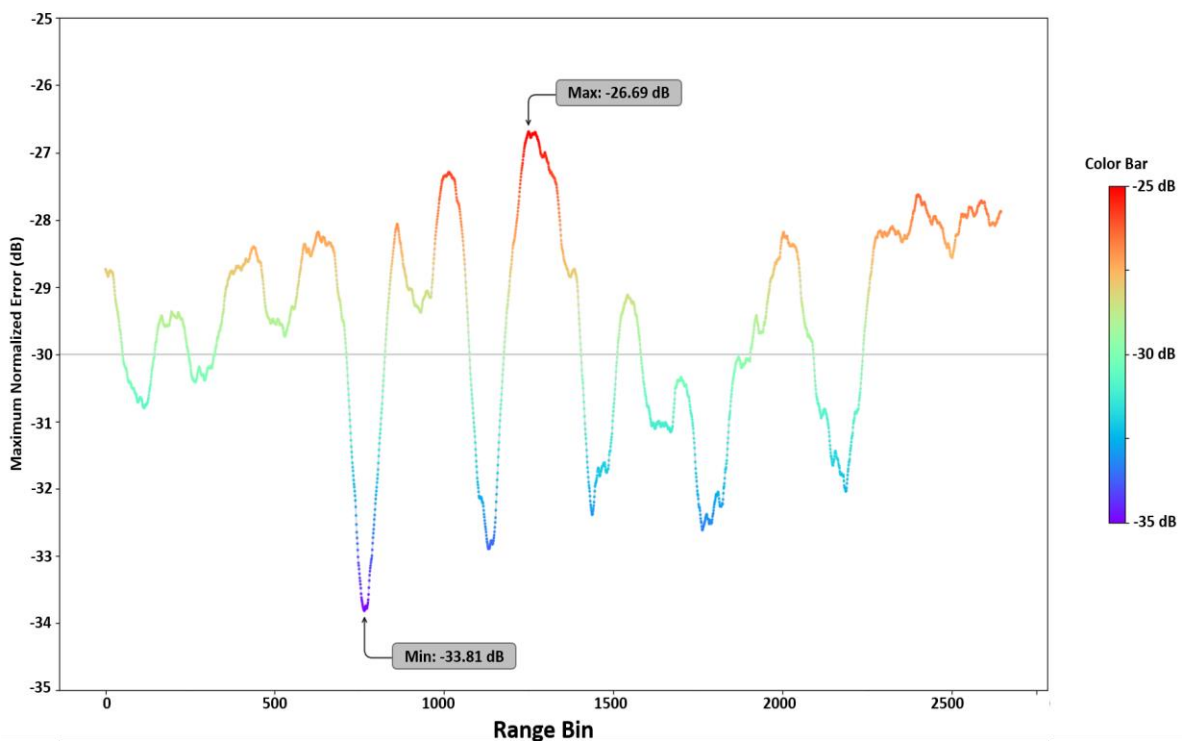

Figure 17: Variation of MNE with respect to the range direction after Quegan's calibration

SNR Estimate

Similar to the MNE, the cross-pol SNR has been estimated before and after performing the crosstalk calibration which is shown in Figure 18.
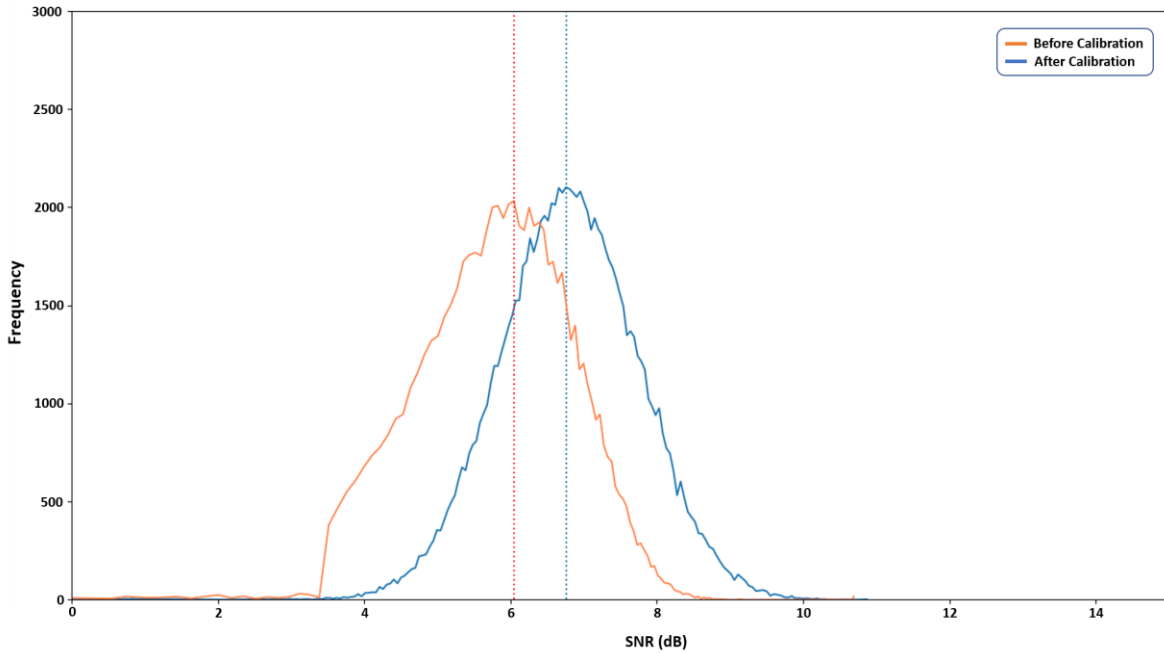

Figure 18: Histogram of cross-pol SNR before and after Quegan's crosstalk calibration. The median of the cross-pol SNR has been shifted to higher value after calibration.

In both cases, the histograms resemble a normal distribution. The mode of the histogram improved to 6.89 dB after the calibration from 6.12 dB before the calibration. However, the distribution of SNR is more uniform after the calibration compared to the distribution of the SNR before.

Effect on Roll Invariant Parameters

The study area for this research mostly comprises of a relatively smooth flat surface. Therefore, surface scattering is expected to be dominating. The volume scattering from vegetation might be present due to the presence of light vegetation near the edge of the dry lake bed. However, the volume scattering should be comparatively low. The H-α planes before and after the calibration are presented in Figure 19.

Figure 19(a) shows that most of the pixels lie in the region of surface scattering with low and medium entropy. However, a relatively large number of pixels depicts medium entropy scattering rather than low entropy surface scattering. Furthermore, the pixel densities indicate that there is a significant amount of volume scattering present despite being lesser than the surface scattering. Presence of double bounce scattering, multiple scattering and anisotropic scattering is negligible.

In contrast, the surface scattering in Figure 19(b) has significantly increased after performing the calibration using the Quegan's algorithm. The amount of volume scattering has been reduced but still significantly present. However, the amount of double bounce scattering has increased which might be attributed to the rocky patches at near the edge of the lake bed. Additionally, the anisotropic scattering slightly increased which is unexpected as no anisotropic medium is known to be present in the study area.
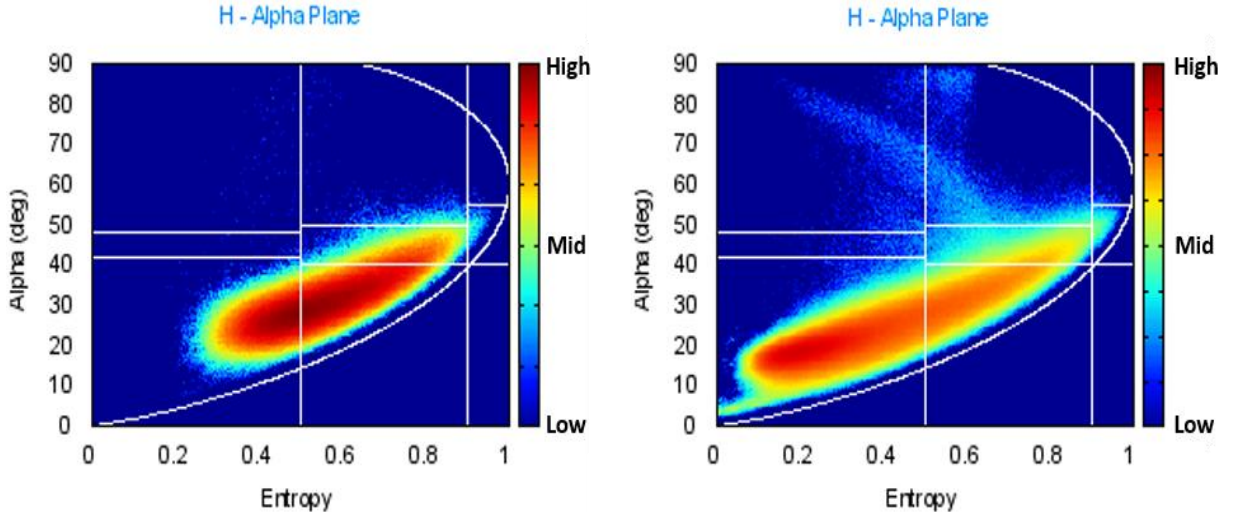
Figure 19: H-α Plane, (a) Before Crosstalk Calibration, (b) After calibration using Quegan's algorithm. Overall surface scattering has increased after calibration

5.3.   Estimations using Improved Quegan's Algorithm

The cross-polarisation noise ratio has been estimated from a relatively homogeneous patch of 734×647 pixels, and it is found to be very close (precision of 10⁻⁴) to the ideal value of one. Due to this reason the crosstalk parameters and channel imbalance parameters estimated to be the nearly equal to the estimations of Quegan's algorithm. The implication of this can be further observed in the estimated cross-pol SNR.

Estimate of Data Quality

The median of SNR slightly increased to 7.03 dB compared to Quegan's 6.89 dB as shown in Figure 20. The estimated MNE also follows a similar trend to that of Quegan's MNE. It can be interpreted from Figure 21 that, the change in the range of MNE is not significant. Similar to Quegan's algorithm, most pixels do not satisfy the requirements of having MNE less than -30 dB. However, near the range pixel of
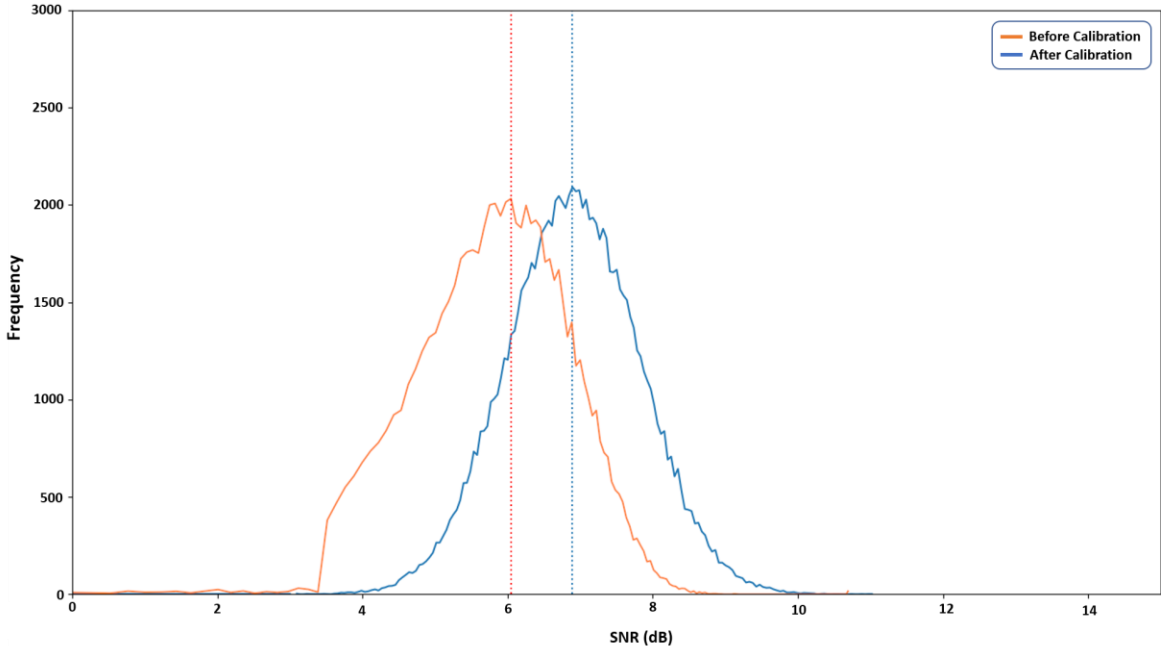
Figure 20: Histogram of cross-pol SNR before and after improved Quegan's crosstalk calibration. The median of the cross-pol SNR has been shifted to higher value after calibration.

800, 1200, 1500, 1750 and 2200 the MNE is as lower than -32 dB and in some cases, it is as low as -34 dB. In brief, the MNE shows a highly irregular and unstable pattern to the range direction.
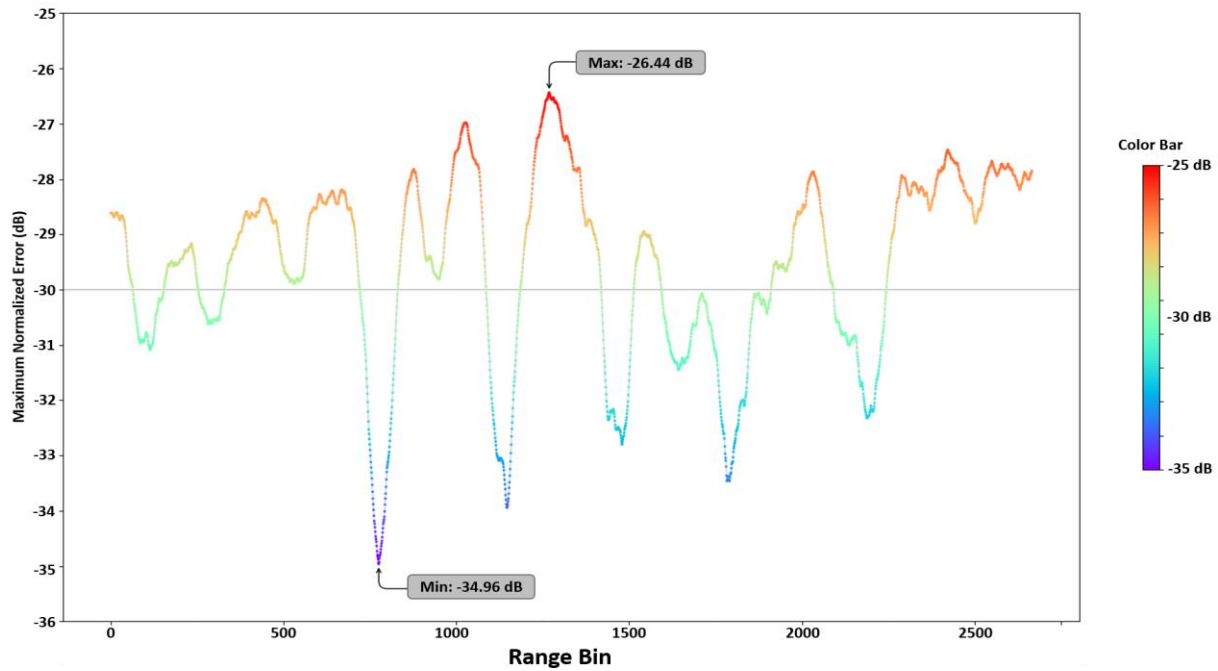
Figure 21: Variation of MNE with respect to the range direction after improved Quegan's calibration

5.4.   Estimations using Ainsworth Algorithm

Estimates of Crosstalk Parameters

The variation of crosstalk parameters in rage direction before and after the crosstalk calibration is shown in Figure 22. Evidently, before calibration, in some cases, the crosstalk parameters are higher than standard -35 dB threshold.
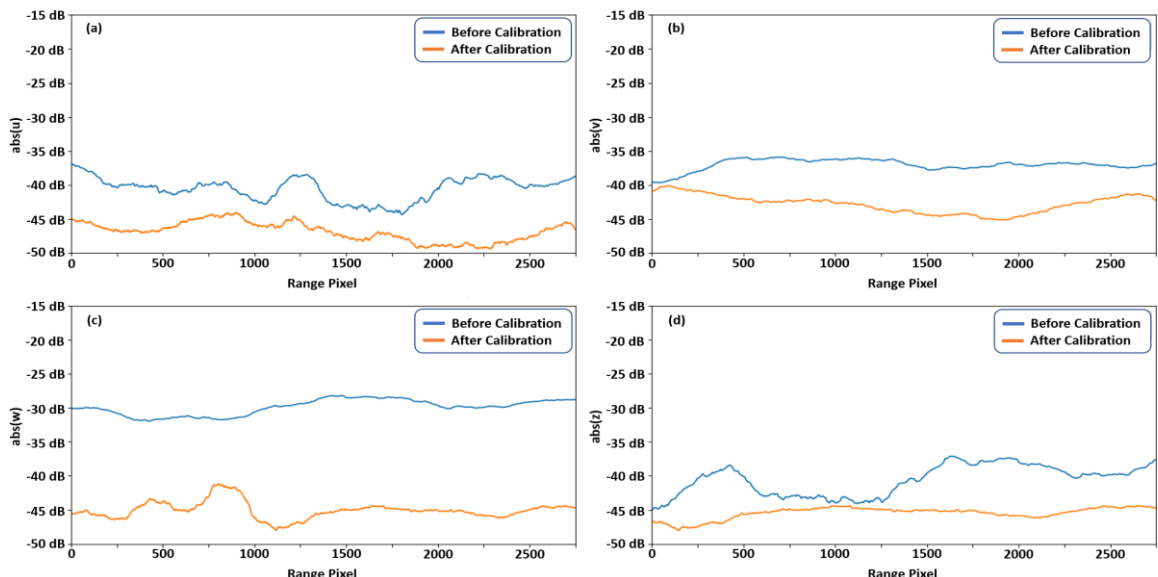
Figure 22: Variation of crosstalk parameters estimated using Ainsworth algorithm. All the crosstalk parameters have reduced after performing calibration.

However, all the crosstalk parameters have reduced below -40 dB after the crosstalk calibration using Ainsworth algorithm. The parameters u, w and z are varied mostly below -45 dB; however, the parameter gently varied between -40 dB to -45 dB. Furthermore, comparing Figure 13 and Figure 22, it can be observed that the estimation of crosstalk parameters using Ainsworth algorithm are relatively stable with respect to Quegan's algorithm.

Estimate of Channel Imbalance

The channel imbalance before and after performing Ainsworth crosstalk calibration is plotted with respect to range in Figure 23. The amplitude of α varied above 0.2 dB before the calibration which reduced below 0.05 dB after the calibration. The phase of α was stable around 26° before the calibration and it reduced below 2° after performing the calibration. Unlike crosstalk parameters, the estimated value of α before the calibration shows the similar variation in the range direction to that of Quegan's estimation. The amplitude of α is lower after the calibration using the Ainsworth algorithm compared to the amplitude of α after performing calibration using Quegan's algorithm. However, the phase of α is more stable and lies closer to 0° in the case of Quegan's algorithm.
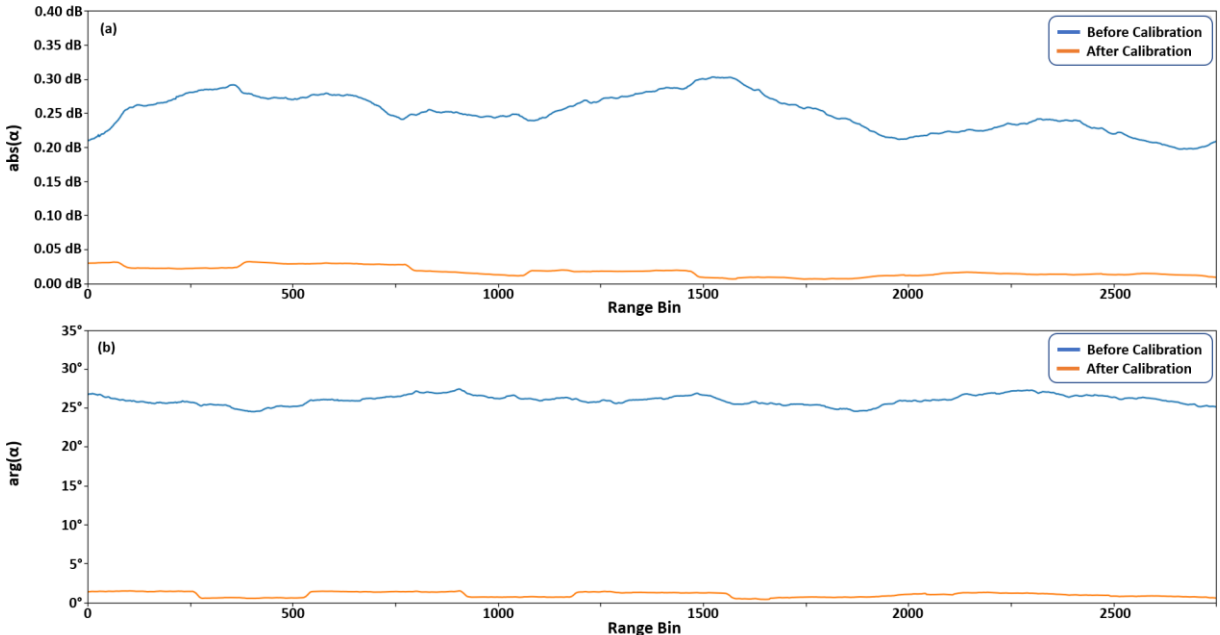
Figure 23: Variation of α estimated using Ainsworth algorithm, (a) shows the variation of amplitude of α with respect to the range direction, (b) shows the variation of phase of α with respect to the range direction

Polarimetric Signature

The polarimetric signatures after the crosstalk and channel imbalance calibration have been shown in Figure 24. It can be observed that the distortions both co-pol and cross-pol signatures have been reduced. After performing the calibration, similar improvements have been observed in the signatures of other corner reflectors containing some distortions.
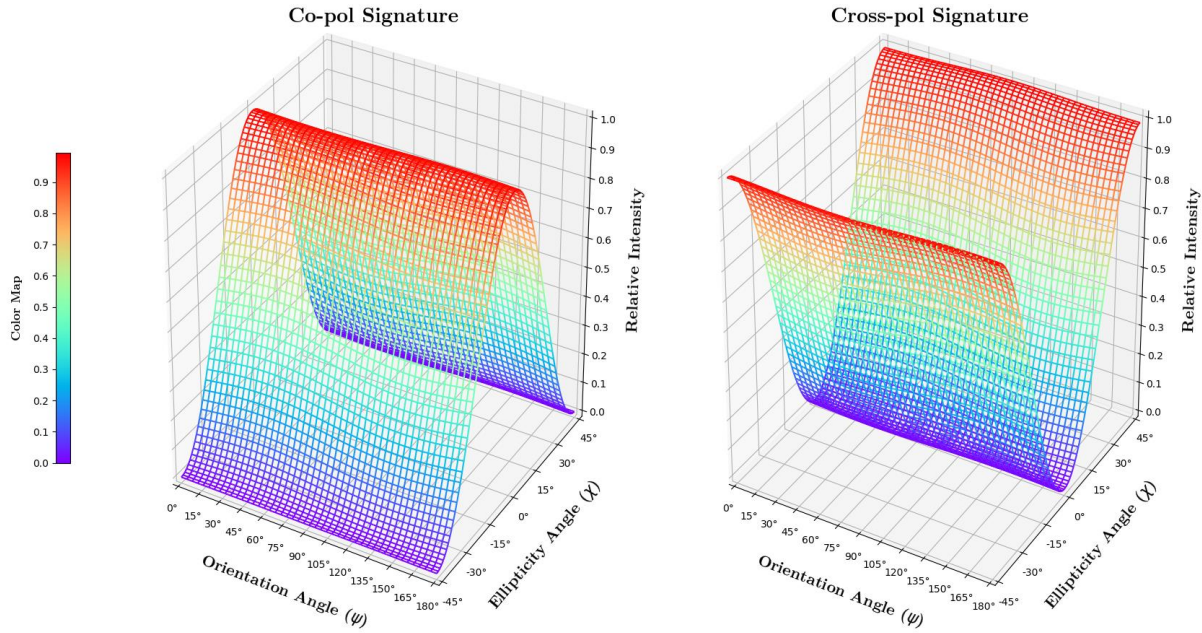
Figure 24: Polarimetric signatures of corner reflector 24 after Ainsworth calibration (a) co-pol, (b) cross-pol signature. The distortion in the shapes have been reduced.

Estimate of Data Quality

MNE Estimate

The variation of MNE in range direction estimated after the crosstalk calibration is shown in Figure 25. The MNE highly varied between -32 dB to -42 dB and reaches maxima near range pixel 1900. Except for the close neighbourhood of the maxima, MNE is below -35 dB in the rest of the range bins.
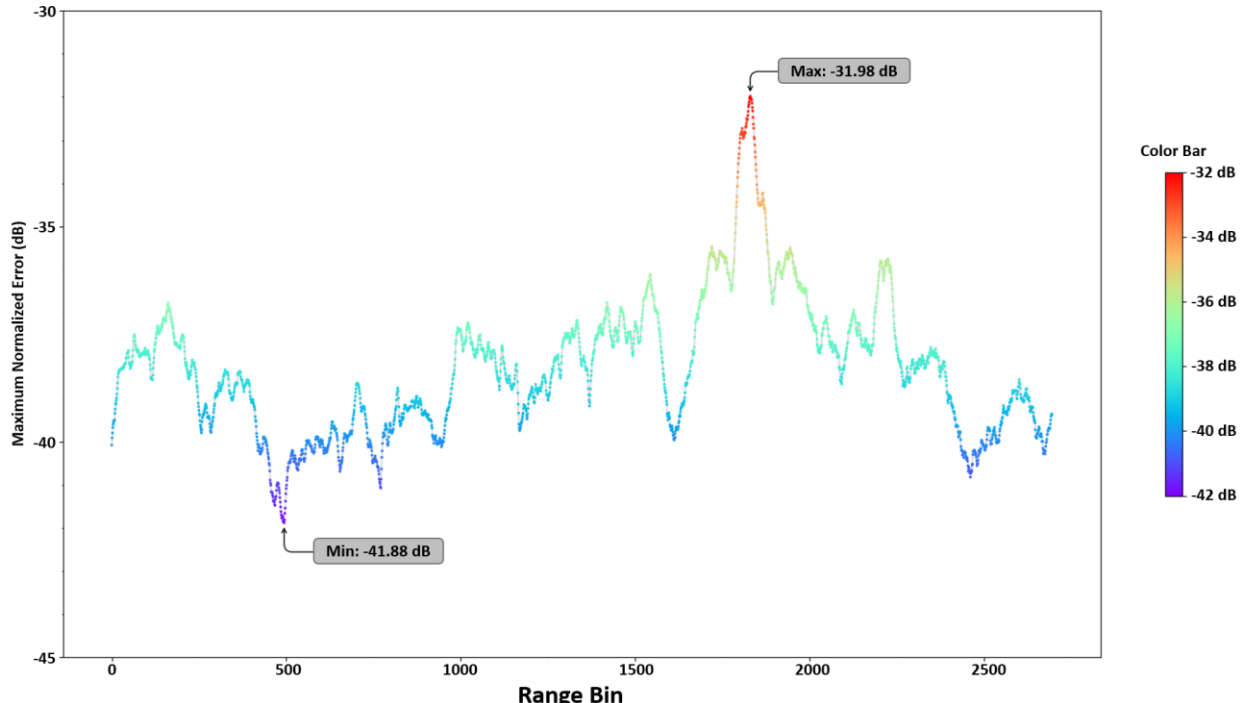
Figure 25: Variation of MNE with respect to the range direction before improved crosstalk calibration using Ainsworth algorithm

SNR Estimate

The histogram of the cross-pol SNR is shown in Figure 26. The histogram of the cross-pol SNR closely follows the normal distribution. After the calibration, the median has increased to more than 8 dB from 6 dB before the calibration.
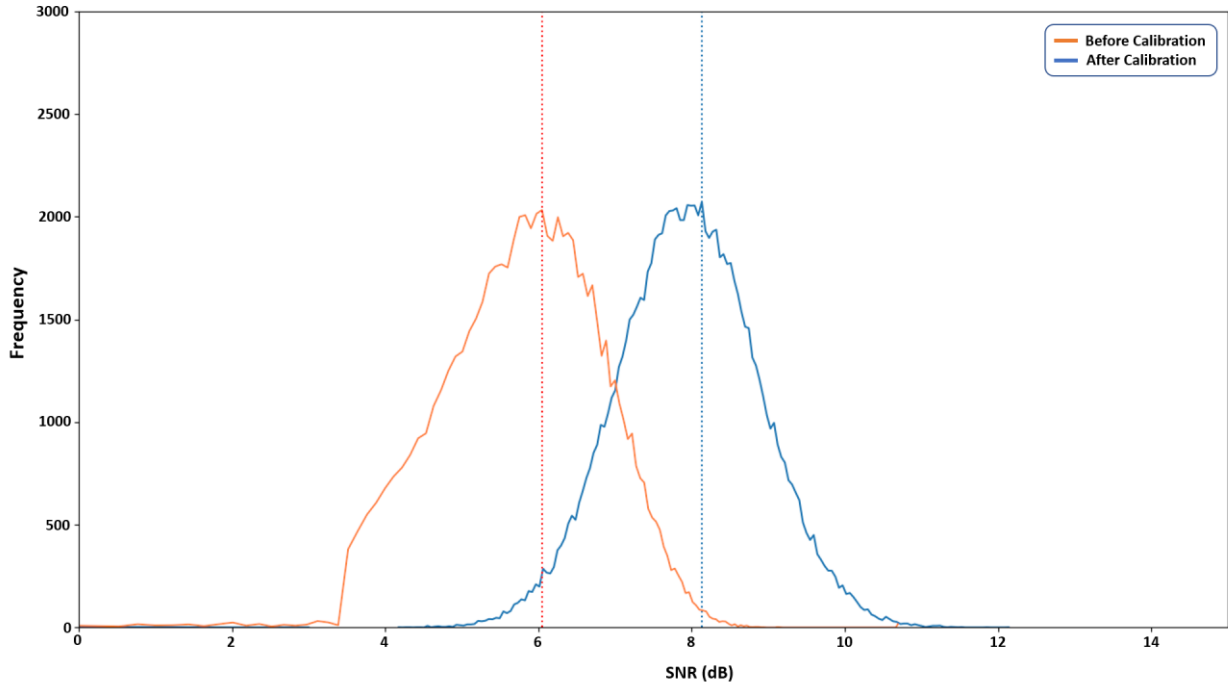
Figure 26: Histogram of cross-pol SNR before and after Ainsworth crosstalk calibration

Effect on Roll Invariant Parameters

The H-α plane after performing the calibration using the Ainsworth algorithm has been shown in contrast with the scenario before the calibration in Figure 27.
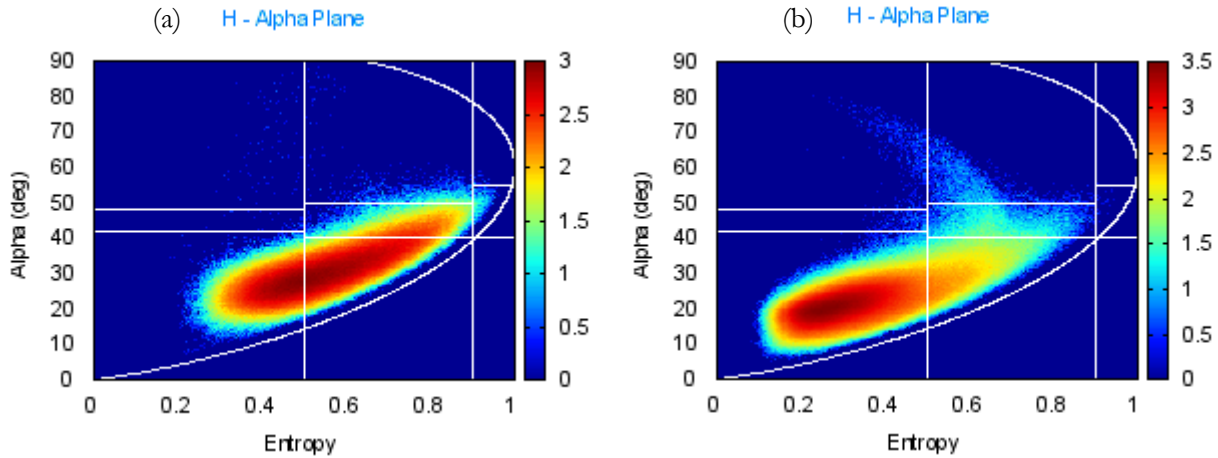
Figure 27: H-α Plane, (a) Before Crosstalk Calibration, (b) After calibration using Ainsworth algorithm

From Figure 27(b) it can be observed that the surface scattering is the most dominant scattering having the maximum contribution from the low entropy surface scattering. Consequently, the medium entropy surface scattering and has been significantly reduced. The multiple scattering is higher than the scenario before the calibration which might be related to the rocky patches as discussed earlier. However, the double bounce scattering in case of Ainsworth calibration is comparatively lower than that of Quegan's calibration. Interestingly, the anisotropic scattering, in this case, is nearly non-existent which correctly depicts the characteristics of the surface. The quality of calibration by Ainsworth algorithm is better than that of Quegan's algorithm.

5.5.   Estimations using Proposed Algorithm

The proposed algorithm adopts a hybrid approach using both Quegan's algorithm and Ainsworth algorithm to improve the computational efficiency while maintaining the quality of calibration similar to the Ainsworth algorithm. Hence the performance of this algorithm has been evaluated through the following results.

Estimates of Data Quality

The MNE after the calibration using this method follows a similar pattern to that of Ainsworth algorithm as it can be observed in Figure 28. However, some minor differences can be observed approximately in the range of -36 dB to -39 dB which might be attributed to the cases where the solutions provided by Quegan's algorithm is acceptable. However, the trend is similar to the Ainsworth algorithm in the rest of cases as the algorithm falls back to Ainsworth algorithm in case Quegan's estimate is not adequate.
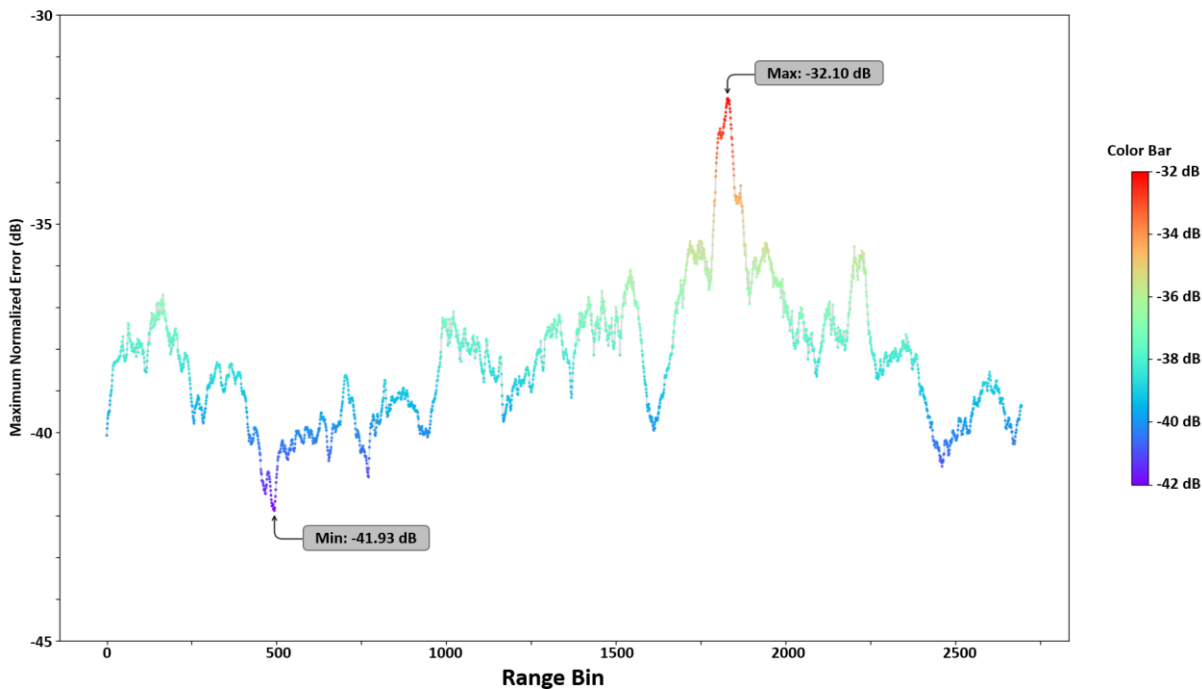

Figure 28: Variation of MNE with respect to the range direction before and after improved crosstalk calibration using proposed algorithm

Similar to the MNE, the cross-pol SNR in Figure 29 does not differ significantly from the cross-pol SNR estimates of the data calibrated using the Ainsworth algorithm. Interestingly, the median of the SNR, in this case, has decreased by 0.003 dB from the Ainsworth algorithm. This minute reduction in cross-pol SNR might be attributed to the cases where Quegan's solution has been accepted.
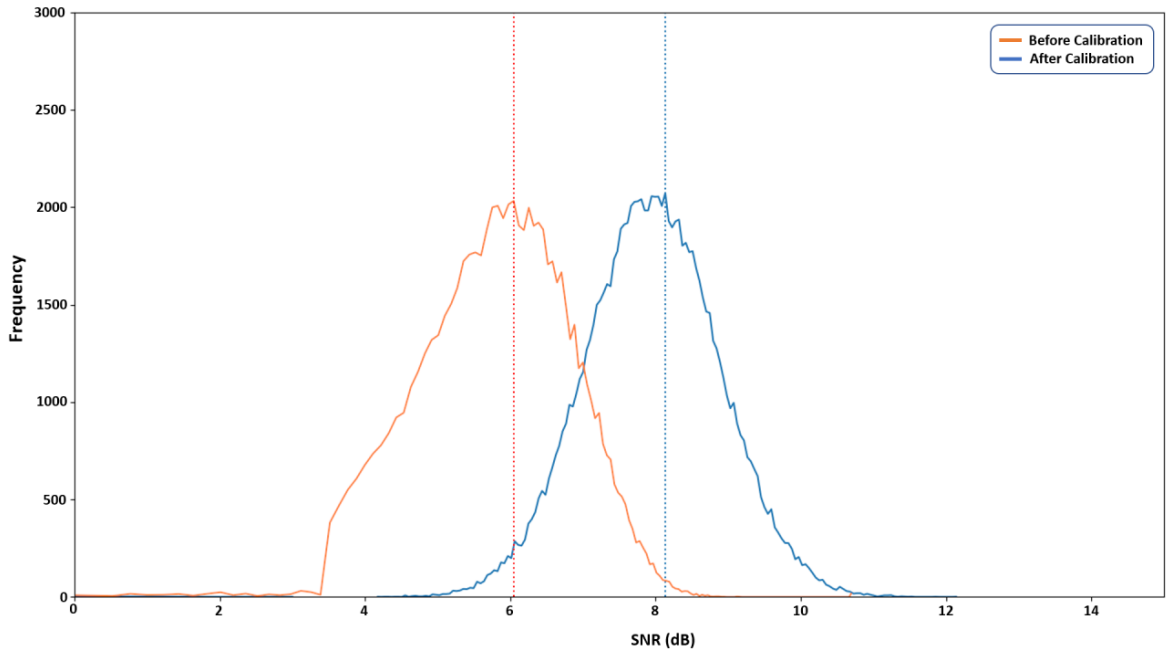
Figure 29: Histogram of cross-pol SNR before and after the crosstalk calibration using the proposed algorithm

Performance Evaluation

The intended objective of the proposed algorithm is to reduce high computational cost caused by the iterative construct of the Ainsworth algorithm without harming the accuracy. Therefore, the computational costs of the proposed algorithm have been monitored in terms of the iterations computed for each pixel. The frequency of iterations observed for 1 million pixels (1000×1000 subset image) has been shown in Figure 30. The iteration 6 has the highest frequency, i.e. in most cases, Ainsworth algorithm inside the proposed algorithm converges with six iterations. The frequencies of iterations steadily decrease after 6. The frequency of the maximum iteration 16 is not zero. It indicates that there might be a few instances where the algorithm did not converge up to the expected precision. The frequencies of the initial few iterations are comparatively low since the Ainsworth algorithm initialises with the crosstalk parameters set to zero, i.e. it is assumed that crosstalk is not present in the dataset. Consequently, the algorithm requires a few iterations before it converges.

Here, iteration 0 depicts the cases where the algorithm directly accepted the Quegan's solutions. Evidently, in case of 135.57×10^3 pixels out of 10^6 pixels, the algorithm found the solution of Quegan's estimations to be suitable. Therefore, the iterative computations have been avoided for nearly 13.6% cases.

5.6.   Comparison of Algorithms Regarding Entropy and Scattering Angle

The entropy (H) and scattering angle (α) from the H-α decomposition have been observed at the corner reflector points before and after the calibration as these parameters are influenced by the presence of crosstalk. Theoretically, the triangular trihedral corner reflectors depict odd bounce scattering, therefore the value of entropy and scattering angle ideally should be very low in the corner reflector points. However, these two parameters potentially increase in the presence of crosstalk. Consequently, calibration should rectify these anomalies by reducing crosstalk.
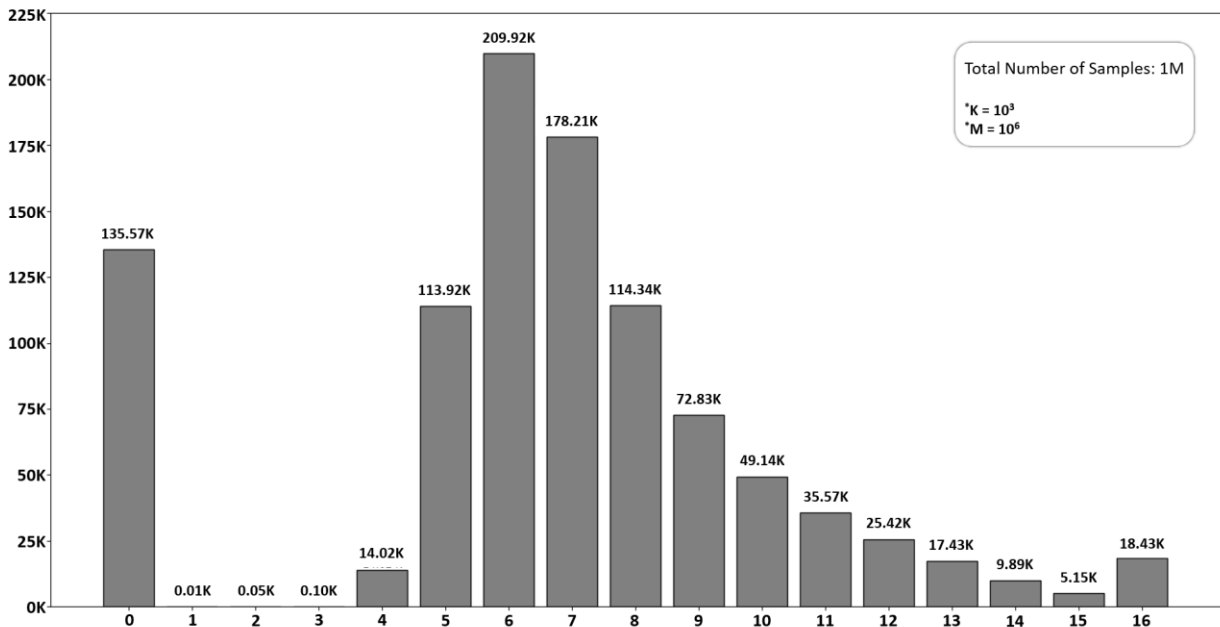
Figure 30: Computational costs of the proposed algorithm observed for 10^6 pixels. Frequencies of each iteration has been shown on the top of each bar.

The changes observed in the value of H and before and after crosstalk calibration for all algorithms are shown in Figure 31. It can be observed that both the entropy and scattering angle has consistently decreased after each method. The Ainsworth algorithm performs better in terms of reducing these parameters. Expectedly, Quegan's algorithm and Ainsworth algorithm performs nearly the same as the cross-channel noise imbalance is negligible as per the observations. Similarly, Ainsworth algorithm and the proposed algorithm performs equally well.

5.7.   Effect of POA Shift Compensation

In general, the presence of POA shift causes overestimation of volume scattering and underestimation of even bounce scattering. POA shift correction has been performed after the crosstalk calibration by both Quegan's algorithm and Ainsworth algorithm. In Figure 32, the scattering patterns of a patch calibrated using the Quegan's algorithm have been shown before and after performing the POA shift compensation.

It can be observed that in the encircled areas volume scattering has decreased which indicates the changes regarding the POA shift correction. However, these changes are relatively small, which is justifiable as the topographic variations in the study area are negligible. Similar behaviour can be observed in Figure 31 in the case of POA shift correction after the calibration using the Ainsworth algorithm. In Figure 31(a), the presence of significant volume scattering can be observed which has been further reduced in Figure 31(b) as a result of the POA shift compensation. However, in both cases, the changes in the double bounce scattering due to POA shift has not been observed since the calibrated scenes hardly show any double-bounce scattering.

Table 3 shows the decrease in the volume scattering in terms of mean and standard deviation of the volume scattering estimated using the Y4R decomposition. In both the cases, the mean of the volume scattering has been reduced after POA shift correction. Although the standard deviation of volume scattering has stayed the same after POA shift correction of Q, the same has been reduced after POA shift compensation in case of A.

Table 3: Change in the volume scattering before and after the POA shift for Quegan and Ainsworth algorithm

	Quegan (Q)		Ainsworth (A)	
	Mean	Std. Dev.	Mean	Std. Dev.
Before POA Shift	3.31×10^{-4}	2.87×10^{-4}	3.31×10^{-4}	3.06×10^{-4}
After POA Shift	2.91×10^{-4}	2.88×10^{-4}	2.88×10^{-4}	2.73×10^{-4}
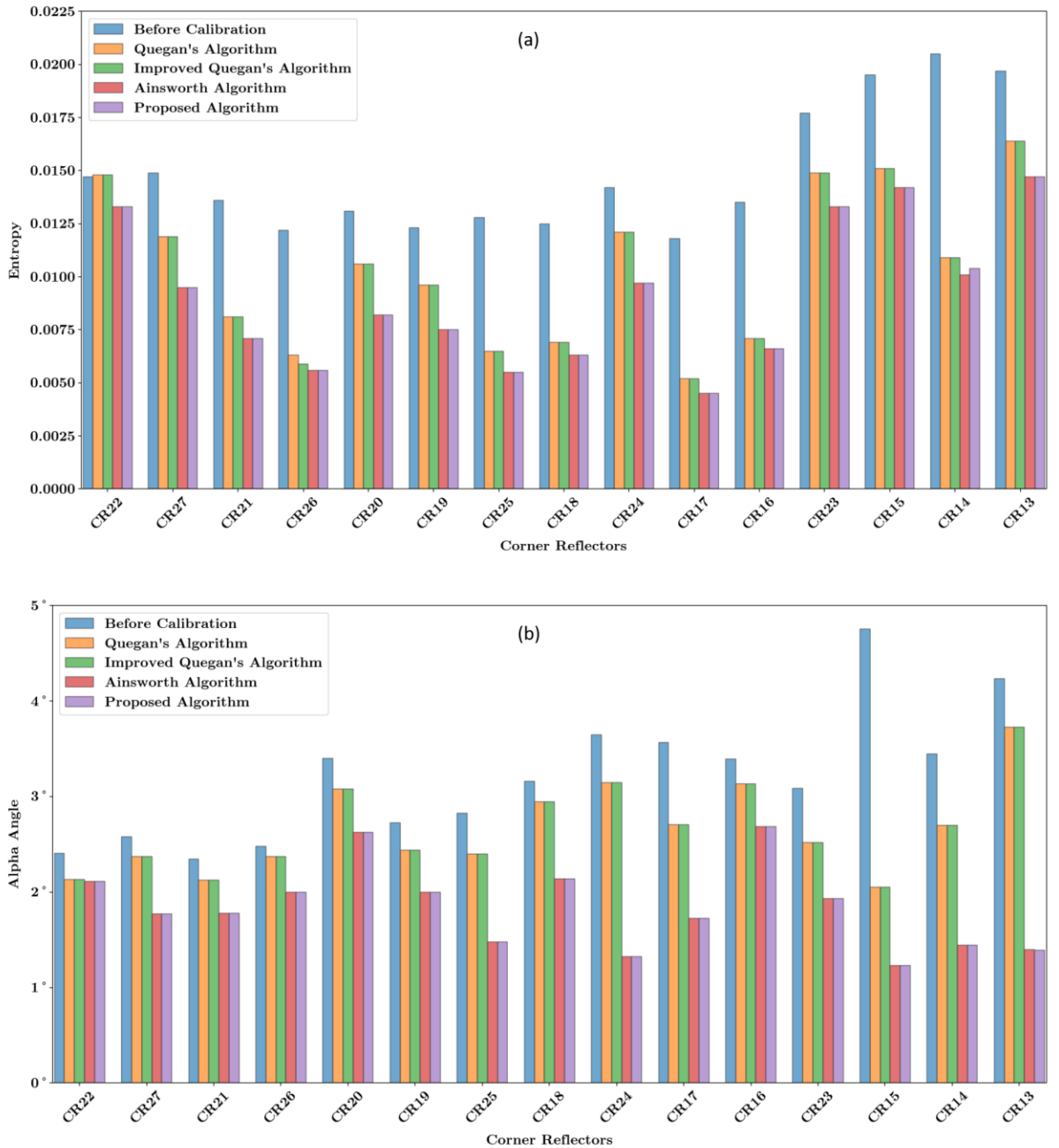
Figure 31: Effect of crosstalk calibration using different algorithms on (a) entropy and (b) scattering angle. Both scattering angle and alpha have reduced due to calibration.
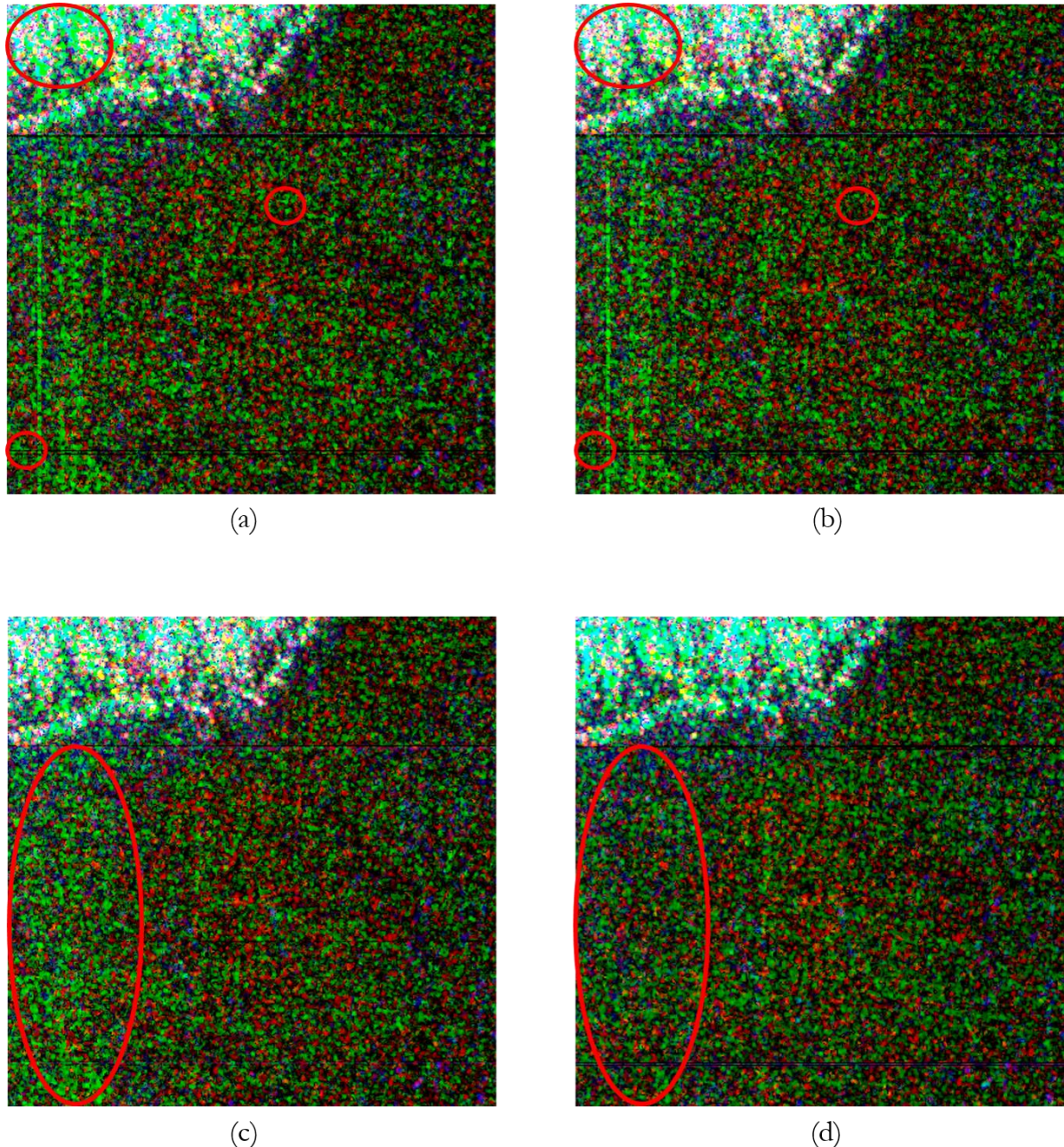
Figure 32: The scattering patterns in Y4R RGB composite of a small patch. (a) scattering pattern after applying Quegan's algorithm, (b) scattering pattern after applying POA shift correction on the patch calibrated using Quegan's algorithm, (c) scattering pattern after applying Ainsworth algorithm, (d) scattering pattern after applying POA shift correction on the patch calibrated using Ainsworth algorithm. Here, Red signifies double bounce scattering, Green signifies volume scattering and blue signifies surface scattering. The respective encircled areas in red are highlighting the changes in the scattering pattern

5.8.   Chapter Summary

In this chapter, the results of the methods are discussed in chapter 3 for the dataset specified in chapter 4. However, the radiometric and phase calibrations have not been performed as the dataset is already radiometrically and phase calibrated. Furthermore, the implications of the results regarding the objectives of this study have been briefly discussed below.

Specific Objective - I

The dataset has been calibrated for the minimisation of crosstalk and channel imbalance using different algorithms. In the case of both Quegan's and Ainsworth algorithms, it can be observed that residual crosstalk has been significantly decreased after the calibration. Furthermore, the reduction of distortions in the polarimetric signature indicates that the channel imbalance has been adequately minimised.

Specific Objective - II

Expectedly, the presence of POA shift is not prominent in the study area since topographic variations are not significant. However, the minute presence of POA shift has been observed through decomposition modelling. In some regions, it has been observed that the potentially overestimated volume scattering has been reduced.

Specific Objective – III

The calibration process reduces the noise present in the data which can be verified as the MNE decreases significantly after the calibration. Moreover, the increase in the cross-pol SNR after calibration strongly signifies the improvement in the data quality. Furthermore, calibration helps to reveal the correct scattering pattern of the targets as conveyed by changes in the H-α plane before and after the calibration.

6.   DISCUSSION

In this section further discussion has been provided regarding the implications of the results obtained in chapter 5. Moreover, it focuses on finding out the answers to the research question from these results.

Research Question – I
Comparing the results in section 5.2 and section 5.4, it is evident that the Ainsworth algorithm is better in terms of minimising crosstalk than the Quegan's algorithm since the residual crosstalk of Ainsworth algorithm is significantly lower than the residuals of Quegan's algorithm. In some cases, Quegan's algorithm fails to comply with the CEOS cal-val recommendation of maintaining the residual crosstalk below -35 dB (ESA, 2004). In this regard, Ainsworth algorithm performs well by reducing the residual crosstalk parameters below -40 dB.

Looking at the polarimetric signatures after the calibrations, it cannot be implied that one algorithm is better at minimising channel imbalance than the other algorithm, the performance of both the algorithms seems nearly equal. Variations of channel imbalance, however, show that the Ainsworth algorithm is slightly better at minimising the amplitude of the channel imbalance than the Quegan's algorithm. On the contrary, Quegan's algorithm appears to perform better at reducing the phase of the channel imbalance. It can be observed in the plots showing the variations of the phase of the channel imbalance that the estimates by Quegan's algorithm are relatively stable and stays close to the ideal zero value compared to the estimates by Ainsworth algorithm. However, this difference is negligible.

The accuracies of these algorithms can be better compared in terms of MNE and cross-pol SNR as these metrics adequately represent the actual data quality. According to Wang et al., (2011), -20 dB of MNE translates into -26 dB of crosstalk and the recommended value of MNE is -25 dB. On the contrary, the recommended threshold for the crosstalk is -35 dB (ESA, 2004). Therefore, the threshold for MNE has been set to -30 dB for this study. After performing the calibrations, it is evident from the plots of MNE that the MNE of the data calibrated using Ainsworth algorithm is significantly lower than the MNE of the data calibrated using Quegan's algorithm. Since MNE is a metric of noise, it can be deduced that the Ainsworth algorithm is better at minimising the noise present in the data than the Quegan's algorithm. On the contrary, cross-pol SNR provides information regarding the useful information content relative to the noise present in the data; in brief, it signifies the quality of the data. The estimated cross-pol SNR after the calibration using the Ainsworth algorithm is higher than the cross-pol SNR estimated after the calibration using Quegan's algorithm. Therefore, concerning the accuracy, Ainsworth algorithm is better in terms both the data quality metrics compared to the Quegan's algorithm.

Research Question – II
In contrast with the Quegan's algorithm, the improved Quegan's algorithm considers the possibility of cross-channel noise imbalance. This imbalance is typically sensor specific (Kimura et al., 2004). According to Hensley et al., (2008) the UAVSAR instrument is well calibrated at the hardware level, and the transceiver module for each band is different. Therefore, the presence of cross-channel noise imbalance is either not present or negligible. The estimated value of cross-channel noise imbalance being close to the ideal value of 1 further supports the claim. Expectedly, in this case, hardly any improvements have been observed in case of the improved Quegan's algorithm in contrast with the Quegan's algorithm.

Research Question – III

POA shift is mainly caused by topographic variations. Referring to the discussion regarding the description of the study area in chapter 4, the topographic variation in the study is known to be significantly low. Consequently, the effect of POA shift is expected to be low. However, small changes in the scattering pattern have been observed by means of decomposition modelling before and after POA shift correction. The volume scattering has been reduced in some places as presented in section 5.7 which indicates the effectiveness of POA shift compensation.

Research Question – IV

The proposed algorithm tries to address the high computational cost incurred by the intensive iterative calculations of Ainsworth algorithm while preserving its accuracy. As per the observations in section 5.5 the proposed algorithm has avoided iterative computation in 13.6% cases. However, it may vary depending upon the data. In the best-case scenario, the algorithm will accept the Quegan's solution in all the cases. Consequently, the complexity of the algorithm will be exactly the same as the Quegan's algorithm. Let's T_q represents the average time required to estimate the crosstalk parameters for a single pixel using the Quegan's algorithm and T_a represents the average time required by a single iteration of the Ainsworth algorithm while estimating the crosstalk parameter for a single pixel. If T represents the average time required to estimate crosstalk parameters by the proposed algorithm for a single pixel then in the best-case, equation (51) is satisfied where c is the time taken to check whether the solutions meet the accuracy requirement.

$$T = T_q + c \tag{51}$$

In the worst case, the algorithm accepts only the Ainsworth algorithm's solutions for all the cases. The construct of algorithm shows that it first computes the Quegan's solution then proceeds to compute the Ainsworth's solution only if the solutions of Quegan's algorithm do not satisfy the accuracy requirements. Consequently, in the worst-case, both the solutions for both the algorithms will be computed along with the additional checking for accuracy. Thus, in the worst case, T will change as shown in equation (52) where μ_a is the average number of iterations required in order to obtain the solution of the Ainsworth algorithm. It should be noted that, at worse μ_a can be equal to the maximum allowed iterations indicating the scenario where all pixels require the maximum number of iterations to converge or do not converge at all. For example, in this case, the maximum value of μ is 16.

$$T = T_q + \mu_a T_a + c \tag{52}$$

However, in the average case, the T will change depending upon the ratio of the pixels where Quegan's solution is accepted with respect to the number of pixels where the solution of the Ainsworth algorithm is accepted. If n is the total number of pixels present in the scene and k is the number of pixels where Quegan's solutions are accepted then T will change as shown in equation (53).

$$T = T_q + \mu_a T_a \left(\frac{n - k}{n}\right) + c \tag{53}$$

Therefore, the time saved per pixel (ΔT) with respect to the Ainsworth algorithm can be expressed as shown in the equation (54).

$$\Delta T = \mu_a T_a - \left(T_q + \mu_a T_a \left(\frac{n-k}{n} \right) + c \right)$$

$$\Rightarrow \Delta T = \left(\frac{k}{n} \right) \mu_a T_a - T_q - c$$

$$\Rightarrow \frac{\Delta T}{\mu_a T_a} = \left(\frac{k}{n} \right) - \frac{(T_q + c)}{\mu_a T_a}$$

$$\Rightarrow \frac{\Delta T}{T_A} \approx \left(\frac{k}{n} \right)$$

(54)

Where, $T_A = \mu_a T_a$

The term T_A signifies the average time taken by the Ainsworth algorithm to estimate the crosstalk parameters for a single pixel. Clearly, the speedup ($\Delta T / T_A$) solely depends upon the factor k/n. The term T_q can be ignored since it is constant and $T_a \gg T_q$. Similarly, c is also constant and, it can be ignored as well. In this case $k \approx 135.57 \times 10^3$ and $n = 10^6$, therefore, the speedup is nearly 13.6%. If the terms T_q and c are not ignored the effective speed expected to be slightly below the 13.6%. It is worth mentioning that this efficiency estimation assumes the Single Instruction Multiple Data (SIMD) computer architecture (Hennessy & Patterson, 2017).

7.   CONCLUSION AND RECOMMENDATIONS

7.1.   Conclusion

The primary objective of this study is to compare the performance of different PolSAR calibration algorithms in terms of accuracy. The study focuses mainly on the two algorithms where the performance of both Quegan's and Ainsworth algorithm has been assessed using suitable metrics and through different qualitative measures. Additionally, the performance of the improved Quegan's algorithm has also been evaluated considering it to be an extension of Quegan's algorithm. Moreover, the effect of POA shift has been estimated and corrected. All the objectives have been completed, and all the research questions have been answered adequately. Furthermore, a modified calibration algorithm has been developed in order to reduce the computational cost. Although the dataset used in this study was already radiometrically and phase calibrated, there is a provision for performing radiometric and phase calibration in the implementation if required.

The Quegan's crosstalk algorithm is relatively simple and capable of providing crosstalk estimation quicker than the Ainsworth algorithm. However, in many instances, it fails to reduce the residual crosstalk under CEOS recommended threshold of -35 dB. Although the cross-pol SNR has improved in case of the Quegan's algorithm, the MNE has not been reduced below the limit of -30 dB in all the cases. In contrast, the Ainsworth algorithm not only complied with the CEOS standard and MNE limit but also performed significantly better at minimising the crosstalk while improving the cross-pol SNR to a higher value than that of Quegan's. Since the cross-channel noise imbalance is negligible in this case, the improved Quegan's algorithm performed nearly the same as Quegan's algorithm. These results unambiguously indicate that Ainsworth algorithm performs better than Quegan's algorithm in terms of accuracy. Concerning the channel imbalance, both the algorithms perform nearly the same, Ainsworth algorithm is slightly advantageous, as the reduction of the entropy and scattering angle is relatively higher for this algorithm.

POA shift compensation for this particular study area was not significantly effective due to lack of POA shift attributing to the low topographic variations in the area. However, this does not signify that POA shift correction is unnecessary in all possible scenarios. This procedure necessarily corrects the discrepancies in the scattering pattern incurred by the POA shift if any such anomaly exists. Moreover, the procedure is relatively simple regarding the computation. Therefore, incorporating the POA shift with PolSAR calibration makes the entire process more robust and effective.

The modified algorithm aims to improve computational efficiency without reducing the accuracy of the estimation. This study successfully demonstrated the gain in the computational efficiency of this algorithm. However, there is no strict lower bound for the improvement in efficiency, which implies that it should perform equally or better than the Ainsworth algorithm.

In essence, Ainsworth algorithm is equivalent to or better than Quegan's algorithm in every metric with the cost of lower computational efficiency. The use of the proposed algorithm can partly address the higher computational cost. POA shift correction along with the PolSAR calibration reduces most of the potential discrepancies which might be present in the PolSAR data revealing right scattering pattern.

7.2.   Recommendation

Based on the results and the discussion it is evident that this research is based on a single airborne quad-pol SAR dataset. Therefore, the findings of this research should be rigorously verified on more datasets to further improve the reliability of the findings. Along with this, it would be the interesting to test the effectiveness of the proposed algorithm on multiple datasets from different sensors and frequencies such as P band and C band data from the NASA AIRSAR (Lou, Kim, & van Zyl, 2006) and S-band data from UAVSAR (Hensley et al., 2008).

Radiometric and phase calibration are important because subsequent calibration steps heavily rely on this. Although there is provision for radiometric and phase calibration in the methodology and implementation but these have not been used in this study as the dataset was already radiometrically and phase calibrated. Thus, the radiometric and phase calibration modules need further investigation with appropriate level 1 PolSAR data to cross-validate their results.

This research is focused on the calibration of airborne PolSAR data. However, it would be interesting to observe the effectiveness of this research on spaceborne PolSAR data as well. In the case of the spaceborne PolSAR data, the effect of Faraday rotation attributing to the presence of ionosphere needs to be incorporated into the study accordingly.

Moreover, the potential need for calibration of the PolSAR data acquired in other modes such as dual-pol or compact-pol can be further explored. Ryzhkov, Giangrande, Melnikov, & Schuur, (2005) have studied such issues for the calibration of the dual-pol dataset. The study by McKerracher et al., (2010) can be further evaluated regarding the calibration of compact-pol SAR dataset. Furthermore, the PolSAR calibration method proposed by Shimada, (2011) can be potentially integrated into the future study.

The efficiency of the proposed algorithm has been studied and tested on a standard PC targeting the SIMD computer architecture. This work can be further optimised for Multiple Instruction Multiple Data (MIMD) computer architecture optionally with fast parallel processing in Graphics Processing Unit (GPU) leading to better efficiency. Additionally, a graphical user interface (GUI) for this calibration tool can be developed for convenience.

LIST OF REFERENCES

Ainsworth, T. L., Ferro-Famil, L., & Jong-Sen, L. (2006). Orientation Angle Preserving a Posteriori Polarimetric SAR Calibration. *IEEE Transactions on Geoscience and Remote Sensing*, *44*(4), 994–1003. https://doi.org/10.1109/TGRS.2005.862508

Ainsworth, T. L., & Lee, J. S. (2001). A New Method for a Posteriori Polarimetric SAR Calibration. In *IGARSS 2001. Scanning the Present and Resolving the Future. Proceedings. IEEE 2001 International Geoscience and Remote Sensing Symposium (Cat. No.01CH37217)* (Vol. 1, pp. 420–422). Sydney: IEEE. https://doi.org/10.1109/IGARSS.2001.976177

Al-kahachi, N. (2014). Polarimetric Cross-Talk in SAR System Induced by Antenna Cross- Pol Pattern. In *European Conference on Synthetic Aperture Radar* (pp. 1365–1368).

Andrade, L. A., Nohara, E. L., Peixoto, G. G., Rezende, M. C., & Martin, I. M. (2003). Backscattering Analysis of Flat Plate and Dihedral Corner Reflectors using PO and Comparison with RCS Measurements in Anechoic Chamber. In *Proceedings of the 2003 SBMO/IEEE MTT-S International Microwave and Optoelectronics Conference - IMOC 2003. (Cat. No.03TH8678)* (Vol. 2, pp. 719–724). IEEE. https://doi.org/10.1109/IMOC.2003.1242667

Baffelli, S., Frey, O., Werner, C., & Hajnsek, I. (2018). Polarimetric Calibration of the Ku-Band Advanced Polarimetric Radar Interferometer. *IEEE Transactions on Geoscience and Remote Sensing*, *56*(4), 2295–2311. https://doi.org/10.1109/TGRS.2017.2778049

Bickel, S. H., & Bates, R. H. T. (1965). Effects of Magneto-Ionic Propagation on the Polarization Scattering Matrix. *Proceedings of the IEEE*, *53*(8), 1089–1091. https://doi.org/10.1109/PROC.1965.4097

Bonkowski, R. R., Lubitz, C. R., & Schensted, C. E. (1953). *Studies in Radar Cross-Sections-VI. Cross-sections of corner reflectors and other multiple scatterers at microwave frequencies*. Ann Arbor, MI, USA: University of Michigan Radiation Lab.

Brunfeldt, D. R., & Ulaby, F. T. (1984). Active Reflector for Radar Calibration. *IEEE Transactions on Geoscience and Remote Sensing*, *GE-22*(2), 165–169. https://doi.org/10.1109/TGRS.1984.350610

Campbell, D. B., & Ostro, S. J. (2014). *Radar Astronomy*. Cambridge, Massachusetts: McGraw-Hill Education OP - AccessScience. https://doi.org/10.1036/1097-8542.757209

Clifford, P. M. (1985). The international vocabulary of basic and general terms in metrology. *Measurement*, *3*(2), 72–76. https://doi.org/10.1016/0263-2241(85)90006-5

Cloude, S. R. (2009). *Polarisation: Applications in Remote Sensing* (First). Chippenham, Wiltshire: Oxford University Press. https://doi.org/10.1093/acprof:oso/9780199569731.001.0001

Cloude, S. R. (2009). *Polarization: Application in Remote Sensing*. Oxford University Press.

Cloude, S. R., & Pottier, E. (1997). An Entropy based Classification Scheme for Land Applications of Polarimetric SAR. *IEEE Transactions on Geoscience and Remote Sensing*, *35*(1), 68–78. https://doi.org/10.1109/36.551935

Cloude, S. R. R., & Pottier, E. (1996). A Review of Target Decomposition Theorems in Radar Polarimetry. *IEEE Transactions on Geoscience and Remote Sensing*, *34*(2), 498–518. https://doi.org/10.1109/36.485127

Cote, S., Srivastava, S. K., Dantec, P. Le, & Hawkins, R. K. (2005). Maintaining RADARSAT-1 Image Quality performance in Extended Mission. In *Proceedings of 2nd International Conference on Recent Advances in Space Technologies, 2005. RAST 2005.* (pp. 678–683). IEEE. https://doi.org/10.1109/RAST.2005.1512653

Desnos, Y. L., Buck, C., Suchail, J.-L., Torres, R., Duesmann, B., & Closa, J. (1999). The Envisat ASAR Calibration and Validation Plan. In *SAR Workshop: CEOS Committee on Earth Observation Satellites; Working Group on Calibration and Validation* (p. 323). Toulouse: European Space Agency.

Doerry, A. W., & Brock, B. C. (2009). *Radar Cross Section of Triangular Trihedral Reflector with Extended Bottom Plate*. Albuquerque. https://doi.org/10.2172/984946

Doerry, A. W., Brock, B. C., Doerry, A. W., Brock, B. C., & Doerry, A. W. (2009). *Radar cross section of triangular trihedral reflector with extended bottom plate. International Journal of Antennas and Propagation* (Vol. 2013). Albuquerque. https://doi.org/10.2172/984946

Doring, B. J., Looser, P., Jirousek, M., & Schwerdt, M. (2011). Point target correction coefficients for absolute SAR calibration. In *2011 IEEE International Instrumentation and Measurement Technology*

Conference (pp. 1–6). IEEE. https://doi.org/10.1109/IMTC.2011.5944111

El-Darymli, K., McGuire, P., Gill, E., Power, D., & Moloney, C. (2014). Understanding the significance of radiometric calibration for synthetic aperture radar imagery. In *2014 IEEE 27th Canadian Conference on Electrical and Computer Engineering (CCECE)* (pp. 1–6). IEEE. https://doi.org/10.1109/CCECE.2014.6901104

ESA. (2004). Recommendation at CEOS CAL/VAL 2004. Retrieved February 23, 2019, from http://earth.esa.int/workshops/ceos_sar_2004/recommendation_at_ceos_cal.html

ESA, & European Space Agency. (2017). PolSARpro. Rennes, France: European Space Agency. Retrieved from https://earth.esa.int/web/polsarpro/home

Fore, A. G., Chapman, B. D., Hawkins, B. P., Hensley, S., Jones, C. E., Michel, T. R., & Muellerschoen, R. J. (2015). UAVSAR Polarimetric Calibration. *IEEE Transactions on Geoscience and Remote Sensing, 53*(6), 3481–3491. https://doi.org/10.1109/TGRS.2014.2377637

Fore, A. G., Chapman, B., Hensley, S., Michel, T., & Muellerschoen, R. (2009). *UAVSAR Polarimetric Calibration*. Pasadena, California. Retrieved from http://uavsar.jpl.nasa.

Freeman, A. (1989). The Need For Sar Calibration. In *12th Canadian Symposium on Remote Sensing Geoscience and Remote Sensing Symposium,* (Vol. 1, pp. 230–233). IEEE. https://doi.org/10.1109/IGARSS.1989.567211

Freeman, A. (1992). Radiometric Calibration of SAR Image Data. In *ISPRS Congress Technical Commission I* (pp. 212–222). Washington, D.C., USA: ISPRS Archives – Volume XXIX Part B1. Retrieved from http://www.isprs.org/proceedings/XXIX/congress/part1/212_XXIX-part1.pdf

Freeman, A. (2004). Calibration of linearly polarized polarimetric SAR data subject to Faraday rotation. *IEEE Transactions on Geoscience and Remote Sensing, 42*(8), 1617–1624. https://doi.org/10.1109/TGRS.2004.830161

Gray, A. L., Vachon, P. W., Livingstone, C. E., & Lukowski, T. I. (1990). Synthetic Aperture Radar Calibration using Reference Reflectors. *IEEE Transactions on Geoscience and Remote Sensing, 28*(3), 374–383. https://doi.org/10.1109/36.54363

Griesser, T., & Balanis, C. (1987). Backscatter Analysis of Dihedral Corner Reflectors using Physical Optics and the Physical Theory of Diffraction. *IEEE Transactions on Antennas and Propagation, 35*(10), 1137–1147. https://doi.org/10.1109/TAP.1987.1143987

Hennessy, J., & Patterson, D. (2017). Data-Level Parallelism in Vector, SIMD, and GPU Architectures. In *Computer Architecture* (6th ed., pp. 282–357). Cambridge, Massachusetts: Elsevier Inc. Retrieved from https://www.elsevier.com/books/computer-architecture/hennessy/978-0-12-811905-1

Hensley, S., Wheeler, K., Sadowy, G., Jones, C., Shaffer, S., Zebker, H., … Smith, R. (2008). The UAVSAR instrument: Description and first results. In *2008 IEEE Radar Conference* (pp. 1–6). IEEE. https://doi.org/10.1109/RADAR.2008.4720722

Hoekman, D. H., & Quiriones, M. J. (2000). Land Cover Type and Biomass Classification using AirSAR Data for Evaluation of Monitoring Scenarios in the Colombian Amazon. *IEEE Transactions on Geoscience and Remote Sensing, 38*(2), 685–696. https://doi.org/10.1109/36.841998

Hounam, D., & Wagel, K. H. (2001). A technique for the Identification and Localization of SAR Targets using Encoding Transponders. *IEEE Transactions on Geoscience and Remote Sensing, 39*(1), 3–7. https://doi.org/10.1109/36.898660

Hu, D., Qiu, X., Hu, D., & Ding, C. (2015). Improved Airborne PolSAR Calibration Algorithm based on Time-variant Attitude Compensation. *International Journal of Remote Sensing, 36*(12), 3184–3195. https://doi.org/10.1080/2150704X.2015.1054042

Huynen, J. R. (1970). *Phenomenological Theory of Radar Targets (Doctoral Thesis)*. TU Delft. Retrieved from http://resolver.tudelft.nl/uuid:e4a140a0-c175-45a7-ad41-29b28361b426

Jet Propulsion Laboratory NASA. (2016). Polarimetry. Retrieved November 29, 2018, from https://nisar.jpl.nasa.gov/technology/polsar/

Kemp, W. M., & Martin, N. M. (1990). A Synthetic Aperture Radar Calibration Transponder at C-Band. In *IEEE International Conference on Radar* (pp. 81–85). IEEE. https://doi.org/10.1109/RADAR.1990.201141

Kimura, H. (2009). Calibration of polarimetric PALSAR imagery affected by faraday rotation using polarization orientation. *IEEE Transactions on Geoscience and Remote Sensing, 47*(12), 3943–3950. https://doi.org/10.1109/TGRS.2009.2028692

Kimura, H., Mizuno, T., Papathanassiou, K. P., & Hajnsek, I. (2004). Improvement of Polarimetric SAR

Calibration based on the Quegan Algorithm. In *IEEE International IEEE International IEEE International Geoscience and Remote Sensing Symposium, 2004. IGARSS '04. Proceedings. 2004* (Vol. 1, pp. 184–187). IEEE. https://doi.org/10.1109/IGARSS.2004.1368990

Knott, E. (1977). RCS Reduction of Dihedral Corners. *IEEE Transactions on Antennas and Propagation*, *25*(3), 406–409. https://doi.org/10.1109/TAP.1977.1141586

Lee, J. S., Jansen, R. W., Schuler, D. L., Ainsworth, T. L., Marmorino, G. O., & Chubb, S. R. (1998). Polarimetric analysis and modeling of multifrequency SAR signatures from Gulf Stream fronts. *IEEE Journal of Oceanic Engineering*, *23*(4), 322–333. https://doi.org/10.1109/48.725228

Lee, J. S. S., Schuler, D. L., Ainsworth, T. L., & Boerner, W. M. (2003). Polarization orientation estimation and applications: a review. In *IGARSS 2003. 2003 IEEE International Geoscience and Remote Sensing Symposium. Proceedings (IEEE Cat. No.03CH37477)* (Vol. 1, pp. 428–430). IEEE. https://doi.org/10.1109/IGARSS.2003.1293798

Lee, J. S., Schuler, D. L., & Ainsworth, T. L. (2000). Polarimetric SAR data compensation for terrain azimuth slope variation. *IEEE Transactions on Geoscience and Remote Sensing*, *38*(5), 2153–2163. https://doi.org/10.1109/36.868874

Lenz, R., Schuler, K., Younis, M., & Wiesbeck, W. (2005). High Accuracy Digitally Controlled Active Radar Ground Calibrator System for Terra SAR-X. In *IEEE International Radar Conference, 2005.* (Vol. 2005–Janua, pp. 1–4). IEEE. https://doi.org/10.1109/RADAR.2005.1435783

Lou, Y., Kim, Y., & van Zyl, J. (2006). *THE NASA/JPL AIRBORNE SYNTHETIC APERTURE RADAR SYSTEM. NASA.* Retrieved from https://airsar.jpl.nasa.gov/documents/genairsar/airsar_paper1.pdf

Luscombe, A. P., Chotoo, K., & Huxtable, B. D. (2000). Polarimetric Calibration for RADARSAT-2. In *IGARSS 2000. IEEE 2000 International Geoscience and Remote Sensing Symposium. Taking the Pulse of the Planet: The Role of Remote Sensing in Managing the Environment. Proceedings (Cat. No.00CH37120)* (Vol. 5, pp. 2197–2199). IEEE. https://doi.org/10.1109/IGARSS.2000.858354

McKerracher, P. L., Jensen, J. R., Sequeira, H. B., Raney, R. K., Schulze, R. C., Bussey, D. B. J., … Palsetia, M. (2010). Mini-RF Calibration, a Unique Approach to On-Orbit Synthetic Aperture Radar System Calibration. In *41st Lunar and Planetary Science Conference* (pp. 1–2). Houston, Texas: Lunar Planetary Institute.

Meyer, R. W., & Bowers, J. C. (2012). *Flood-Prone Areas and Waterways, Edwards Air Force Base, California.* Sacramento. Retrieved from https://pubs.usgs.gov/of/2000/ofr00183/ofr00183.pdf

Moreira, A., Prats-Iraola, P., Younis, M., Krieger, G., Hajnsek, I., & Papathanassiou, K. P. (2013). A tutorial on synthetic aperture radar. *IEEE Geoscience and Remote Sensing Magazine*, *1*(1), 6–43. https://doi.org/10.1109/MGRS.2013.2248301

Muellerschoen, R., & Muellerschoen Ronald. (2018). Calibration - UAVSAR. Retrieved May 26, 2018, from https://uavsar.jpl.nasa.gov/cgi-bin/calibration.pl

NASA. (2015). Data and Information Policy: NASA. Retrieved February 24, 2019, from https://science.nasa.gov/earth-science/earth-science-data/data-information-policy

Pottier, E., Schuler, D. L., Lee, J. S., & Ainsworth, T. L. (1999). Estimation of the terrain surface azimuthal/range slopes using polarimetric decomposition of POLSAR data. In *IEEE 1999 International Geoscience and Remote Sensing Symposium. IGARSS'99 (Cat. No.99CH36293)* (Vol. 4, pp. 2212–2214). IEEE. https://doi.org/10.1109/IGARSS.1999.775080

Python Core Team. (2018). Python. Python Software Foundation. Retrieved from https://www.python.org/

Quegan, S. (1994). A Unified Algorithm for Phase and Cross-talk Calibration of Polarimetric Data - Theory and Observations. *IEEE Transactions on Geoscience and Remote Sensing*, *32*(1), 89–99. https://doi.org/10.1109/36.285192

Rosen, P. A., Hensley, S., Wheeler, K., Sadowy, G., Miller, T., Shaffer, S., … Madsen, S. (2006). UAVSAR: A New NASA Airborne SAR System for Science and Technology Research. In *2006 IEEE Conference on Radar* (pp. 22–29). Verona, New York: IEEE. https://doi.org/10.1109/RADAR.2006.1631770

Ryzhkov, A. V., Giangrande, S. E., Melnikov, V. M., & Schuur, T. J. (2005). Calibration Issues of Dual-Polarization Radar Measurements. *Journal of Atmospheric and Oceanic Technology*, *22*(8), 1138–1155. https://doi.org/10.1175/JTECH1772.1

Sarabandi, K. (1993). Calibration of a Polarimetric Synthetic Aperture Radar using a Known Distributed Target. In *Proceedings of IGARSS '93 - IEEE International Geoscience and Remote Sensing Symposium* (pp.

968–970). Tokyo: IEEE. https://doi.org/10.1109/IGARSS.1993.322167

Sato, D., Watanabe, T., Yamada, H., & Yamaguchi, Y. (2013). Comparison of model-based polarimetric decomposition algorithms. In *Asia-Pacific Conference on Synthetic Aperture Radar (APSAR) Conference Proceedings of 2013* (pp. 346–349). Tsukuba, Japan: IEEE.

Shimada, M. (2011). Model-Based Polarimetric SAR Calibration Method Using Forest and Surface-Scattering Targets. *IEEE Transactions on Geoscience and Remote Sensing*, *49*(5), 1712–1733. https://doi.org/10.1109/TGRS.2010.2090046

Shimada, M., & Freeman, A. (1995). A technique for measurement of spaceborne SAR antenna patterns using distributed targets. *IEEE Transactions on Geoscience and Remote Sensing*, *33*(1), 100–114. https://doi.org/10.1109/36.368217

Skolnik, M. I. (1990). *Radar Handbook* (2nd ed.). McGraw-Hill Professional.

Skriver, H., Dierking, W., Gudmandsen, P., Le Toan, T., Moreira, A., Papathanassiou, K., & Quegan, S. (2003). Applications of Synthetic Aperture Radar Polarimetry. *European Space Agency, (Special Publication) ESA SP*, *72*(529), 11–16. Retrieved from http://linkinghub.elsevier.com/retrieve/pii/S0024320503000699

Snoeij, P., Attema, E., Rommen, B., Floury, N., Davidson, M., Duesmann, B., & Rowsell, D. (2010). Transponder Development for Sentinel-1. In *8th European Conference on Synthetic Aperture Radar* (pp. 1–4).

Sorensen, K. W. (2013). A Dihedral Corner Reflector Model for Full Polarization Calibration of RCS Measurements. In *Antennas and Propagation Society Symposium 1991 Digest* (pp. 748–751). IEEE. https://doi.org/10.1109/APS.1991.174947

Tang, J., & Xu, X. (2015). A New Polarimetric Active Radar Calibrator and Calibration Technique. In L. Bruzzone (Ed.) (p. 96431U). https://doi.org/10.1117/12.2194478

Thompson, A. R., Moran, J. M., & Swenson Jr., G. W. (2017). Propagation Effects. In *Interferometry and Synthesis in Radio Astronomy* (pp. 507–593). Weinheim, Germany: Wiley-VCH Verlag GmbH. https://doi.org/10.1002/9783527617845.ch13

Touzi, R. (2007). Target Scattering Decomposition in Terms of Roll-Invariant Target Parameters. *IEEE Transactions on Geoscience and Remote Sensing*, *45*(1), 73–84. https://doi.org/10.1109/TGRS.2006.886176

van Zyl, J. (1990). Calibration of Polarimetric Radar Images using Only Image Parameters and Trihedral Corner Reflector Responses. *IEEE Transactions on Geoscience and Remote Sensing*, *28*(3), 337–348. https://doi.org/10.1109/36.54360

van Zyl, J. (1993). Application of Cloude's Target Decomposition Theorem to Polarimetric Imaging Radar Data. In H. Mott & W.-M. Boerner (Eds.) (p. 184). https://doi.org/10.1117/12.140615

van Zyl, J., & Kim, Y. (2011a). Polarimetric SAR Calibration. In *Synthetic Aperture Radar Polarimetry* (Vol. 44, pp. 145–181). Hoboken, NJ, USA: John Wiley & Sons, Inc. https://doi.org/10.1002/9781118116104.ch4

van Zyl, J., & Kim, Y. (2011b). *Synthetic Aperture Radar Polarimetry*. Hoboken, NJ, USA: John Wiley & Sons, Inc. https://doi.org/10.1002/9781118116104

van Zyl, J., Zebker, H. A., & Elachi, C. (1987). Imaging radar polarization signatures: Theory and observation. *Radio Science*, *22*(4), 529–543. https://doi.org/10.1029/RS022i004p00529

Villano, M., & Papathanassiou, K. P. (2013). SNR and Noise Variance Estimation in Polarimetric SAR data. In *ESA PolInSAR Workshop*. Frascati, Italy: ESA. Retrieved from https://elib.dlr.de/83036/

Wang, Y., Ainsworth, T. L., & Lee, J.-S. (2011). Assessment of System Polarization Quality for Polarimetric SAR Imagery and Target Decomposition. *IEEE Transactions on Geoscience and Remote Sensing*, *49*(5), 1755–1771. https://doi.org/10.1109/TGRS.2010.2087342

Whitt, M. W., Ulaby, F. T., Polatin, P., & Liepa, V. V. (1991). A General Polarimetric Radar Calibration Technique. *IEEE Transactions on Antennas and Propagation*, *39*(1), 62–67. https://doi.org/10.1109/8.64436

Yamaguchi, Y., Moriyama, T., Ishido, M., & Yamada, H. (2005). Four-component scattering model for polarimetric SAR image decomposition. *IEEE Transactions on Geoscience and Remote Sensing*, *43*(8), 1699–1706. https://doi.org/10.1109/TGRS.2005.852084

APPENDIX A

THEORY OF EIGENVALUE BASED POLARIMETRIC DECOMPOSITION

The surface characteristics are best evaluated from interpreting the roll invariant parameters like entropy, anisotropy and alpha angle. This utilises the Eigenvalue decomposition of the coherency matrix $[J]$, owing to the basis invariant description of the scatterers (Cloude, 2009). Moreover, the original coherency matrix is decomposed into the nature of the scattering property (Eigenvectors) and associated relative magnitudes (Eigenvalues). The randomness in the scattering distribution across the surface is represented by entropy (H), wherein the dominance of a specific scattering mechanism is quantitatively assessed (Cloude, 2009). The rugged terrains with increased roughness exhibit higher entropy and, thus, a depolarizing target, thereby utilizing the full spectrum of Eigen values. On the other hand, the variations in alpha angle ($\bar{\alpha}$) denote the type of the mean scattering patterns. The alpha value ranges from 0° to 90° while the bounding limits of entropy parameter are 0 and 1. Furthermore, the anisotropy (A) reflects the divergence in the secondary scattering processes, thereby facilitating more information on the potential surface scatterer in conjunction with entropy (Cloude, 2009). This parameter proves to be prominent in the high entropy scenarios, wherein it becomes difficult for identifying different scattering mechanisms within a resolution cell. The number of Eigen values and their corresponding Eigen vectors are directly proportional to the dimension of the backscattered coherency matrix. In this context, the matrix and surface parameters can be written as (Cloude, 2009).

$$[J] = [U][D][U]^{*T}$$

Where,

$$[U] = \begin{bmatrix} \cos\alpha_1 & \cos\alpha_2 & \cos\alpha_3 \\ \sin\alpha_1\cos\psi_1 e^{-j\phi_1} & \sin\alpha_2\cos\psi_2 e^{-j\phi_2} & \sin\alpha_3\cos\psi_3 e^{-j\phi_3} \\ \sin\alpha_1\cos\psi_1 e^{-j\phi_1} & \sin\alpha_2\cos\psi_2 e^{-j\phi_2} & \sin\alpha_3\cos\psi_3 e^{-j\phi_3} \end{bmatrix}$$

$$[D] = \begin{bmatrix} \lambda_1 & 0 & 0 \\ 0 & \lambda_2 & 0 \\ 0 & 0 & \lambda_3 \end{bmatrix}$$

where λ_1, λ_2 and λ_3 are the three orthogonal Eigen values of the coherency matrix $[J]$, P_i is the probability with which the derived polarization states can be estimated, $[U]$ is the unitary matrix containing the Eigen vectors in the three columns, $[D]$ represents the matrix comprising of probabilities and Eigen values of the original coherency matrix, and (α_i, ψ_i ϕ_i) are the polarisation ellipse parameters. The scattering angle, entropy, anisotropy and probability can be further defined as.

$$\bar{\alpha} = \sum_{i=1}^{3} P_i \alpha_i$$

$$H = -\sum_{i=1}^{3} P_i \log_3 P_i$$

$$A = \frac{\lambda_2 - \lambda_3}{\lambda_2 + \lambda_3}$$

$$P_i = \frac{\lambda_i}{\sum_{k=1}^{3} \lambda_k}$$

The utilization of probabilities gives an elaborated understanding of the entropy parameter based on the spread of these values ranging from non-depolarisation ($H = 0$) to complete depolarisation ($H = 1$) case (Cloude, 2009). Moreover, the normalized form of Eigen values is strongly aligned with the polarity of the backscatter. The polarity parameter can be characterised by the degree of polarisation as the ratio of polarised power to the total power.

THEORY OF Y4R DECOMPOSITION

According to Yamaguchi, Moriyama, Ishido, & Yamada, (2005), the measured covariance matrix ($\langle[C]\rangle$) can be expanded as shown in the equation below.

$$\langle[C]\rangle = f_s\langle[C]\rangle_s + f_d\langle[C]\rangle_d + f_v\langle[C]\rangle_v + f_c\langle[C]\rangle_h$$

Where,

f_s, f_d, f_v and f_c are expansion coefficients.

$\langle[C]\rangle_s, \langle[C]\rangle_d, \langle[C]\rangle_v$ and $\langle[C]\rangle_h$ are surface scattering, double bounce scattering, volume scattering and helical scattering component of the covariance matrix.

$$\langle[C]\rangle_s = \begin{bmatrix} |\beta|^2 & 0 & \beta \\ 0 & 0 & 0 \\ \beta^* & 0 & 1 \end{bmatrix}, \langle[C]\rangle_d = \begin{bmatrix} |\alpha|^2 & 0 & \alpha \\ 0 & 0 & 0 \\ \alpha^* & 0 & 1 \end{bmatrix}$$

$$\langle[C]\rangle_v = \frac{1}{15}\begin{bmatrix} 8 & 0 & 2 \\ 0 & 4 & 0 \\ 2 & 0 & 3 \end{bmatrix}, \langle[C]\rangle_h = \frac{1}{4}\begin{bmatrix} 1 & \pm j\sqrt{2} & -1 \\ \mp j\sqrt{2} & 2 & \pm j\sqrt{2} \\ -1 & \mp j\sqrt{2} & 1 \end{bmatrix}$$

The six unknown parameters $f_s, f_d, f_v, f_c, \alpha$ and β in the model can be obtained from the solutions of the following system of equations.

$$\langle|s_{hh}|^2\rangle = f_s|\beta|^2 + f_d|\alpha|^2 + \frac{8}{15}f_v + \frac{f_c}{4}$$

$$\langle|s_{hv}|^2\rangle = \frac{2}{15}f_v + \frac{f_c}{4}$$

$$\langle|s_{vv}|^2\rangle = f_s + f_d + \frac{3}{15}f_v + \frac{f_c}{4}$$

$$\langle s_{hh}s_{vv}^*\rangle = f_s\beta + f_d\alpha + \frac{2}{15}f_v - \frac{f_c}{4}$$

$$\frac{1}{2}\Im(\langle s_{hh}s_{hv}^*\rangle + \langle s_{hv}s_{vv}^*\rangle) = \frac{f_c}{4}$$

$$f_c = 2|\Im\langle s_{hv}^*(s_{hh} - s_{vv})\rangle|$$

APPENDIX B
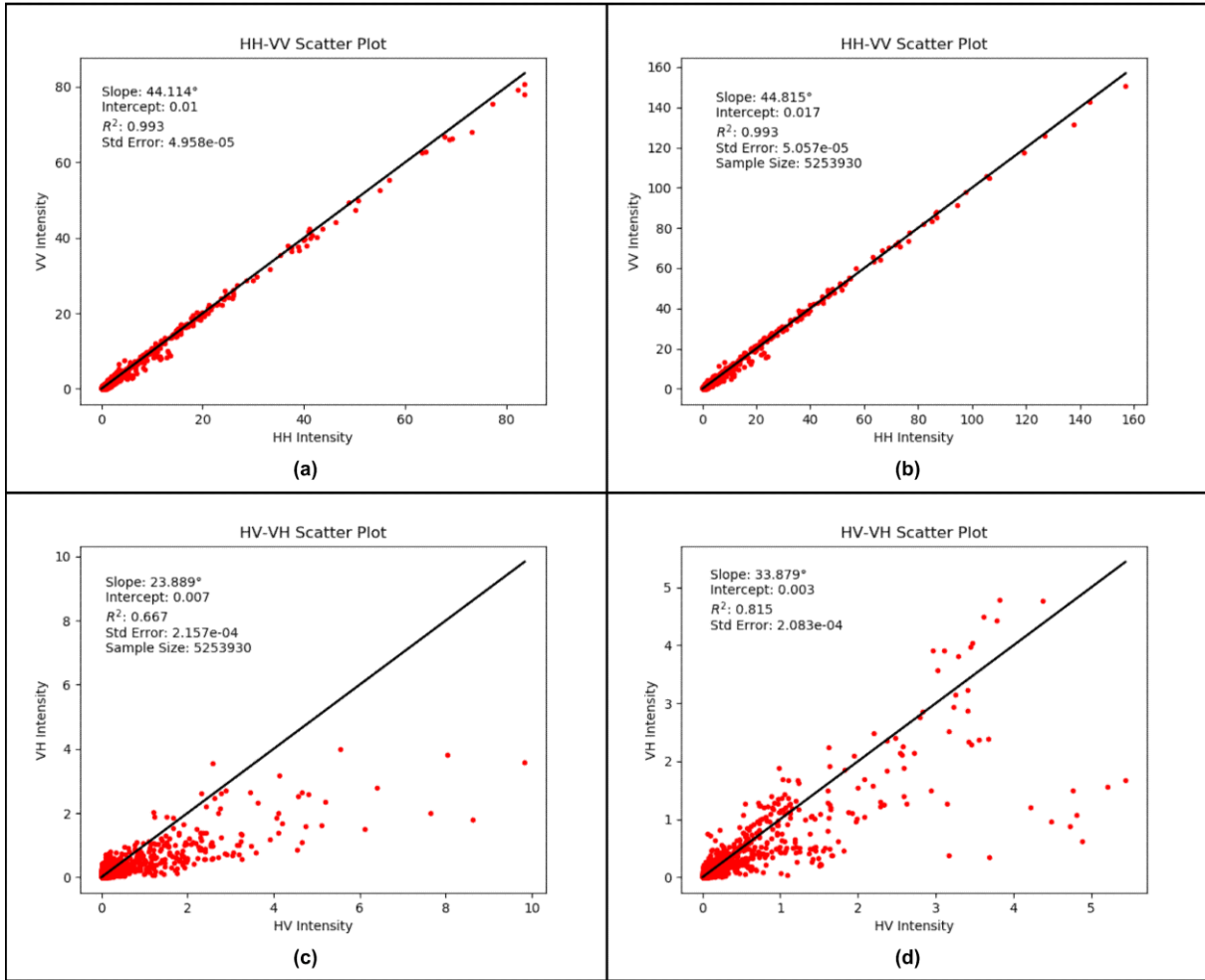
Figure 1: Scatter plots of the backscattering intensities, (a) HH-VV scatter plot of the intensities before calibration, (b) HH-VV scatter plot of the intensities after Quegan's calibration, (c) HV-VH scatter plot of the intensities before calibration, (d) HV-VH scatter plot of the intensities after Quegan's calibration. Both in case of co-pol channels and cross-pol channels the intensities are more aligned along the $y = x$ line after performing the calibration.
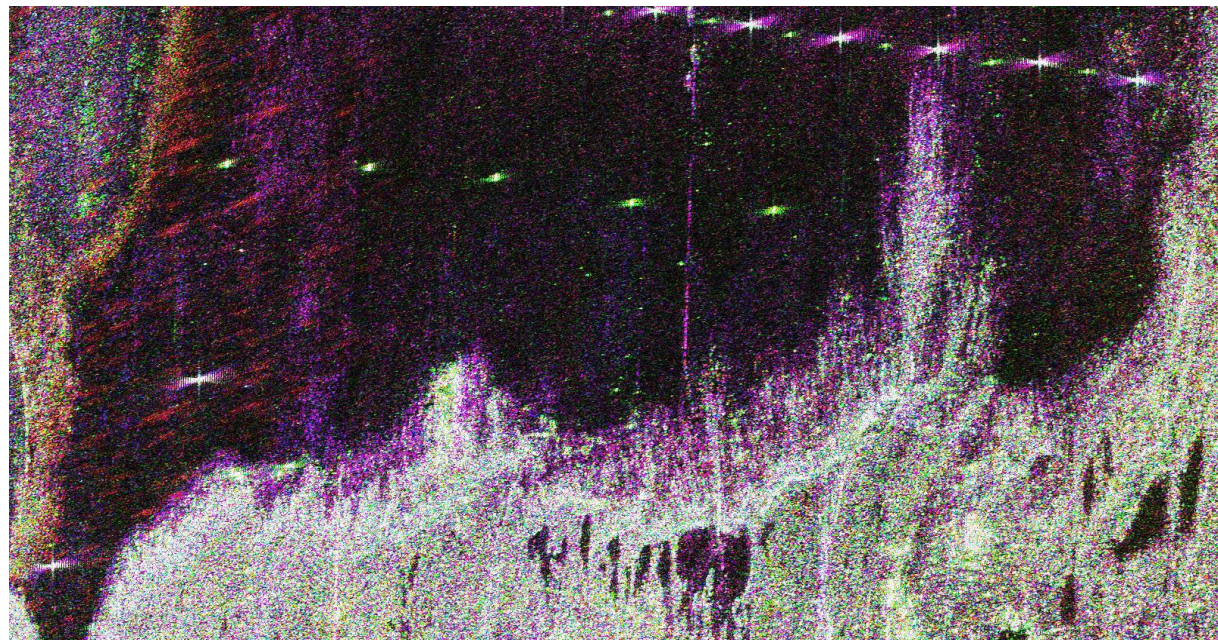
(a)
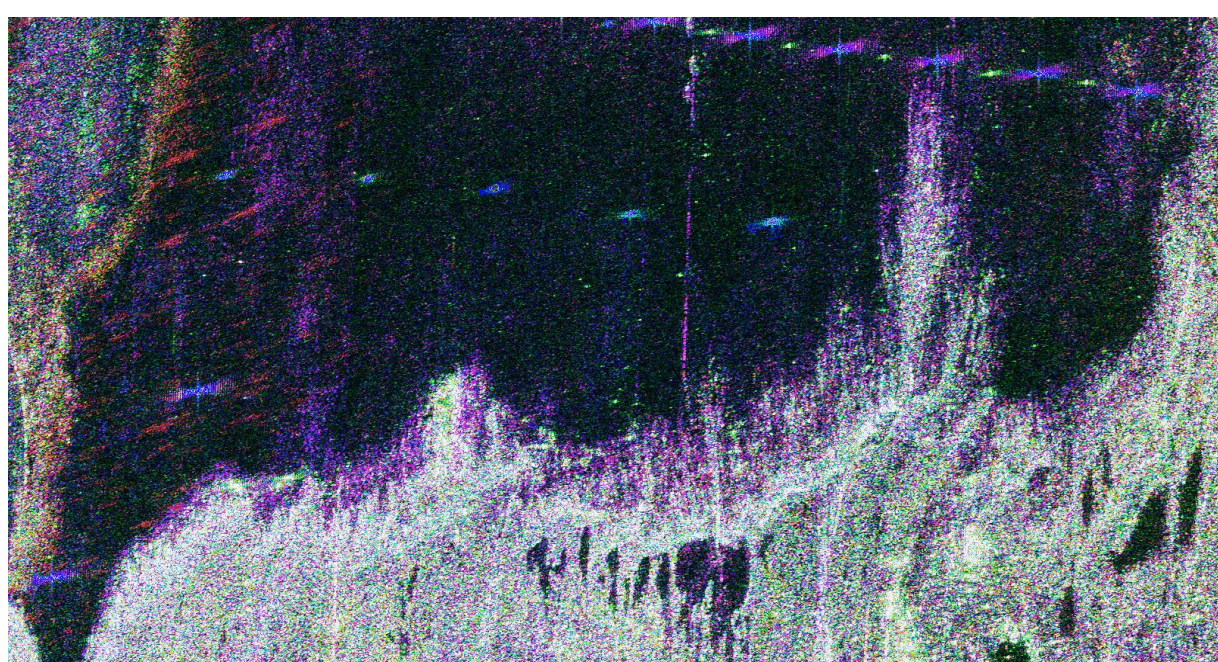
(b)

Figure 2: RGB composite after performing Y4R decomposition of a P band AIRSAR dataset of the Rosamond site, (a) Uncalibrated dataset, (b) Calibrated dataset using Ainsworth's algorithm.